

Soft colloidal matter in external driving fields: Theory and simulation

Inaugural-Dissertation
zur
Erlangung des Doktorgrades der
Mathematisch-Naturwissenschaftlichen Fakultät
der Heinrich-Heine-Universität Düsseldorf

vorgelegt von

Martin Rex

aus Mettmann

Dezember 2007

Aus dem Institut für Theoretische Physik II: Weiche Materie
der Heinrich-Heine-Universität Düsseldorf

Gedruckt mit der Genehmigung der
Mathematisch-Naturwissenschaftlichen Fakultät
der Heinrich-Heine-Universität Düsseldorf

Referent: Prof. Dr. H. Löwen
Koreferent: Prof. Dr. G. Nägele
Koreferent: Prof. Dr. H. Stark

Tag der mündlichen Prüfung: 14.04.2008

©Martin Rex
All Rights Reserved.

This thesis is based on the following original papers:

Chapter 2

M. Rex and H. Löwen,
Lane formation in oppositely charged colloids driven by an electric field: Chaining and two-dimensional crystallization,
Phys. Rev. E **75**, 051402 (2007)

M. Rex and H. Löwen,
Influence of hydrodynamic interactions on lane formation in oppositely charged driven colloids,
DOI 10.1140/epje/i2007-10274-4, Eur. Phys. J. E (2008)

M. Rex, T. Vissers, C. P. Royall, A. van Blaaderen, and H. Löwen,
Second order nonequilibrium phase transition in oppositely charged driven colloids,
(in preparation)

H. Löwen, H. H. Wensink, and M. Rex,
Driven colloidal mixtures and colloidal liquid crystals,
AIP Conference Proceedings, **982**, 284-288 (2008)

Chapter 3

M. Rex and H. Löwen,
Hydrodynamic interactions in dynamical density functional theory,
(in preparation)

M. Rex and H. Löwen,
Dynamical density functional theory with hydrodynamic interactions and colloids in unstable traps,
submitted to Phys. Rev. Lett. (2008)

Chapter 4

H. H. Wensink, H. Löwen, M. Rex, C. N. Likos, and S. van Teeffelen
Long-time self-diffusion of Brownian Gaussian-core particles,
to appear in Computer Physics Communications (2008)

M. Rex, H. H. Wensink, and H. Löwen,
Dynamical density functional theory for anisotropic colloidal particles,
Phys. Rev. E **76**, 021403 (2007)

Summary

In this work, we present recent results obtained for the dynamics of colloidal dispersions out of equilibrium in external fields by means of theory and computer simulations. In the first part of this thesis we study a binary mixture of oppositely charged colloids which is driven by an external field by carrying out extensive Brownian dynamics computer simulations. The particles are driven in opposite directions by either an electric field or by gravity. While the direct forces are chosen to be identical, the hydrodynamic interactions, which are taken into account on the Rotne-Prager level, are different in the two situations. In the presence of an electric field the Oseen contribution to the mobility tensor is screened due to the forces acting on the counterion cloud surrounding a charged colloid. The systems undergo a nonequilibrium phase transition, the so-called lane formation, if the external driving force exceeds a critical value. In this nonequilibrium phase particles driven alike align behind each other and form lanes which comprise only particles of the same charge. In the plane perpendicular to the external field we find additionally a variety of different phases. We map out steady-state phase diagrams for both the case where hydrodynamic interactions are neglected, as well as when they are taken into account.

In the second chapter we derive a dynamical density functional theory with hydrodynamic interactions and examine the out-of-equilibrium dynamical evolution of density profiles of hard spherical colloids in an unstable optical trap. We complement our theoretical analysis by carrying out extensive Brownian dynamics simulations and demonstrate thereby the validity of our theory. We predict a considerable retardation of the dynamics compared to the case where hydrodynamic interactions are neglected.

Finally, in the third part we generalize the formalism of dynamical density functional theory for translational Brownian dynamics to that of anisotropic colloidal particles which perform both translational and rotational Brownian motion. Using a mean-field approximation for the density functional and a Gaussian-segment model for the rod interaction, the dynamical density functional theory is then applied to a concentrated rod suspension in a confined slab geometry made by two parallel soft walls. The walls are either expanded or compressed and the relaxation behavior is investigated for an equilibrated starting configuration. We find distinctly different orientational ordering during expansion and compression. Furthermore, an external field which aligns the rods perpendicular to the walls is turned on or switched off and similar differences in the relaxational dynamics are found. Comparing the theoretical predictions to Brownian dynamics computer simulation data, we find very good agreement.

Zusammenfassung

Die vorliegende Arbeit untersucht die Nichtgleichgewichts-Dynamik kolloidaler Dispersionen in äußeren Feldern mit Hilfe theoretischer Methoden und Computersimulationen. Im ersten Teil dieser Arbeit analysieren wir mit Brownscher Dynamik Simulationen eine äquimolare binäre Mischung entgegengesetzt geladener Kolloide, die durch ein externes elektrisches Feld gegeneinander getrieben werden. Wenn die Stärke der externen treibenden Kraft einen kritischen Wert überschreitet, zeigt das System einen Nichtgleichgewichts-Phasenübergang, die sogenannte Spurbildung (*lane formation*). In dieser Nichtgleichgewichtsphase ordnen sich die Partikel entlang des elektrischen Feldes hintereinander so an, dass eine Spur ausschließlich gleich geladene Kolloide enthält. Wir untersuchen die Natur des Phasenübergangs und den Einfluss hydrodynamischer Wechselwirkungen und beobachten, dass die Spuren in der Ebene senkrecht zu dem externen Feld, abhängig von der Dichte und der Abschirmlänge, verschiedene Strukturen bilden. Wir finden u. a. zweidimensionale Gitter- und netzwerkartige Strukturen. Die Ergebnisse fassen wir in Nichtgleichgewichts-Phasendiagrammen zusammen.

Im zweiten Teil dieser Arbeit leiten wir eine dynamische Dichtefunktionaltheorie mit hydrodynamischen Wechselwirkungen her. Anhand dieser untersuchen wir die zeitliche Entwicklung von Dichteprofilen harter sphärischer Kolloide in einer instabilen optischen Falle. Wir ergänzen unsere Untersuchungen durch extensive Computersimulationen und zeigen so die Gültigkeit unserer Theorie. Durch den Vergleich mit Berechnungen, in denen hydrodynamische Wechselwirkungen vernachlässigt werden, stellen wir fest, dass die Dynamik des Systems durch die hydrodynamische Wechselwirkung deutlich gebremst wird.

Im letzten Teil erweitern wir den Formalismus der dynamischen Dichtefunktionaltheorie für Translationsdynamik auf die Translations- und Rotationsdynamik anisotroper Brownscher Teilchen. Unter Verwendung einer *mean-field* Näherung für das Dichtefunktional und eines Gaußschen Segmentmodells für die Stäbchen–Stäbchen Wechselwirkung, wenden wir die dynamischen Dichtefunktionaltheorie auf eine konzentrierte Stäbchenlösung in einer durch zwei weiche Wände eingeschränkten Geometrie an. Zusätzlich untersuchen wir den Einfluss eines externen Orientierungsfeldes, das die Stäbchen senkrecht zu den Wänden ausrichtet. Wir vergleichen die Vorhersagen unserer Theorie für die zeitliche Entwicklung der Dichteprofile mit denen, die durch Brownsche Dynamik Simulationen gewonnen wurden, und finden sehr gute Übereinstimmung.

Contents

| | | |
|----------|---|-----------|
| 1 | Introduction | 1 |
| 2 | Lane formation in oppositely charged colloids driven by an external field | 7 |
| 2.1 | Introduction | 8 |
| 2.2 | The Model | 8 |
| 2.3 | Order parameters and structural correlations | 13 |
| 2.4 | Lane formation in oppositely charged colloids driven by an electric field: chaining and two-dimensional crystallization . . | 16 |
| 2.4.1 | Introduction | 16 |
| 2.4.2 | Results | 17 |
| 2.5 | Influence of hydrodynamic interactions on lane formation in oppositely charged driven colloids | 30 |
| 2.5.1 | Introduction | 30 |
| 2.5.2 | Results | 30 |
| 2.6 | Conclusions | 39 |
| 3 | Dynamical density functional theory with hydrodynamic interactions | 43 |
| 3.1 | Introduction | 43 |
| 3.2 | Equation of motion for the one-body density | 45 |
| 3.3 | The model | 49 |
| 3.4 | Results | 52 |
| 3.5 | Conclusions | 58 |
| 4 | Dynamical density functional theory for anisotropic colloidal particles | 59 |
| 4.1 | Introduction | 59 |
| 4.2 | Equation of motion for the one-body density | 61 |
| 4.3 | Model and free energy functional | 64 |
| 4.4 | Dynamic processes | 66 |

| | | |
|----------|---|-----------|
| 4.5 | Results | 69 |
| 4.5.1 | Compression and expansion | 70 |
| 4.5.2 | Orienting external field | 73 |
| 4.6 | Conclusions | 74 |
| 5 | Conclusion and outlook | 77 |
| A | Ewald sum of μ_{ij}^{LA} | 81 |
| | Bibliography | 83 |

Chapter 1

Introduction

In recent years soft condensed matter (or soft matter, for brevity) has emerged as an important subfield of condensed matter physics. It is a collective term for a rich variety of different substances whose common feature is that they react much more sensitively to mechanical stresses or shear strains than *hard* materials such as aluminum or sodium chloride. The reason for the eponymous softness is the underlying mesoscopic¹ length scale of the constituents and can be understood from the following considerations: Imagine two equally sized perfect crystals consisting either of mesoscopic (soft matter) or of Ångström sized (atoms) particles. Now, given that the typical binding energy per particle is in both systems of the same order [1], there are simply many fewer particles in the soft matter crystal to resist deformation than in the atomistic one. To be more precise, a quantitative measure for the rigidity is the shear modulus of a crystal that scales as the inverse cube of the edge length of an elementary cell. Thus, in our example, the ratio between the shear moduli of the soft matter and the atomistic crystals is extremely small, namely up to 10^{-12} for micrometer sized constituents. Since this behavior is independent of the details of the particles, the important role of the mesoscopic length scale of the constituents is made the defining property of soft matter². The realm of soft matter thus subsumes materials such as colloidal dispersions, liquid crystals, polymers, membranes, dendrimers, surfactants and biological macromolecules [3]. Those substances have a wide range of applications, e.g., in paints, pharmaceuticals, detergents and cosmetics, lubricants, and foods [4–6].

This thesis is devoted to the study of colloidal dispersions (also called

¹The mesoscopic length scale ranges from the nanometer to the micrometer scale.

²According to the International Union of Pure and Applied Chemistry (IUPAC), soft condensed matter systems consist of supramolecular entities, which cover at least one structural length scale which is in the mesoscopic regime [1, 2]

colloids). Colloids are solutions of mesoscopic objects dissolved in a microscopic host solvent. Though significant complexity arises from having different constituents with widely separated length scales, the description of the equilibrium properties of the mesoscopic particles resembles that of a system of atoms in vacuum – the solvent does not appear explicitly [7]. What seems to be a gross omission turns out to be a sophisticated theoretical approach. As was first pointed out by Onsager [8], the degrees of freedom of the solvent can be eliminated and the colloidal particles interact with an effective potential (“the potential of mean force”) which accounts for all solvent effects. When discussing the dynamics, on the other hand, the analogy between colloids and atoms breaks down. The reason is that atoms in a gas move *ballistically*, colloids in a suspension move *diffusively*. At the most microscopic level, we can describe the system by the positions and momenta of the small liquid molecules and the large colloidal particles, which interact by atomic and molecular forces and follow trajectories determined by Newton’s equations of motion. However, because we are concerned primarily with the motion of the colloidal particles, one can obtain a more tractable description by eliminating the liquid variables with the Mori-Zwanzig projection method [9] to find a set of Langevin equations for the momentum variables of the large particles. These dissipative stochastic equations replace the time-reversal invariant Newtonian equations. In this reduced description, the liquid molecules act as a heat bath, which provides a set of random forces and torques, as well as friction that produce drag forces and torques on the colloidal particles and are related by fluctuation–dissipation theorems. In colloidal suspensions, where usually the long-time configurational dynamics are of interest, additionally the momentum variables may be dropped from the equations of motion. This is justified by the enormous difference in size and mass of the suspended colloidal particles and the solvent molecules which implies a corresponding separation in the relaxational timescales of the two. At times of the order of the Fokker-Planck scale, $\tau_{\text{FP}} \approx 10^{-14} \text{s}$, the solvent coordinates are already relaxed to thermal equilibrium. On the other Brownian or Smoluchowski timescale, $\tau_{\text{S}} \approx 10^{-9} \text{s}$, the momentum coordinates of the solute particles relax to equilibrium with the heat bath of the solvent molecules. Finally, the time scale of interest for colloidal particles is their typical diffusive time scale τ_{B} (i.e., the time required to move a distance equal to its own diameter due to thermal motion), which is of the order of microseconds to seconds [10], and thus a statistical description involving only the coordinates of the solutes is feasible [10]. Intuitively, the motion of colloidal particles resembles that of marbles in honey plus Brownian motion. An important result of the “slow” movement of the particles is that the dynamics of colloids can easily be resolved experimentally.

Both facts render colloidal dispersions as appealing *model systems* for physics in and out of equilibrium. They are two of the main reasons for the strong interdisciplinary interest that has arisen in the last few decades. The term model system is justified for the following reasons:

First, the mesoscopic particles lie within a length scale observable using visible light and their dynamics are on an experimentally accessible time scale. Therefore, their structure and their dynamical processes can be observed in real space by optical techniques such as confocal microscopy. This offers the unique opportunity to study dynamic processes in and out of equilibrium by direct observation and allows investigation of the behavior of colloids simultaneously by theory, computer simulation, and experiment.

Second, though colloidal particles extend well beyond the atomistic regime and are therefore free of quantum mechanical effects, instructive analogies between atomistic liquids and solids can be identified [4]. This is because mesoscopic colloidal particles are still small enough to have a well defined temperature that manifests itself through the Brownian motion they perform. Therefore, in equilibrium they occur in the phase with the lowest free energy, and the standard tools of classical statistical mechanics and thermodynamics apply. Consequently they also exhibit collective behavior similar to that found in atomistic systems. For example, liquid-vapor phase separation or solid phases with different lattice structures possessing virtually every possible symmetry group are found in colloids.

Third, the effective mutual interaction between colloidal particles is well-characterized and can be tailored nearly at will. In contrast to atomistic systems where the interaction potential is prescribed by quantum mechanics, the effective interaction potential between, e.g., charged spherical colloids can be tuned from a bare Coulombic to a hard-sphere potential by changing the salt concentration of the suspending fluid and thereby changing the screening length of the underlying Yukawa potential [9]. Especially the nearly perfectly realized hard-sphere liquid has become famous and provides excellent laboratories in which to test theoretical predictions [11].

Fourth, mesoscopic particles can be individually controlled by external fields (e.g. laser tweezers) such that single particles or clusters of particles can be trapped or dragged. This offers the opportunity to study nearly arbitrary configurations of the observed system. Moreover, through the use of external fields, self-organization can be directed to make new advanced materials [12].

Finally, there are many different kinds of shapes of colloidal particles available. Prominent examples are spheres, rods, platelets, ellipsoids, or dumbbells etc., which give rise to a bunch of new phases such as nematic or smectic order in liquid crystals.

In conclusion, colloidal dispersions offer an ideal testing ground for fundamental concepts in physical science, both in and out of equilibrium. Consequently, colloids are natural candidates for studying dynamical processes in nonequilibrium situations as is the main interest of this thesis. We predict the dynamics of colloidal dispersions in external fields by means of both, theory and computer simulation, in nonequilibrium systems.

In the first part of this thesis, we focus on a binary mixture of oppositely charged colloids which is driven by an external field. Therefore, we briefly review what is known about driven diffusive systems out of equilibrium. Of particular interest are nonequilibrium phase transitions in such systems, where abrupt changes in the properties of the system can result from small changes in control parameters such as temperature, density, or external forces. While bulk equilibrium phase transitions are by now well understood both by computer simulation [13, 14] and by statistical theories [3, 9, 15], out-of-equilibrium phenomena still lack a rigorous treatment on the particle level [16, 17]. For systems in thermal equilibrium the framework provided by Gibbs allows us in principle to compute averages of all time-independent observables once the microscopic Hamiltonian and thereby the distribution over configurational space of the system is known. The remaining difficulties are “merely” technical (though in general challenging). For systems out of equilibrium on the other hand, until now no similar general classification scheme has been available [17]. This is immediately evident when considering the enormous complexity of nonequilibrium time-dependent behavior. Nonetheless, some good progress in understanding these processes has been made. One obvious approach is to study steady-state processes. Here, the system has “settled down” and the probability distribution becomes time-independent, yet still non-Hamiltonian. In 1983, Katz *et al.* [18, 19] presented a system which, while being as simple as possible, still retains the essence of the difficulties of “far from equilibrium” states, in order to study nonequilibrium phase-transitions; the Ising lattice gas model in which the constituent particles have an enhanced/suppressed probability of jumping from a lattice site to an unoccupied one in/against field direction. It is now referred to as the “standard model” [17]. They found that particles form strips along the field direction when a critical field strength is exceeded, and observed a distinct influence of the field on the equilibrium critical point of the Ising-like liquid–vapor phase-separation [18, 19]. A similar pattern, though off-lattice and without the presence of an equilibrium critical point, was recently discovered in a colloidal system: the so-called lane formation [16, 20, 21]. Here, a repulsive binary colloidal mixture is exposed to a constant external driving field that acts in opposite directions on the two otherwise identical species. For forces stronger than a critical force, particles driven alike align behind

each other. In this way, the driven particles form stripes (or lanes) along the field direction that comprise only particles of the same species. As a result, lane formation enhances the drift velocity in field direction [20]. It seems to be a very common scenario in oppositely driven systems, and similar behavior has also been found in granular systems [22, 23], at fluid–fluid interfaces [24], in sheared bilayers [25], and pedestrian dynamics [26, 27]. Leunissen *et al.* [28] have recently presented the first experimental confirmation of lane formation in colloids in an electrophoresis experiment of oppositely charged colloidal particles exposed to an external electric field. In the first part of this thesis, we perform extensive Brownian dynamics (BD) computer simulations to study this very system. BD simulations solve the stochastic Langevin equations of motion for particles performing Brownian motion. What renders the dynamics of colloids different from ballistic motion, apart from the random Brownian forces and the damping of the velocity of the particles due to the friction with the viscous solvent, is the solvent flow field induced by the motion of a mesoscopic particles. The flow field then influences the surrounding particles even if there are no direct mutual forces between them. This solvent-mediated interactions are called the hydrodynamic interactions and are typically long-ranged and of a many-body nature. In simulations hydrodynamic interactions are included through the mobility tensor whose long-distance contribution is called Oseen tensor [13]. In the first instance, we neglect hydrodynamic interactions and characterize different structures perpendicular to the direction of drive. Then, in a next step we study the influence of hydrodynamic interactions on the phase behavior. Thereby, we study two different setups; namely electrophoresis and sedimentation. In the former the Oseen contribution to the mobility tensor is screened due to the forces acting on the counterions. We confirm the previously observed results in the electrophoresis, while different structures are found in the sedimentation.

The second part of the thesis is devoted to *dynamical density functional theory* (DDFT). This theory predicts the time-evolution of the one-particle density of a system, i.e. the probability of finding a particle with coordinates in a volume element, subjected to external fields. It makes use of the formally exact static classical density functional theory. This theory has proved to be a very convenient tool that is based on the free-energy density functional of a given system to derive the equilibrium density profile in external fields. Density functional theory has been successfully applied to problems such as adsorption, wetting, confinement, and solid–liquid and liquid–gas phase transitions [15, 29–31]. Several attempts to generalize the theory to nonequilibrium processes have been carried out in the past. The present version was originally proposed on a phenomenological basis by Evans [29] and indepen-

dently by Dieterich [32]. However, it was Marconi and Tarazona [31, 33] who presented a stringent derivation from the Langevin equation of motion and demonstrated the assumption underlying the DDFT: namely that the correlations of the particles in the out-of-equilibrium system are approximately those of a system in equilibrium with the same density profile. Archer and Evans [34] provided an alternative derivation from the Smoluchowski equation, which is the equation for time-evolution of the probability density in configurational space. In both cases hydrodynamic interactions are ignored. A rigorous proof of the existence of an exact DDFT has been given by Chan and Finken [35], showing that in principle all the time-dependent properties of the system may be expressed as functionals of the time-dependent density. Unfortunately, this proof does not provide a practical formalism. However, to date many studies have demonstrated the accuracy of the original version and its approximation in a variety of different systems, e.g., [34, 36–40]. In this thesis, we extend the DDFT, to include hydrodynamic interactions on a two-body level and to predict the rotational dynamics of anisotropic particles. We fill both gaps without further approximations in chapter 3 and 4, respectively. First, we generalize the existing theory to incorporate hydrodynamic interactions and apply it to a hard-sphere system in an unstable optical trap. Then, in chapter 4, we derive a DDFT formalism for rotational dynamics of anisotropic particles and apply the resulting equation to predict the switching dynamics of soft rods through an external nematic ordering field in strong confinement. For both setups we demonstrate the accuracy of the derived equations by comparing the results to those obtained by extensive Brownian dynamics simulations.

This thesis is organized as follows. In chapter 2, we study a mixture of oppositely charged colloids driven by an external field in two steps. First, in section 2.4, we perform Brownian dynamic simulation to study lane formation in an equimolar system of oppositely charged colloidal particles while neglecting hydrodynamic interactions. In section 2.5, we then expand the model by considering the influence of hydrodynamic interactions on lane formation. In chapter 3, we derive an equation for the time-evolution of the one-body density in the framework of the DDFT, including hydrodynamic interactions, and apply it to a hard-sphere cluster trapped and driven by a laser field. In chapter 4, we show how rotational dynamics are to be treated within DDFT and study the switching dynamics of soft rods. Finally, in chapter 5, we conclude and give an outlook to possible future work.

Chapter 2

Lane formation in oppositely charged colloids driven by an external field

In this chapter, we study a binary mixture of oppositely charged colloids which is driven by an external field by means of extensive Brownian dynamics computer simulations. The system investigated is designed to model an experimental setup in which recently lane formation was observed [28]. In section 2.4, we first ignore hydrodynamic interactions, whose calculation is computationally very costly, and characterize the observed structures. We find a variety of different phases involving lanes with two-dimensional crystalline order perpendicular to the field and network-like structure reminiscent of a phase-separating fluid. We map out a whole steady-state phase diagram for different values of the screening length and the volume fraction. In section 2.5, we then study the influence of hydrodynamic interactions on the Rotne-Prager level on the results. Thereby, we examine two different setups; namely electrophoresis and sedimentation. In the former case the Oseen contribution to the mobility tensor is screened due to the opposite motion of counterions. Virtually all phases are confirmed and only minor changes on the phase boundaries are observed when the external field stems from an electric field. For the sedimentation, on the other hand, the phase diagram is altered and two different structures perpendicular to the field direction are identified: a square-lattice and a phase separation.

2.1 Introduction

As already stated in the introductory chapter, the physics of phase transitions in nonequilibrium are still in its infancy [17]. Colloidal suspensions in external fields are excellent model systems to study those phase transitions [3,41]. One important example, which builds the basics of electrophoresis and electro-osmosis [42], is to expose charged colloidal particles to an external electric field. A constant electric field leads to a nonequilibrium drift of the particles. If a binary mixture of oppositely driven particles is considered, there is a transition toward formation of lanes at high driving fields and sufficient particle concentration. Each lane consists of particles driven alike. This transition was found in Brownian dynamics simulations [20, 21, 43–47] of a binary mixture of repulsive particles driven by opposite forces. It occurs in two and three spatial dimensions. In two dimensions, it was reported to be a first-order nonequilibrium transition with a hysteresis in a suitable order parameter [20]. We address this issue in Sec. 2.5.2.

The general scenario is reminiscent of that of pedestrians moving in two opposite directions in a pedestrian zone [26, 27]. Similar patterns were observed in simulations of granular systems [22, 23, 48], at fluid-fluid interfaces [24], in sheared bilayers [25], and in driven diffusive lattice gases [49].

Recently, the formation of lanes in a colloidal system was confirmed in real space experiments by Leunissen *et al.* [28]. The dynamics of oppositely charged colloidal suspensions in an external field was studied by confocal microscopy. In the absence of an electric driving field, these suspensions form binary crystals [50, 51] coexisting with a vacuum. If the applied field strength exceeds a critical threshold, the equilibrium crystal is destroyed and particles form lanes parallel to the applied field, or jam in opposing bands perpendicular to the field direction.

In this chapter we study this system by means of extensive BD computer simulations. We thereby, proceed as follows: First, we explain the model and the simulation details in Sec. 2.2. Then, we define the used analyzing tools to calculate the structural correlations in the system and to detect lane formation in Sec. 2.3. In Sec. 2.4 we present the results obtained with hydrodynamic interactions ignored and in Sec. 2.5 we then study its influence. Finally, in Sec. 2.6 we conclude and outlook.

2.2 The Model

We perform Brownian dynamic simulations to study an equimolar binary mixture of N ($N = 2000$ in Sec. 2.4 and $N = 1024$ in Sec. 2.5) oppositely

charged colloidal particles of diameter σ dissolved in a solvent fluid of shear viscosity η at temperature T and volume fraction $\phi = 2N\pi\sigma^3/6l^3$ exposed to an external driving field, where l is the dimension of a cubic simulation box having periodic boundary conditions. Henceforth, σ serves as the unit of length and $k_B T$, the thermal energy, as the energy unit of the system. To mimic the experiments by Leunissen *et al.* [28, 52] the particles interact with an effective screened Coulomb potential (or Yukawa potential) plus a steric repulsion V_h :

$$V(r_{ij}) = V_0 \frac{Z_i Z_j}{(1 + \kappa\sigma/2)^2} \frac{e^{(-\kappa\sigma(r_{ij}/\sigma - 1))}}{r_{ij}/\sigma} + V_h(r_{ij}) \quad (2.1)$$

with $V_0 = 50k_B T$ the strength of the interaction potential and $Z_i = \pm 1$ the sign of the charge of particle i . It has been shown experimentally that this Yukawa interaction is a suitable effective interaction for this system [28, 52]. $r_{ij} = |\mathbf{r}_i - \mathbf{r}_j|$ denotes the distance between particle i and j , where \mathbf{r}_i is the coordinate vector. The inverse screening length κ governs the range of the interaction and is determined by the salt concentration of the solution. The steric repulsion between the particles, that prevents the system from collapsing, is approximated by a repulsive (shifted and truncated) Lennard-Jones potential

$$V_h(r_{ij}) = \begin{cases} \epsilon \left[\left(\frac{\sigma}{r_{ij}} \right)^{12} - \left(\frac{\sigma}{r_{ij}} \right)^6 + \frac{1}{4} \right] & \text{if } r_{ij} \leq 2^{1/6}\sigma \\ 0 & \text{else,} \end{cases} \quad (2.2)$$

with $\epsilon = 4V_0/(1 + \kappa\sigma/2)^2$. A plot of the potential is shown in Fig. 2.1. The constant external driving field that acts in opposite directions on the two different particle species reads as

$$\mathbf{F}_i^{\text{ext}} = Z_i f \mathbf{e}_z, \quad (2.3)$$

where \mathbf{e}_z is the unit vector along the z direction and f is the strength of the external force which is chosen to be $f = 276k_B T/\sigma$ in Sec. 2.4 and $f = 150k_B T/\sigma$ in Sec. 2.5, respectively. In the former case we chose a stronger external field to be well in the laning regime [see Fig. 2.28] and to have more pronounced structures in the lateral direction, i.e., the direction perpendicular to the field. The minor influences on the observed phases of the different field strengths are addressed in Subsec. 2.5.2. Though the interaction strength and the external force are large against the thermal energy, we perform Brownian dynamics simulation to prevent particles from crystallizing within a lane.

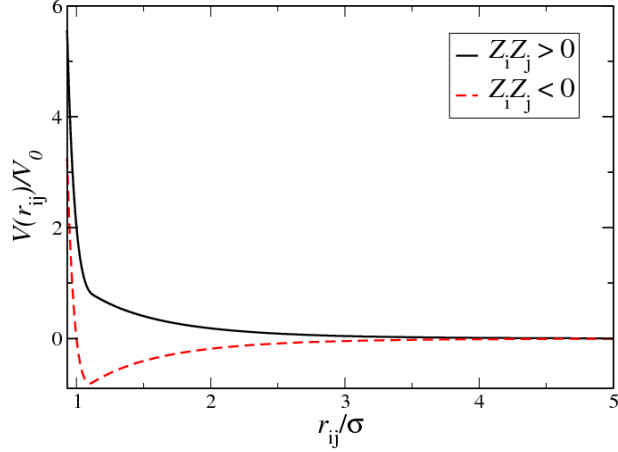


Figure 2.1: Interaction potential between like-charged (solid black curve) and oppositely charged (dashed red curve) particles for $\kappa\sigma = 1$.

In Sec. 2.5, we distinguish between two different setups that are identical as long as hydrodynamic interactions are ignored. The external force is supposed to stem from either an electric field (electrophoresis) or a gravitational field (sedimentation) accompanied with different buoyant masses of the oppositely charged particles. Though the external force Eq. (2.3) may in both cases be identical, if the charges and/or buoyant masses are chosen accordingly, the hydrodynamic interactions are not.

The algorithm used to simulate the diffusive Brownian motion of the colloidal particles was proposed by Ermak and McCammon [53]. Here, the translational displacements of the particles are deemed to occur in time steps of fixed length Δt and the update algorithm is given by [13]:

$$\mathbf{r}_i(t + \Delta t) = \mathbf{r}_i(t) + \Delta t \sum_{j=1}^N \left\{ \frac{\mathbf{D}_{ij}(t)}{k_B T} \cdot \mathbf{F}_j(t) + \nabla_{\mathbf{r}_j} \cdot \mathbf{D}_{ji}(t) \right\} + \Delta \mathbf{r}_i^G, \quad (2.4)$$

where \mathbf{D}_{ij} denotes the diffusion tensor field depending solely on the positions of the particles at time t . The random displacements $\Delta \mathbf{r}_i^G$ are chosen from a joint Gaussian distribution with mean and covariant matrix [13]

$$\langle \Delta \mathbf{r}_i^G \rangle_G = 0; \quad \langle \Delta \mathbf{r}_i^G \Delta \mathbf{r}_j^G \rangle_G = 2\mathbf{D}_{ij} \Delta t, \quad (2.5)$$

where $\langle \dots \rangle_G$ denotes the average over the Gaussian noise distribution. $\mathbf{F}_i(t)$, $i = 1, \dots, N$, comprises the nonhydrodynamic forces due to interparticle interactions, determined by the gradient of the interaction potentials in Eq. (2.1) and Eq. (2.2), and the external force $\mathbf{F}_i^{\text{ext}}$, Eq. (2.3), acting onto particle i .

Hydrodynamic interactions are included in the simulation through the mobility tensor $\boldsymbol{\mu}_{ij} = \mathbf{D}_{ij}/k_{\text{B}}T$. In a first approach, we neglect the numerically very costly hydrodynamic interactions completely to be in the position to study larger systems and longer times and to assess the effect of hydrodynamic interactions on the system. In that case the diffusion tensor is given by Stoke's law in diagonal form

$$\gamma\boldsymbol{\mu}_{ij} = \delta_{ij}\mathbf{1}, \quad (2.6)$$

with friction $\gamma = 3\pi\eta\sigma_{\text{H}}$, where σ_{H} is the hydrodynamic diameter. The integration of Eq. (2.4) is then carried out by using the stochastic Runge Kutta algorithm which has been shown [54, 55] to give more accurate results than the conventional Brownian dynamics algorithm of Ermak [56]. In the sedimentation and electrophoresis situation we approximate the mobility tensor by two-body interactions. In this approximation the divergence in Eq. (2.4) vanishes always [57]. When studying the sedimentation, the buoyant masses of the oppositely charged particles are supposed to be such that due to Archimedes principle the same force acts on the two species but in opposite directions. The action of gravity on the surrounding microions, which screen the Coulomb potential, can safely be neglected. Therefore, in sum no net force is acting on the solvent and overall it remains quiescent. Then, for a pair of spheres of hydrodynamic diameter σ_{H} the mobility tensor is approximated by the well-known Rotne-Prager expression [58]

$$\gamma\boldsymbol{\mu}_{ij}^{\text{RP}} = \delta_{ij}\mathbf{1} + (1 - \delta_{ij}) \left[\frac{3\sigma_{\text{H}}}{8}\mathbb{O}(\mathbf{r}_{ij}) + \frac{\sigma_{\text{H}}^3}{16}\mathbb{Q}(\mathbf{r}_{ij}) \right], \quad (2.7)$$

where

$$\mathbb{O}(\mathbf{r}) = \frac{1}{|\mathbf{r}|}(\mathbf{1} + \hat{\mathbf{r}}\hat{\mathbf{r}}); \quad \mathbb{Q}(\mathbf{r}) = \frac{1}{|\mathbf{r}|^3}(\mathbf{1} - 3\hat{\mathbf{r}}\hat{\mathbf{r}}), \quad (2.8)$$

with the unit vector $\hat{\mathbf{r}} = \mathbf{r}/|\mathbf{r}|$, $\hat{\mathbf{r}}\hat{\mathbf{r}}$ a dyadic product, and δ_{ij} Kronecker's symbol. On this level of approximation we incorporate all interactions up to $O((\sigma_{\text{H}}/r)^3)$. Higher order contributions such as many-body, coupling between rotational and translational motions, and lubrication forces are neglected. Note, that the leading term in Eq. (2.7) is given by $\mathbb{O}(\mathbf{r})$ which is of the order of $1/|\mathbf{r}|$ for large distances.

However, when regarding the electrophoresis, the mobility tensor has to be altered since forces induced by the surrounding counterions into the solvent are in sum equal to the force induced by a colloidal particle. Thus, the solvent flow stemming from the drag on the counterions cannot be neglected as is done in the sedimentation case. For this case, Long and Ajdari [59] have calculated the solvent flow field. Thereby, they assumed that the colloidal

particle can be treated as a point-like charge Q in an electrolyte which induces an excess of counterions in its neighborhood. They approximated the resulting net charge distribution by the linear Debye-Hückel theory [11], such that the charge density in the solution is given by $\rho_c(\mathbf{r}) = -Q\kappa^2 \exp(-\kappa r)/4\pi r$. Together with Faxén's law, which states that at large enough distances a sphere is simply advected by the velocity of the solvent [60], this results in an effective screening of the leading far-distance term of the hydrodynamic interactions between the colloidal particles. The mobility tensor $\boldsymbol{\mu}_{ij}^{\text{LA}}$ then reads as

$$\begin{aligned} \gamma \boldsymbol{\mu}_{ij}^{\text{LA}} = & \delta_{ij} \mathbf{1} + \frac{3\sigma_{\text{H}}}{4}(1 - \delta_{ij}) \left[\frac{e^{-\kappa r_{ij}}}{r_{ij}} \left(\left(1 + \frac{1}{\kappa r} + \frac{1}{\kappa^2 r^2} \right) \mathbf{1} - \right. \right. \\ & \left. \left. \left(\frac{1}{3} + \frac{1}{\kappa r} + \frac{1}{\kappa^2 r^2} \right) 3\hat{\mathbf{r}}_{ij}\hat{\mathbf{r}}_{ij} \right) - \frac{1}{\kappa^2} \mathbb{Q}(\mathbf{r}_{ij}) \right]. \end{aligned} \quad (2.9)$$

Here, the leading order term is $\mathbb{Q}(\mathbf{r}_{ij})$ which decays as $1/|\mathbf{r}^3|$. Some further remarks are in order. The charge density distribution is described on the Debye-Hückel level that is suited for weakly charged point ions. The distortion of the spherical electrolyte atmosphere around the colloidal particle by the electric field is neglected. For high volume fractions and large screening length where particles are close to contact the above mobility tensor might be inaccurate. However, to some extent the problems are overcome by the fact that the considered colloidal particles are coated with a polymer layer. To account for this polymer coating, that gives rise to the steric repulsion, we choose $\sigma_{\text{H}} = 0.9\sigma$ throughout this chapter. Additionally, this ensured the positive definiteness of the mobility tensor since configurations with $|\mathbf{r}_i - \mathbf{r}_j| \leq \sigma_{\text{H}}$ are of negligible statistical weight.

More sophisticated simulation techniques for spherical particles in an unbounded space including lubrication approximation for particles in close proximity and multipolar expansion methods are available [61–65]. However, in the electrophoresis where the hydrodynamic interactions of the counterions become important explicit simulations of all colloidal particles and their counterions – 110 per colloidal particle in the experiments by Leunissen *et al.* – are still beyond computational means. Therefore, we adopted the calculations of Long and Ajdari to our simulations and compare it to the sedimentation problem on the same level of accuracy, i.e. the Rotne-Prager level. To our best knowledge this is the first Brownian dynamic simulations with the Long and Ajdari mobility term (2.9).

Both mobility tensors (2.7) and (2.9) are long-ranged and thus require an Ewald-like summation in simulations analogous to Coulomb and dipole-dipole interactions. Details on the summation and discussions about appropriate boundary conditions to the system can be found elsewhere [66–69].

We applied the scheme suggested by Beenakker [69] and adapted it for $\boldsymbol{\mu}_{ij}^{\text{LA}}$ accordingly, see Appendix A. The square root of the diffusion tensor, needed when calculating the random displacements in Eq. (2.5), are obtained from a Cholesky decomposition:

$$\mathbf{D} = \mathbf{L} \cdot \mathbf{L}^{\text{T}}, \quad (2.10)$$

where \mathbf{L} is a lower triangular matrix and \mathbf{L}^{T} is its transpose. A suitable time scale for our system is $\tau_{\text{B}} = \gamma\sigma^2/k_{\text{B}}T$. The equations of motion including the external field are numerically solved using a small finite time step $\Delta t = 2 \cdot 10^{-5}\tau_{\text{B}}$ in all simulations. The starting configuration of all simulations including HIs was a homogeneous mixture. For the case of ignored HIs we tried different starting configurations but the system was observed to run into the same nonequilibrium steady-state independent of the initial configuration unless stated differently in the text. Statistics were gathered after an initial relaxation period of $20\tau_{\text{B}}$. We address the issue of system-size effects in subsection 2.4.2.

2.3 Order parameters and structural correlations

We monitor a suitable order parameter Φ to detect the laning transition, which is defined as follows. An order parameter $\Phi_i = (n_l - n_o)^2 / (n_l + n_o)^2$ is assigned to every particle i . The numbers n_l and n_o are the numbers of like-charged particles and oppositely charged particles, respectively, whose projections of distance onto the plane perpendicular to the field are smaller than a suitable cutoff length scale z_c . This order parameter is equal to 1 if all particles within this distance criterion are of the same kind and zero if $n_l = n_o$, i.e., a homogeneous mixture. We chose for convenience $z_c = \frac{3}{4}\sigma$ to detect all lanes starting from a single queue of particles. The global order parameter Φ is then defined as

$$\Phi = \frac{1}{N} \left\langle \sum_{i=1}^N \Phi_i \right\rangle_t, \quad (2.11)$$

where the angular brackets $\langle \dots \rangle_t$ denote a time average. The global order parameter Φ is practically zero for a homogeneous mixed configuration, since oppositely charged particles will be found inside the cutoff distance but it gets close to unity if the same particles are located on top of each other, i.e., in a state of lanes. In what follows we will use the following threshold: for $\Phi \geq 3/4$ we call the configuration a state of lanes while in the opposite case ($\Phi < 3/4$)

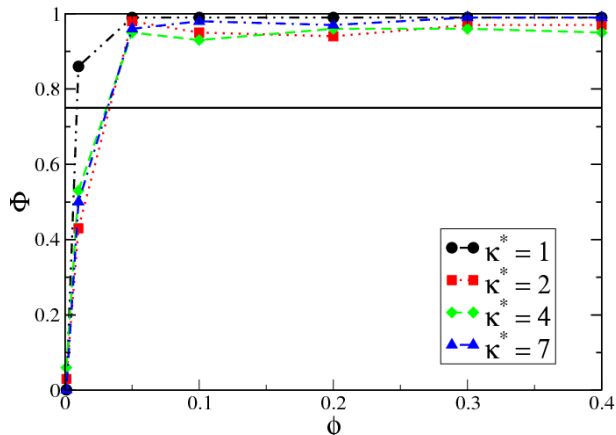


Figure 2.2: Dimensionless order parameter Φ as a function of the volume fraction ϕ for different inverse screening lengths κ^* with hydrodynamic interactions neglected. The straight line indicates the threshold dividing states of lanes (above) from states of no lanes (below).

we call it a state without lanes. A typical result for the order parameter Φ as a function of the volume fraction ϕ is depicted in Fig. 2.2 for different inverse screening lengths κ^* and neglected hydrodynamic interactions. We observe that for low volume fractions $\phi < 0.01$ the laning order parameter is small, but upon increasing the volume fraction it sharply increases to a value close to unity. Only for strongly Coulomb coupled particles, $\kappa^* \leq 1$, is the order parameter in the laning regime for $\phi = 0.01$. This behavior can be understood intuitively. When the volume fraction and the Coulomb coupling are small, the mean particle separation is several diameters and thus the particles are hardly correlated and do not form lanes; whereas for sufficiently high densities or sufficiently low κ^* we observe lane formation due to the stronger interaction. A detailed discussion on the phase transition as a function of the strength of the driving force is given in Sec. 2.5.2.

As mentioned in the introduction, we find a variety of different situations within the laning regime depending on the volume fraction and the screening length. Therefore, we monitor the following analysis tools to classify different states of lanes. To distinguish the particles species they are labeled henceforth A and B . We calculate a pair distribution function perpendicular to the field direction to check for the structure in the lateral direction which

is defined as follows:

$$g_{\perp}(r_{\perp}) = \frac{1}{\rho N} \left\langle \sum_{\substack{i,j \\ (i \neq j)}}^N \delta(\mathbf{r}_{\perp} - |\mathbf{r}_{i\perp} - \mathbf{r}_{j\perp}|) \delta(z_i - z_j) \right\rangle_t, \quad (2.12)$$

Here, \mathbf{r}_{\perp} denotes the lateral direction, i.e., $\mathbf{r} = (\mathbf{r}_{\perp}, z)$, $\delta(\mathbf{r})$ Dirac's delta distribution, and $\rho = 6/\pi\phi\sigma^3$ the number density. Similarly, we calculate the pair distribution functions between the different particle species $g_{AB}(r_{\perp})$ and like-charged particles $g_{AA}(r_{\perp})$, which are defined as follows:

$$g_{AB}(r_{\perp}) = \frac{2}{\rho N} \left\langle \sum_{\substack{i,j \\ (Z_i \neq Z_j)}}^N \delta(\mathbf{r}_{\perp} - |\mathbf{r}_{i\perp} - \mathbf{r}_{j\perp}|) \delta(z_i - z_j) \right\rangle_t, \quad (2.13)$$

and

$$g_{AA}(r_{\perp}) = \frac{2}{\rho N} \left\langle \sum_{\substack{i,j \\ (Z_i = Z_j, i \neq j)}}^N \delta(\mathbf{r}_{\perp} - |\mathbf{r}_{i\perp} - \mathbf{r}_{j\perp}|) \delta(z_i - z_j) \right\rangle_t. \quad (2.14)$$

Additionally, we calculate the Fourier transforms $\hat{h}_X(k)$ of $h_X(r_{\perp}) = g_X(r_{\perp}) - 1$ to obtain the structure factors

$$S_X(k) = 1 + \rho \hat{h}_X(k), \quad (2.15)$$

with $X = \perp, AA, AB$ and the wave vector $k = |\mathbf{k}|$, where $\mathbf{k} = (2\pi/l)(k_x, k_y)$ and k_x and k_y are integers. A prepeak in the structure factor is an indication of an additional mesoscopic length scale as is typical for bicontinuous networks, such as, e.g., microemulsions [70, 71].

To detect two-dimensional crystallization in the lateral direction we monitor bond-order parameters $\langle \Psi^{(k)} \rangle$ similar to those frequently used in two-dimensional systems [72–75]. These order parameters check for symmetry of the bonds between particles. We assign to every particle a local bond-order parameter

$$\Psi_i^{(k)} = \left| \frac{1}{N_b} \sum_{j=1}^{N_b} e^{ki\Theta_{ij}} \right|, \quad (2.16)$$

that is close unity for a particle whose neighbors have a k -fold symmetry, and remains small otherwise. The global bond-order parameters $\langle \Psi^{(k)} \rangle$ are then defined by

$$\langle \Psi^{(k)} \rangle = \frac{1}{N} \left\langle \sum_{i=1}^N \Psi_i^{(k)} \right\rangle_t. \quad (2.17)$$

In Eq. (2.17), i runs over all particles of the system, and in Eq. (2.16), j runs over all neighbors of i , Θ_{ij} denotes the angle between the projection of the bond connecting particles i and j onto the xy plane and an arbitrary but fixed reference axis in this plane, and N_b denotes the number of bonds of particle i . We define a bond between two particles if they are next neighbors in the z direction and their projected distance onto the xy plane is less than 1.3σ and more than σ . This somewhat arbitrary definition may be applied since we find that the resulting $\Psi^{(k)}$ depends only weakly on the precise definition of the neighbor distance. In fact, it has already been observed earlier that details of the neighborhood definition have negligible influence on the results of the bond-order parameter [73, 74]. This allows us to discriminate between a fluidlike structure where all $\langle \Psi^{(k)} \rangle$ are small and a crystalline one. Furthermore, a k -fold symmetry within a crystalline structure in the lateral direction can clearly be detected. The distribution function $P(\Psi_i^{(k)})$ according to Eq. (2.17) of the local bond-order parameter $\Psi_i^{(k)}$ also sheds light on *coexistence* of a crystalline phase with a second one, since its distribution reveals a two-peak structure in that case. Thus it allows for detection of coexistence regimes.

2.4 Lane formation in oppositely charged colloids driven by an electric field: chaining and two-dimensional crystallization

2.4.1 Introduction

In this section, we perform extensive Brownian dynamics simulations without hydrodynamic interactions between the constituent particles. The obtained results are summarized in a nonequilibrium “phase diagram” classifying different steady-states as a function of the colloidal volume fraction and the Coulomb coupling. Different steady-states are characterized by structural correlations perpendicular and parallel to the applied field, whose definitions are presented in the previous section. We find a variety of different phases involving lane chains at small volume fraction and low screening, and lanes with two-dimensional crystalline order perpendicular to the field at high volume fraction. The lateral crystalline order can be a square, triangular, or rhombic lattice. In between there is a lateral network structure.

2.4.2 Results

(a) Different state points

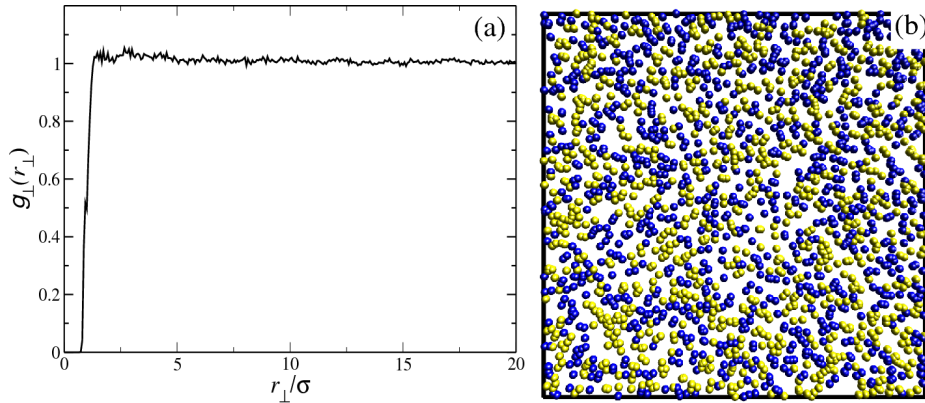


Figure 2.3: Pair distribution function $g_{\perp}(r_{\perp})$ as defined in Eq. (2.12) for $\phi = 0.01$ and $\kappa^* = 7$ (a) and the corresponding projections of the particle positions onto the area perpendicular to the field (b).

We first discuss eight different typical state points shown in Figs. 2.3 - 2.16 below and then summarize more data in a nonequilibrium state diagram Fig. 2.18. For each, we monitor the lateral pair distribution function

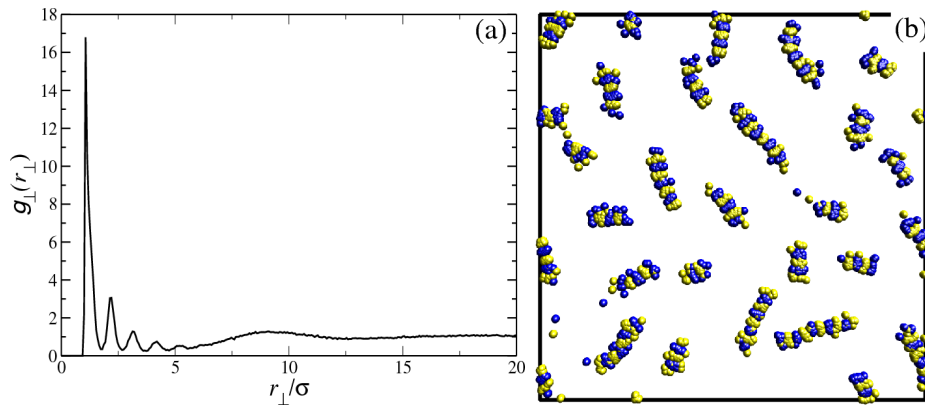


Figure 2.4: Same as Fig. 2.3 for $\phi = 0.01$ and $\kappa^* = 0.2$. Statistics are gathered after an initial relaxation time of $10\tau_B$.

$g_{\perp}(r_{\perp})$ as defined in Eq. (2.12) and present the results with a typical particle snapshot projected to a plane perpendicular to the applied driving field.

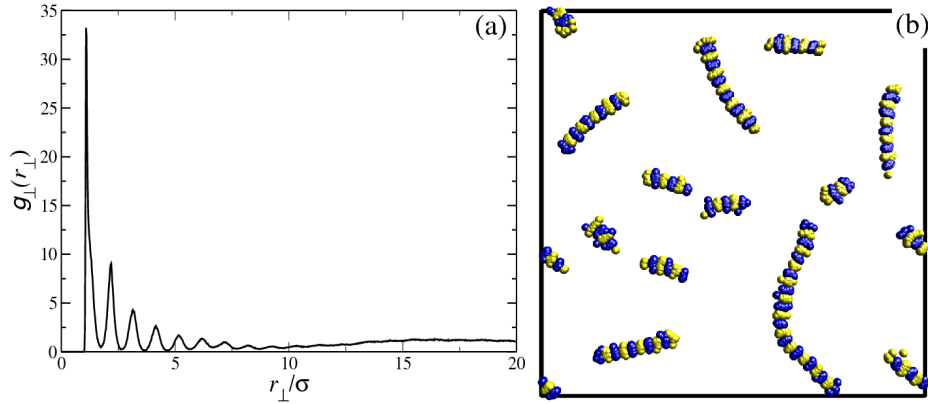


Figure 2.5: Same as Fig. 2.4. Statistics are gathered after an initial relaxation time of $320\tau_B$.

We accompany the results with adequate structural correlations and order parameters. The first parameter set is for *low density* ($\phi = 0.01$) and *high screening* ($\kappa^* = 7$), see Fig. 2.3. In this case, there is no fully developed lane formation, yet the projected particle snapshots reveal some anisotropic coarsening which results in an intermediate value of the order parameter $\Phi = 0.5$ as shown in Fig. 2.2. Concomitantly, apart from a correlation hole, there is no liquid or solid structure in the lateral direction, because the particles hardly interact with each other.

The second situation is for *low screening and low density* ($\phi = 0.01$). Then, initially a few lanes of oppositely charged particles form chainlike objects, i.e., a string of alternating lanes; see Fig. 2.4. This formation process occurs typically within a few τ_B , when starting from a mixed disordered configuration. We emphasize that a strong mutual attraction is needed to stabilize the chains; no chains are obtained for repulsive Yukawa mixtures [20]. It is interesting to follow the further dynamical evolution of the chains. Then, neighboring lane chains fuse subsequently and grow. The fusing process is slow compared to the initial formation of the small chains. The growing process can clearly be deduced from the projected snapshot of Fig. 2.5(b) and the corresponding lateral pair correlation function, Fig. 2.5(a), which exhibits an ordering phenomena along the chains. In the latter case, the pair correlation reveals more peaks than in the early stage, showing that the average chain length is growing in time. In Fig. 2.6 the number of chains N_C as a function of time is displayed. One clearly observes the gradual reduction in the number of chains. The inset shows a log-log plot suggesting that the decrease follows a scaling law with best fit $N_C = A/t^\alpha$ with $A = 60$ and $\alpha = 0.32$. But, due

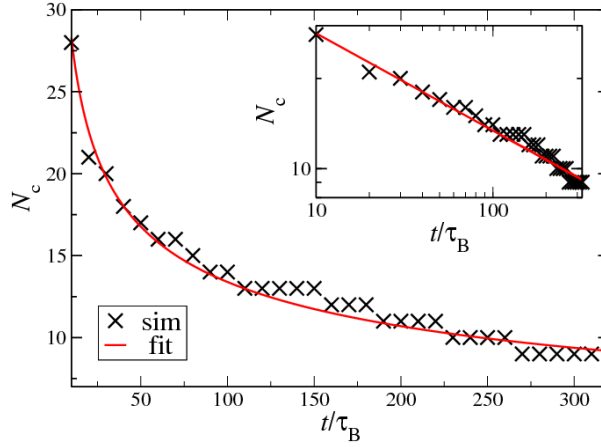


Figure 2.6: Number of chains N_C as a function of time. The straight red line is the best fit of a scaling law to the simulation results (symbols). The inset shows a double-logarithmic plot of the same data.

to the limited time window accessible in the simulation, the ultimate steady-state is not clear; one may conjecture that it is a fully phase-separated region coexisting with a region of no lanes. Nevertheless, the lane chains should be clearly observable as transient dynamical states in an experiment. A similar chain formation is observed for higher volume fraction up to $\phi = 0.05$. The appearance of chains can be qualitatively understood when regarding pairs of lanes. Since a lane pair of oppositely charged particles clearly possesses a dipolar moment the effective interaction between pairs is expected to be like that between dipoles. In fact, a similar chaining behavior has also been

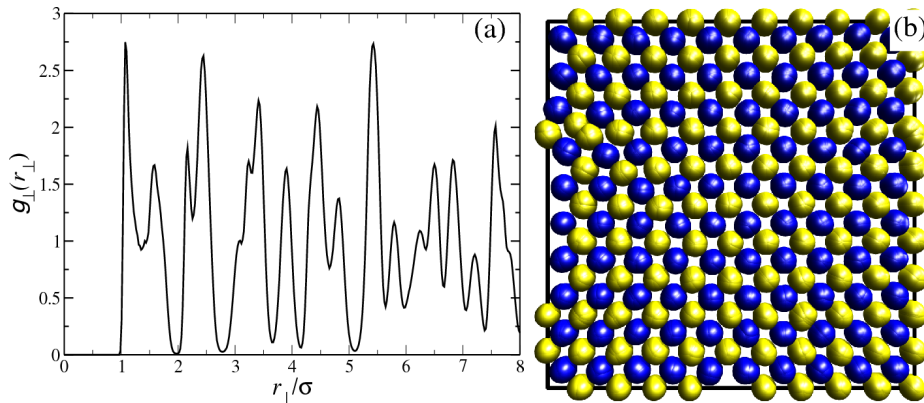


Figure 2.7: Same as Fig. 2.3 for $\phi = 0.3$ and $\kappa^* = 2$.

observed in equilibrium dipolar fluids; see, e.g., [76–78].

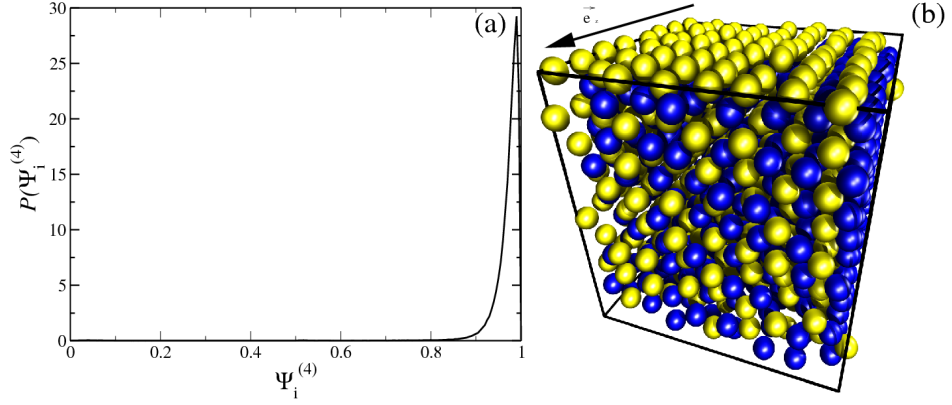


Figure 2.8: Bond-order parameter distribution $P(\Psi_i^{(4)})$ for $\phi = 0.3$ and $\kappa^* = 2$ (a) and a corresponding typical simulation snapshot (b). The latter clearly indicates a square lattice in the lateral direction.

Next we explore a parameter combination with *low screening and high density*; see Fig. 2.7, where data for $\phi = 0.3$ and $\kappa^* = 2$ are shown. As is clearly visible from both the pair correlation function and the projected snapshots, a lateral crystal-like order emerges. Oppositely driven lanes are placed on a square lattice as the high value of $\langle \Psi^{(4)} \rangle = 0.95$ clearly reveals. The sharp distribution of $P(\Psi_i^{(4)})$ depicted in Fig. 2.8(a) indicates indeed a single state with fourfold symmetry. This lattice formation can be qualitatively

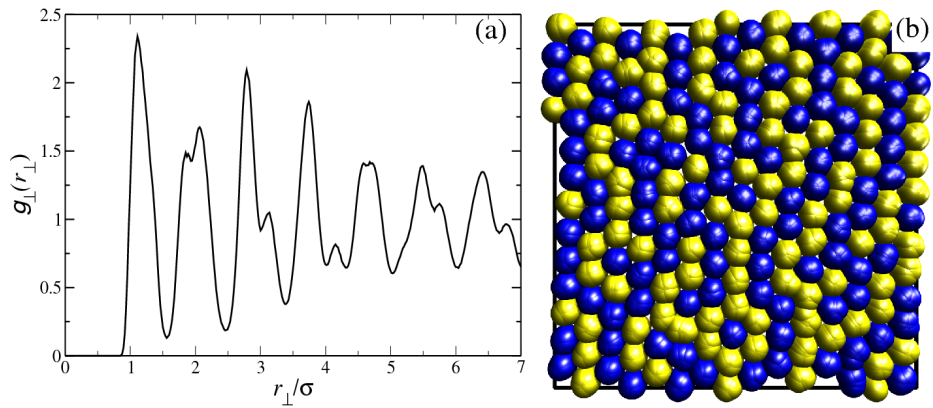


Figure 2.9: Same as Fig. 2.3 for $\phi = 0.4$ and $\kappa^* = 8$.

understood from an effective interaction between oppositely charged driven

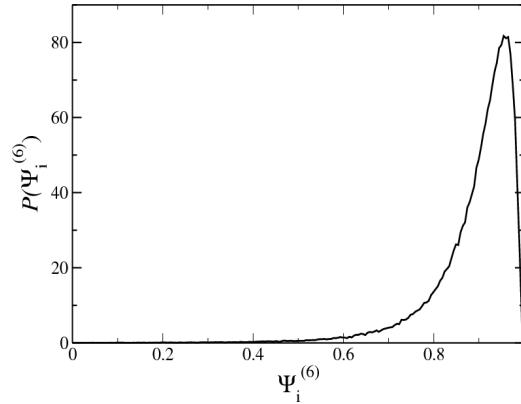


Figure 2.10: Bond-order parameter distribution $P(\Psi_i^{(6)})$ for $\phi = 0.4$ and $\kappa^* = 8$. It clearly reveals a sixfold symmetry of the lattice in the lateral direction.

lanes which has a short-ranged repulsive part and a long-ranged attractive interaction. The former is caused by friction between oppositely driven particles, while the latter just results from the bare Coulomb interaction. From the data we conclude that the positional order in the lane location is really long ranged. This is supported by a simulation of a system that is eight times bigger, as will be discussed in Sec. 2.4.2.

The next parameter combination is *high screening and high volume fraction*, $\phi = 0.4$ and $\kappa^* = 8$; see Fig. 2.9. Here the strong friction between

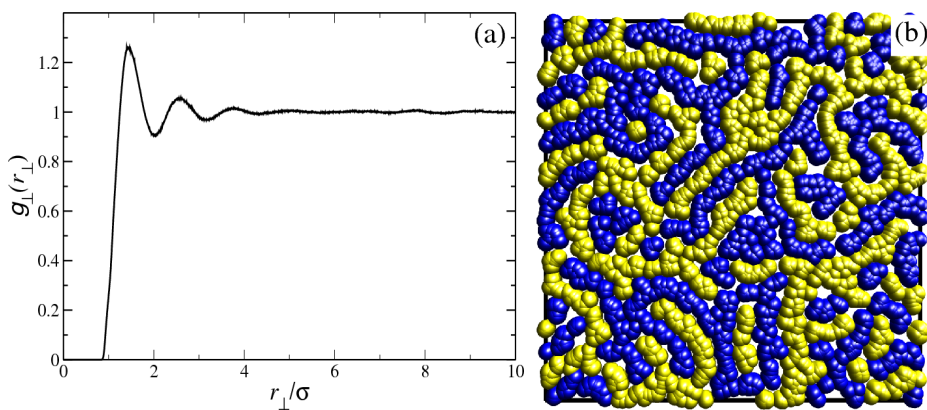


Figure 2.11: Same as Fig. 2.3 for $\phi = 0.1$ and $\kappa^* = 5$.

oppositely driven particles enforces lane formation, and the high density re-

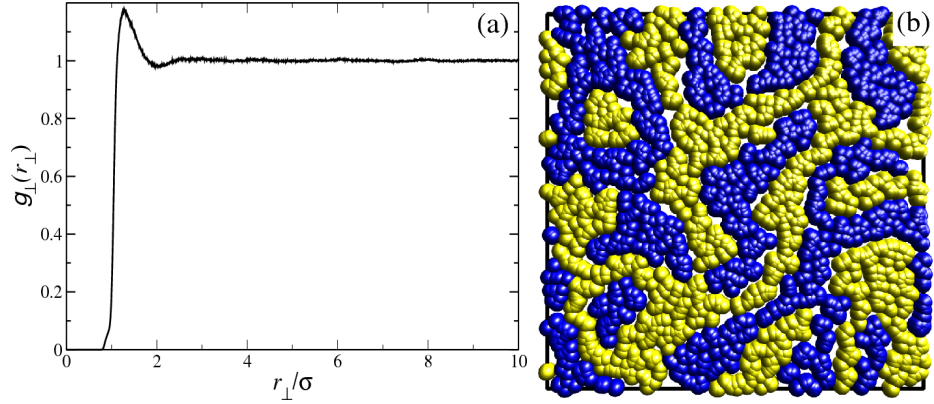


Figure 2.12: Same as Fig. 2.3 for $\phi = 0.1$ and $\kappa^* = 10$.

sults in a rhombic or triangular packing of different lanes. This lattice is then decorated with different charges. The sixfold symmetry of the lattice of this parameter combination is revealed by the averaged value of $\langle \Psi^{(6)} \rangle = 0.83$. The distribution of $\Psi_i^{(6)}$ is also shown in Fig. 2.10. For less screening, $\kappa^* \leq 3$, we find a rhombic lattice with a twofold symmetry.

Next we go for further intermediate cases. The most striking new state occurs at *high screening and intermediate volume fraction*; see Fig. 2.11 and 2.12, where data for $\phi = 0.1$ and $\kappa^* = 5$ and $\kappa^* = 10$ are shown. Here one encounters an in-plane structure reminiscent of a percolating network,

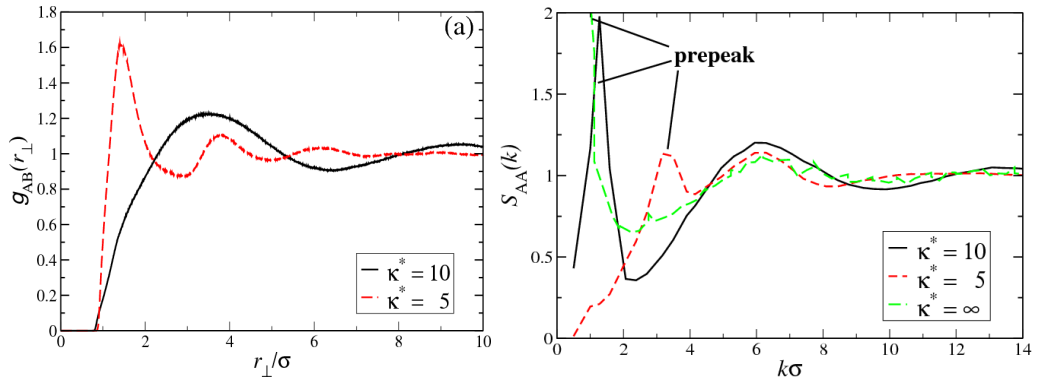


Figure 2.13: Pair distribution function $g_{AB}(\mathbf{r}_\perp)$ (a) and structure factor $S_{AA}(k)$ of like charged particles (b) for $\phi = 0.1$, $\kappa^* = 5$ and $\kappa^* = 10$. Additionally the structure factor for $\kappa \rightarrow \infty$ is shown. The latter indicates that the two particle species are separated by half of the box length.

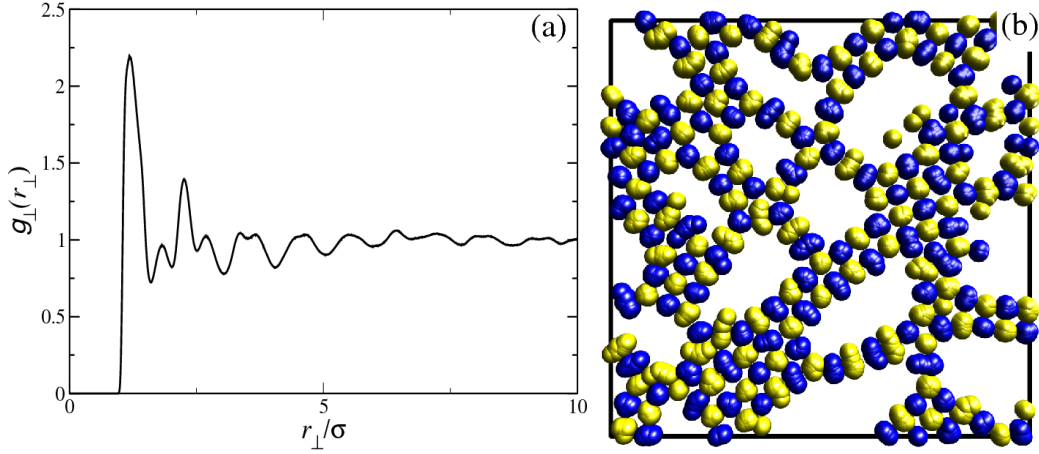


Figure 2.14: Same as Fig. 2.3 for $\phi = 0.1$ and $\kappa^* = 1$.

bicontinuous microemulsion, or microphase-separated system. We call this structure network like. It is characterized by liquid like order in the lateral direction [see Fig. 2.11(a) and 2.12(a)]. The prepeaks in the structure factors $S_{AA}(k)$ in 2.13(b) reveal an additional length scale that depends on the screening length κ^* . The peaks clearly show that the average thickness of the lateral regions of like-charged particles is significantly affected by the choice of κ^* . The characteristic spacing in this structure can be also extracted from the pair correlation function between the different particle species g_{AB} as defined in Eq. (2.13) [see Fig. 2.13(a)]. These result show that the characteristic spacing is increasing with increasing κ^* . This is also qualitatively supported from the projection snapshots in Fig. 2.11(b) and 2.12(b). In the limit of $\kappa \rightarrow \infty$, i.e., the interaction potential reduces to the repulsive core, we find that the characteristic spacing is half of the box length suggesting that the steady-state situation is a phase separated one.

Then we observed a mixed situation of two coexisting dynamical states. Coexisting states are characterized by two peaks in the appropriate bond-order parameter distribution, indicating that parts of the system are in a k -fold symmetry regime while other parts of the system are not. These results are summarized in Figs. 2.14 and 2.16. The former shows a coexistence between a region of no lanes and a square lattice phase which involves empty holes. The fourfold symmetry in the lattice is indicated by the second peak in the bond-order parameter distribution both depicted in Fig. 2.15(a). The prepeak in the structure factor $S_{\perp}(k)$ in Fig. 2.15(b) shows an additional length scale caused by the voids. But, as in the chaining situation, it is not completely clear whether this is a transient state toward a complete

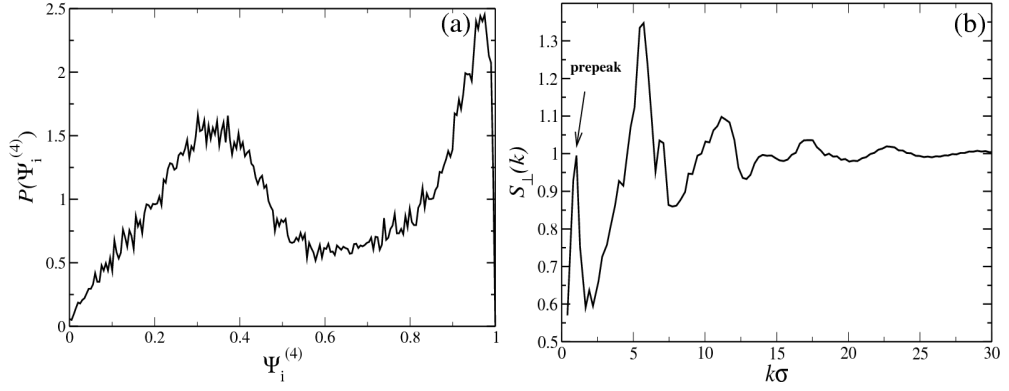


Figure 2.15: Bond-order parameter distribution $P(\psi_i^{(4)})$ (a) and structure factor $S_{\perp}(k)$ (b) for $\phi = 0.1$ and $\kappa^* = 1$.

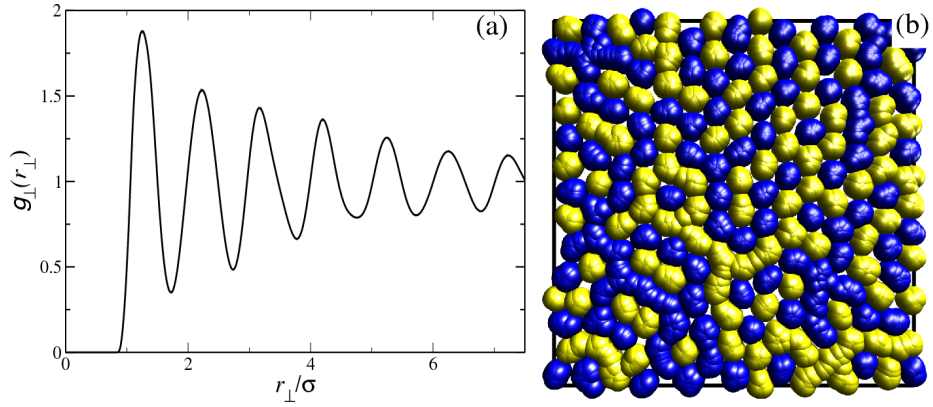


Figure 2.16: Same as Fig. 2.3 for $\phi = 0.3$ and $\kappa^* = 7$.

square lattice and no lanes phase separation, or whether this is a stable state. However, if a completely separated state is used as a different starting configuration, it stays stable over the time explored by the simulation.

Finally in the projected snapshot of Fig. 2.16(b) one observes both local network structures and parts with triangular crystallinity. The underlying sixfold symmetry is again revealed by the bond-order parameter distribution Fig. 2.17.

(b) Steady-state phase diagram

In Fig. 2.18 we present a nonequilibrium steady-state phase diagram for fixed driving force as a function of the screening parameter κ^* and the volume

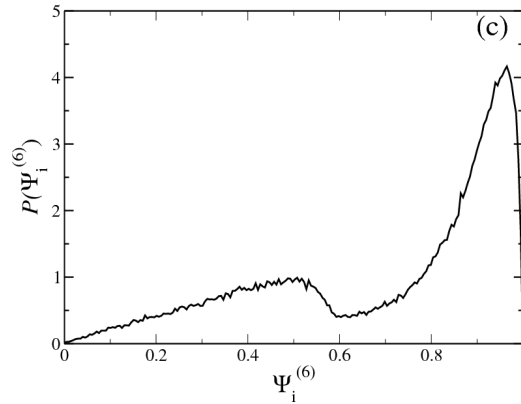


Figure 2.17: Bond-order parameter distribution $P(\Psi_i^{(6)})$ for $\phi = 0.3$ and $\kappa^* = 7$. It clearly reveals that parts of the system are in a sixfold symmetry while others are not.

fraction ϕ . In addition to the eight parameter combinations that were already discussed in detail, more data are collected here. There are stable states with no lanes, network-forming lanes, square, triangular, and rhombic lateral crystals of lanes, and associated coexistence situations. Solid lines separate the different states. The chain formation is shown as well. The broken line separating this state from the others indicates that we are not sure whether this is a transient state on the way to square and no-lane coexistence or a stable state. This phase diagram should be detectable in experiments on highly charged colloidal suspensions.

It is interesting to correlate our results with the phase diagram of the same system in equilibrium without an external field which was calculated by Hynninen *et al.* for $\kappa^* = 6$ and varying temperatures and volume fractions in [50]. Similar to our results, they find a variety of different stable states due to the competition between the repulsive core and the screened Coulombic attraction. Let us first go through the phase diagrams from low to high volume fractions for weak Coulomb coupling, which corresponds to high temperature in the phase diagram of Hynninen *et al.* and high screening in ours. In equilibrium one encounters first a fluid phase, then a fluid and fcc-disordered coexistence regime, and ends up in a fcc-disordered phase. Analogously, in our phase diagram we start from two regimes with no crystalline order, namely, no lanes and network, and go through a triangular lattice-network coexistence to a triangular lattice. This part of the phase diagram is in both cases mainly dominated by the repulsive core. For stronger Coulomb coupling, on the other hand, the equilibrium case reveals a broad

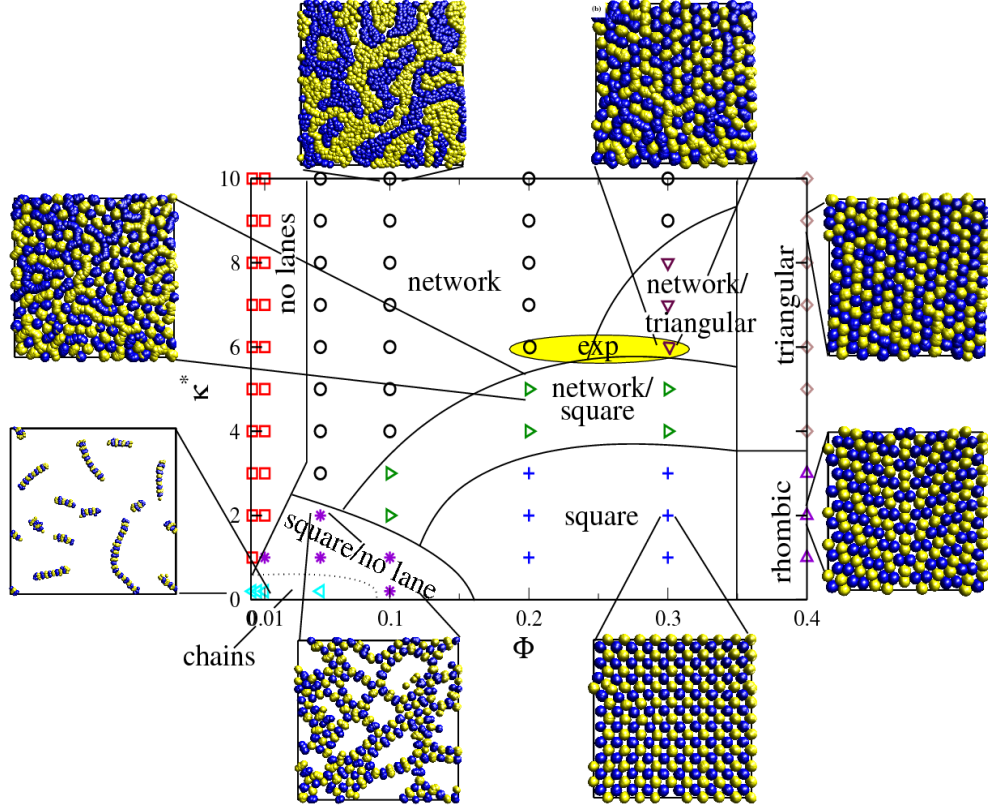


Figure 2.18: Nonequilibrium steady-state phase diagram for a constant driving force of strength $f^* = 236$. All different states described in Fig. 2.3 - 2.16 in the plane perpendicular to the external fields as a function of the inverse screening length κ^* and the volume fraction ϕ are displayed. The lines are a guide for the eye. Additionally, the yellow area indicates the parameter set for which laning was reported in [28].

gas-CsCl coexistence. The corresponding part in our phase diagram shows similarly a coexistence between a square lattice and no lanes including the special case of the chain regime. Finally, for higher packing fractions and strongly interacting particles, Hynninen *et al.* find three different crystal structures for increasing volume fractions: CuCl, CsCl, or tetragonal structure. In our case, we find analogously a transition from a square to a rhombic lattice. We emphasize, however, that this is just a qualitative comparison between an equilibrium and a nonequilibrium phase diagram.

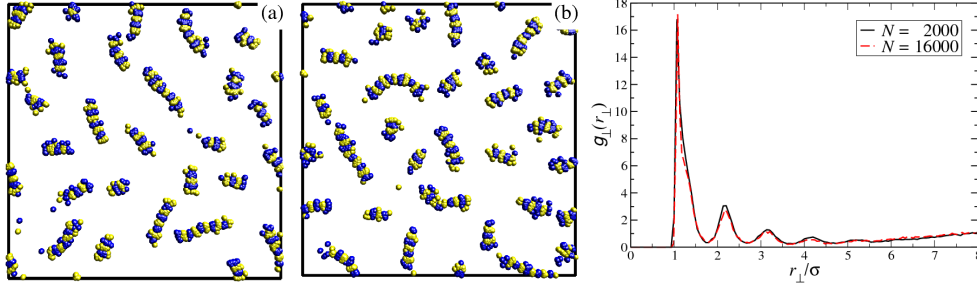


Figure 2.19: Projections of the particles' position onto the area perpendicular to the field for $\phi = 0.01$ and $\kappa^* = 0.2$ after an initial relaxation time of $10\tau_B$. (a) is the same plot as in Fig. 2.4(b). (b) shows the same setup but for $N = 16000$ particles. For (b) only 1/8 of the system is displayed to compare with the smaller system depicted in (a) on the same dimensions. Additionally, the pair distribution function $g_{\perp}(r_{\perp})$ for the two different system sizes after an initial relaxation time of $10\tau_B$ is presented.

(c) Finite system size effects

We have also addressed the issue whether the observed results are influenced by the system size and whether the periodic boundary conditions support lane formation. Therefore, we carried out several benchmark simulations with a system that is eight times bigger, i.e., $N = 16000$ particles. We applied the same external field as previously as well as a field tilted by 45 degrees such that lanes do not connect themselves due to the periodic boundary conditions. We compare the simulations to the previous results after the same initial simulation time. We find that the qualitative results are influenced neither by system size nor by the field direction. We further confirm that the quantitative results depend only weakly on the system size.

We exemplify this with two state points and compare them to earlier discussed results. First, we consider $\phi = 0.01$ and $\kappa^* = 0.2$. For this parameter combination, we find chains of lanes as reported in subsection 2.4.2. The same is holds for the larger system. Typical projections of the particles' position onto the area perpendicular to the field for $N = 2000$ and $N = 16000$ are presented in Fig. 2.19. For the larger system only 1/8 of the system is displayed to enable comparison on the same dimensions. Obviously we find qualitative agreement with the previously shown results. The quantitative agreement can be deduced from the pair distribution functions $g_{\perp}(r_{\perp})$ in Fig. 2.19. They reveal the same number of peaks, suggesting that the average width of a chain is nearly unaltered by the system size.

The second state point is $\phi = 0.1$ and $k^* = 10$, where we find a network

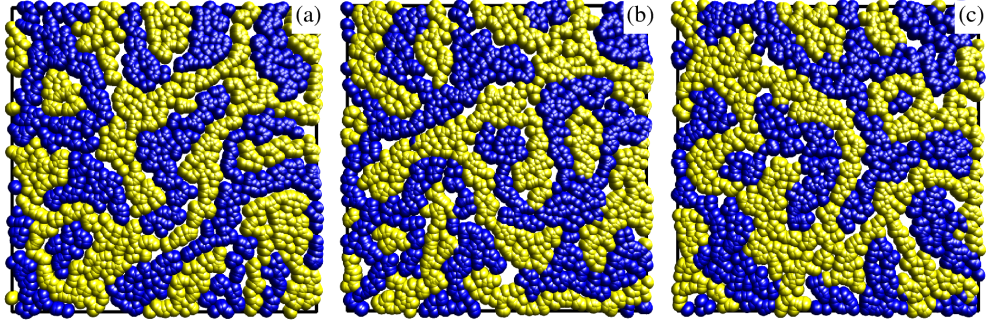


Figure 2.20: Projections of the particles' position onto the area perpendicular to the field for $\phi = 0.1$ and $\kappa^* = 10$. (a) Same plot as in Fig. 2.12(b). (b), (c) Same setup but for $N = 16000$ particles. In (c) the external driving field is tilted by 45 degrees such that the lanes do not connect themselves due to the periodic boundary conditions. For (b) and (c) only 1/8 of the system is displayed to compare with the smaller system depicted in (a) on the same dimensions.

like structure. In Fig. 2.20(a) and (b) the projected particle positions for the two system sizes with the same driving field are displayed. To make the point, for the larger system we again show only 1/8 of the system. Once again, the qualitative agreement is obvious. Quantitatively, we compare the pair distribution functions $g_{AB}(r_{\perp})$ in Fig. 2.21. It suggests that the characteristic spacing is more or less system-size independent.

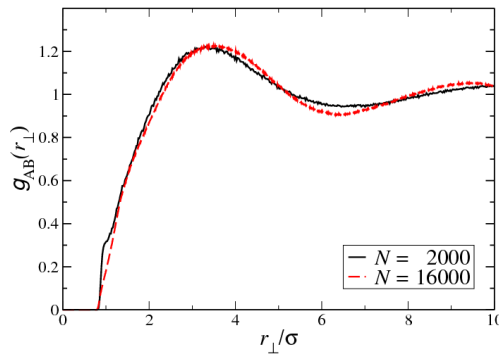


Figure 2.21: Pair distribution function $g_{AB}(r_{\perp})$ for $\phi = 0.1$ and $k^* = 10$ for two different system sizes $N = 2000$ and $N = 16000$.

The influence of the periodic boundary conditions, which support laning by connecting the lanes to each other when the driving field is along the box

orientation is also small, as can be seen when tilting the external driving field. We then find the same qualitative behavior, see Fig. 2.20(a) and (c). Here, we depict a simulation snapshot for an external field tilted by 45 degrees, i.e. $\mathbf{E}_i^{\text{ext}} = Z_i f(\mathbf{e}_y + \mathbf{e}_z)/\sqrt{2}$.

2.5 Influence of hydrodynamic interactions on lane formation in oppositely charged driven colloids

2.5.1 Introduction

In this section, the influence of hydrodynamic interactions on lane formation of oppositely charged driven colloidal suspensions is investigated using Brownian dynamics computer simulations performed on the Rotne-Prager level of the mobility tensor. Our motivation to do so is twofold: First, the experiments, of course, contain hydrodynamic interactions in their full glory, and therefore an inclusion of hydrodynamic interactions is needed for a quantitative comparison. Second, there is a principal need to understand in which direction hydrodynamics influence lane formation. Two cases are considered, namely sedimentation and electrophoresis. In the latter case the Oseen contribution to the mobility tensor is screened due to the opposite motion of counterions. The simulation results are compared to that resulting from simple Brownian dynamics where hydrodynamic interactions are neglected. For sedimentation, we find that hydrodynamic interactions strongly disfavor laning. In the steady-state, a macroscopic phase separation of lanes is observed here. This is in marked contrast to the simple Brownian case where a finite size of lanes was obtained in the steady-state. For strong Coulomb interactions between the colloidal particles a lateral square lattice of oppositely driven lanes is stable similar to the simple Brownian dynamics. In an electric field, on the other hand, the behavior is found in qualitative and quantitative accordance with the case of neglected hydrodynamics.

2.5.2 Results

Order parameter and steady-state phase diagrams

To assess the effect of hydrodynamic interactions on the lane behavior of oppositely charged colloidal particles we study a set of volume fractions ϕ and inverse screening lengths $\kappa^* = \kappa\sigma$ and map out nonequilibrium steady-state phase diagrams for three situations: hydrodynamic interactions neglected (A), electrophoresis (B), and sedimentation (C).

A state of lane is thereby identified by a laning order parameter that is defined in the previous Sec. 2.3. We observe that lanes form different structures in the plane perpendicular to the driving direction for different values of κ^* and ϕ [see also Sec. 2.4]. We find lanes placed on a square

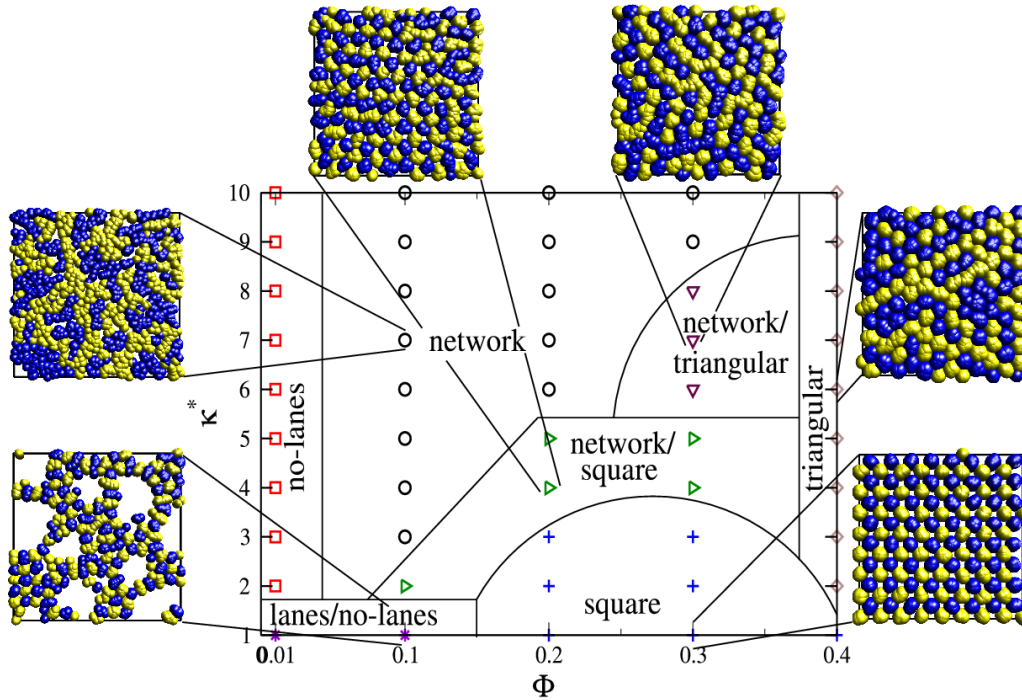


Figure 2.22: (Color online) Nonequilibrium steady-state phase diagram for a constant driving force of strength $f = 150k_B T/\sigma$ with hydrodynamic interactions neglected accompanied by a typical simulation snapshot of the projection of the particle coordinates onto the plane perpendicular to the driving field for each different state. The lines between the phases are a guide for the eye.

or triangular lattice, a network-like structure (reminiscent of a bicontinuous microemulsion or microphase-separated system), coexistence regimes of the same, and macroscopically separated lanes. The resulting nonequilibrium steady-state phase diagrams are shown in Fig. 2.22, 2.23, and 2.24. They are accompanied with typical simulation snapshots of the projection of all particle coordinates onto the xy -plane of the respective situation.

What can be seen at first sight is that the qualitative behavior of situation (A) and (B) in Fig. 2.22 and 2.23 is almost identical with only subtle differences, while on the other hand the phase behavior changes drastically for situation (C), Fig. 2.24. In the latter, the whole phase diagram is altered and the diversity of phases found is reduced compared to the first two cases.

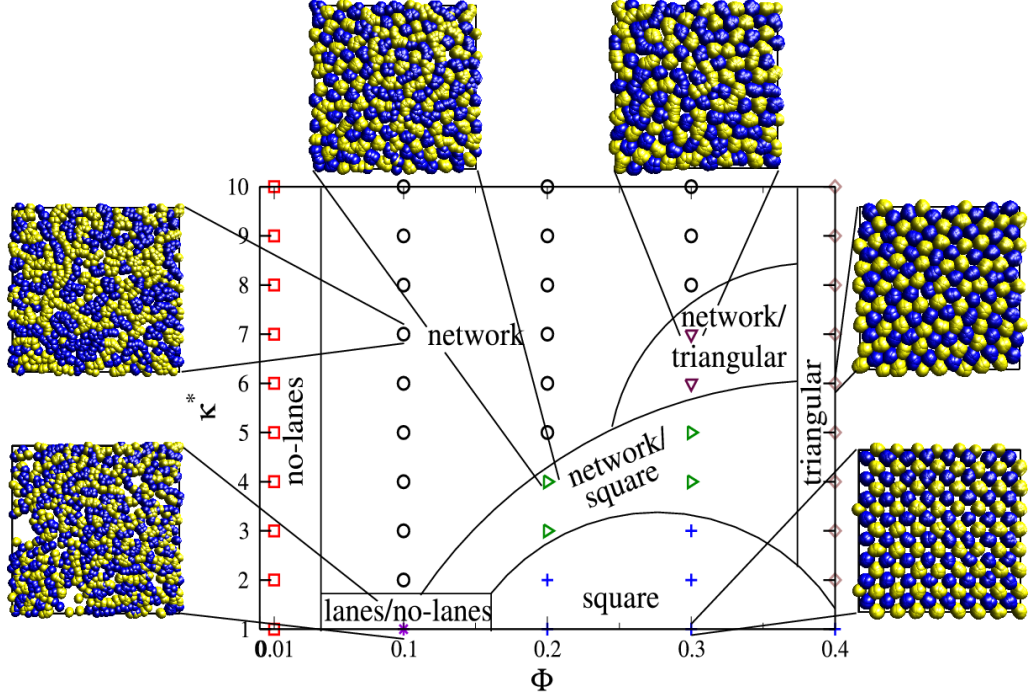


Figure 2.23: (Color online) Same as Fig. 2.22 but for electrophoresis with hydrodynamic interactions taken into account through μ_{ij}^{LA} in Eq. (2.9). The phase diagram reveals only minor differences as compared to the the case of neglected hydrodynamic interactions in Fig. 2.22.

Comparison of simulation results for neglected hydrodynamic interactions and electrophoresis

In this subsection, we briefly describe the two phase diagrams in Fig. 2.22 and 2.23 and their differences, beginning at low volume fractions and ending at high ones, and then dwell on the third diagram, Fig. 2.24, thereafter in subsection 2.5.2. A more ample discussion on how different phases are identified and what structural correlations they exhibit is given in the previous section 2.4 on the same system with hydrodynamic interactions neglected but for a stronger driving strength and larger systems [79]. Here, we find for situation (A) virtually the same results as in the previous section with only one difference, namely that we do not encounter a rhombic phase for $\phi = 0.4$ and $\kappa^* = 1, 2, 3$.

For very low volume fraction, $\phi \lesssim 0.01$, in both systems the correlations between particles are not sufficient to form lanes at all. Thus, the systems are in a phase of no lanes. Only for very low salt concentration, i.e. small κ^* ,

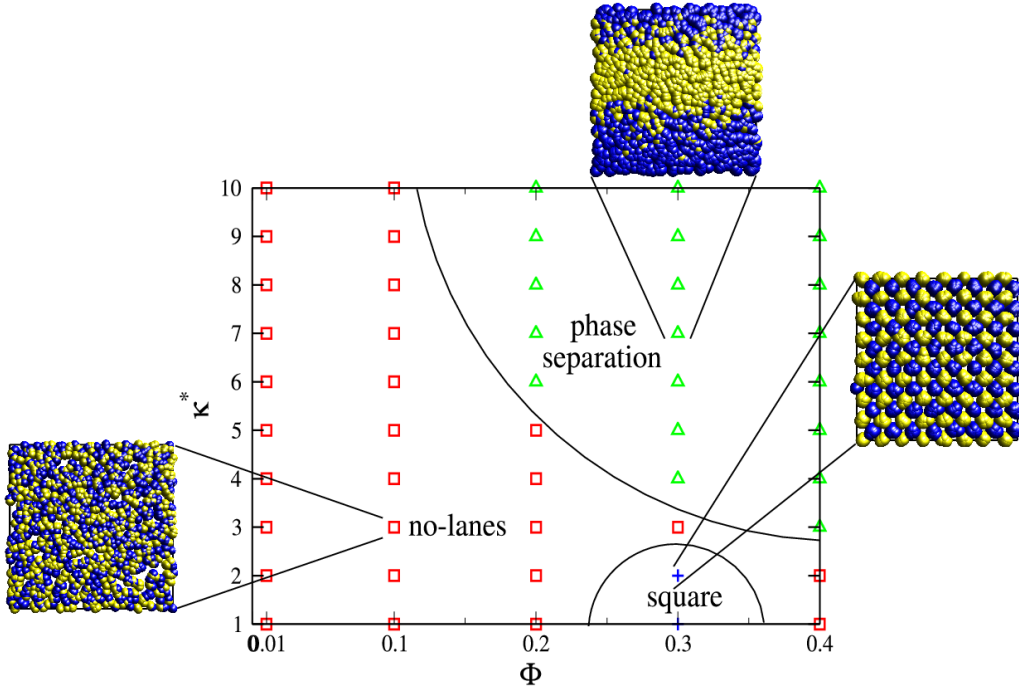


Figure 2.24: (Color online) Same as Fig. 2.22 but for sedimentation with hydrodynamic interactions taken into account through μ_{ij}^{RP} in Eq. (2.7). The phase diagram shows significant changes as compared to Fig. 2.22 and Fig. 2.23.

where the electrostatic coupling between the colloidal particles is strong, we find a coexistence region between lanes and no lanes. Here, the region with no lanes consists of voids, where hardly any particle is found. The structure of the lane region, on the other hand, is different in situation (A) and (B). For situation (A) the corresponding snapshot in Fig. 2.22 reveals fixed lattice points while the snapshot in Fig. 2.23, situation (B), shows a network-like structure. For situation (A), an initial configuration with lanes placed on a square lattice separated from a completely depleted region is stable in simulations, as well [see also Sec. 2.4.2]. Thus, we assume that in situation (A) the lanes/no lanes phase is a transient state toward a complete square lattice and no lane phase separation. Hydrodynamic interactions destroy the coexistence phase for $\phi = 0.01$. It only occurs in a denser system with $\phi = 0.1$ whereas in situation (A) this state shows already up at $\phi = 0.01$. Additionally, the voids are more pronounced in the latter case compared to situation (B). Upon increasing $\kappa^* \geq 2$ for $\phi = 0.1$ we find in both situations a network-like structure whose characteristic spacing is increasing with increasing κ^* .

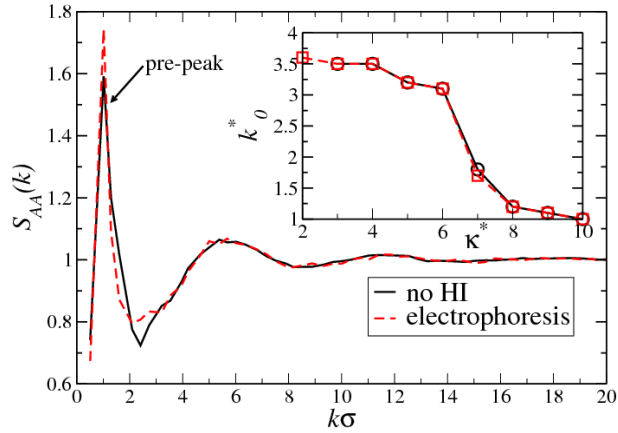


Figure 2.25: Partial structure factor $S_{\perp}(k)$ of like-charged particles perpendicular to the driving field for $\kappa^* = 10$ and $\phi = 0.1$ for hydrodynamics neglected and electrophoresis. The prepeak at $k_0^* = k_0\sigma$ indicates an additional length scale of the structure in the network-like phase. The inset shows the position k_0^* of the prepeak as a function of the inverse screening length κ^* for a fixed volume fraction of $\phi = 0.1$.

For situation (A) there is also a small coexistence region between network and square lattice at $\kappa^* = 2$ that is not present in (B).

To obtain a quantitative measure of the characteristic spacing in the network structure we determine a structure factor perpendicular to the driving field of like-charged particles. The steady-state partial structure factor has been calculated by evaluating expression 2.15. An example of the structure factors for $\kappa^* = 10$ and $\phi = 0.1$ for both situation, (A) and (B), is shown in Fig. 2.25. One clearly observes a pronounced prepeak at the wave number $k_0 \approx 1/\sigma$ in both cases. A prepeak in the structure factor is an indication of an additional mesoscopic length scale as typical for bicontinuous networks, such as e.g. microemulsions [70, 71]. In the inset, we additionally present the position $k_0^* = k_0\sigma$ of the prepeak as a function of the inverse screening length. It is evident from the picture that the characteristic spacing is indeed growing with increasing κ^* . We find hardly any difference between situation (A) and (B).

For $\phi = 0.2$ an additional phase for small inverse screening length shows up in both phase diagrams. Oppositely driven lanes are placed on a square lattice with an alternating charge pattern. The formation of this lattice structure can be qualitatively understood from an effective interaction between oppositely charged driven lanes which has a short-ranged repulsive and a long-ranged attractive interaction. The former stems from the friction

between oppositely driven particles while the later results form the Coulomb interaction. The square lattice then reduces the electrostatic energy of the system because each particle has only oppositely charged neighbors. For increasing salt concentrations we encounter a coexistence region between the square lattice and the network-like phase and finally end up in a pure network-like phase. The phase diagram is in both situations very similar, only the borders of the transitions are slightly shifted. In the electrophoresis case the network-like structure is preferred to the square lattice.

For a higher volume fractions of $\phi = 0.3$ a coexistence regime between a triangular lattice and a network-like structure is found. The lattice-points in the triangular phase are rather randomly decorated with different charges. Here, the short range repulsion plays the dominant role compared to the electrostatic interaction. It enforces a triangular lattice due to packing effects although electrostatically it is strongly disfavored because like-charged particles necessarily occupy lattice points next to each other. Again, hydrodynamic interactions slightly shift the phase boundaries to the network-like structure.

For the highest volume fraction studied, $\phi = 0.4$, both phase diagrams show exactly the same behavior. Here, the short range repulsions dictates the phase behavior for nearly all salt concentration but for $\kappa^* = 1$ and enforces lanes to be placed on a triangular lattice. Only for $\kappa^* = 1$, where electrostatic interactions are prominent, a square lattice is preferred. In principle a square lattice is possible up to the packing of $\phi = 0.52$, i.e. the closed packing of the simple cubic lattice.

In summary, we found very similar behavior in both situations. The observed differences can be qualitatively explained by the fact that hydrodynamic interactions disfavor lanes driven oppositely past each other.

Sedimentation

Regarding sedimentation, Fig. 2.24, the whole phase diagram exhibits *only* three different phases. For volume fractions $\phi \leq 0.1$ we do not find lane formation for all inverse screening length studied. For increasing volume fractions and strong electrostatic interactions, $\kappa^* \leq 2$, first the square lattice at $\phi \approx 0.3$, that is also present in the previous two situations, is recovered and then the system reenters a region with no lanes for $\phi = 0.4$. This behavior nicely illustrates the competition between hydrodynamic interactions disfavoring lanes driven oppositely past each other and the electrostatic interactions favoring a square lattice. Only for the small regime around $\phi \approx 0.3$ the electrostatics succeeds the hydrodynamic interactions and enforces a square lattice. For all other volume fractions laning is destroyed. However, for

stronger salt concentrations, where the Coulombic coupling is reduced, we discover a situation that is not present in the previous situations (A) and (B), namely a region with only two big completely separated lanes. We call this state *phase separated*. In that case the long ranged hydrodynamic interactions prescribe the structure and the short ranged Yukawa interaction plays its role only at the rough interface of the two phases. From our simulations we conclude the lanes are separated by half of the box length.

Drift velocity

Now, we study the influence of hydrodynamic interaction on the drift velocity along the field direction that is defined as follows

$$v^2 := \lim_{t \rightarrow \infty} \frac{\langle [(\mathbf{r}_i(t) - \mathbf{r}_i(0)) \cdot \mathbf{e}_z]^2 \rangle}{t^2}. \quad (2.18)$$

This entity measures the mean-square displacement of each particle in the nonequilibrium steady-state. A study on the effect of hydrodynamics on the drift velocity of like charged colloidal particles was carried out by Watzlawek and Nägele [80]. Here, we study two cases. First we fix the volume fraction at $\phi = 0.3$ and vary the inverse screening length and afterward vice versa for $\kappa^* = 1$.

In Fig. 2.26, we display $v^* = v/v_0$, where $v_0 = 150\sigma/\tau_B$ is the drift velocity of an infinitely diluted system, for a fixed volume fraction $\phi = 0.3$ as a function of the inverse screening length κ^* for all three situations. For all cases the drift velocity increases with decreasing Coulomb coupling because oppositely charged colloids attract each other while driven in opposite direction and lanes mutually retard each other. For very strongly screened particles where this friction is less important all three curves reveal approximately the same value of $v^* \approx 0.87$. Accordingly, this value approaches the drift velocity of a system of infinite dilution subjected to the same driving force. While in (A) and (B) v grows gradually, in the sedimentation curve we encounter a jump in the drift velocity between $\kappa^* = 3$ and $\kappa^* = 4$. This coincides with the transition from the no lane regime to the phase separated regime, see the phase diagram Fig. 2.24. On the other hand for $\kappa^* \leq 2$, where we find a square lattice, the drift velocity is similar to $\kappa^* = 3$. From that we conclude that the phase separated state of lanes supports particle transport while lanes placed on a square lattice, enforced by strong Coulombic interactions, slows down particle transportation. A further interesting feature is that curves for (A) and (B) intersect between $\kappa^* = 1$ and $\kappa^* = 2$ and that the screened hydrodynamic interaction enhance the drift velocity for larger inverse screening length. The same is true for the unscreened hydrodynamic

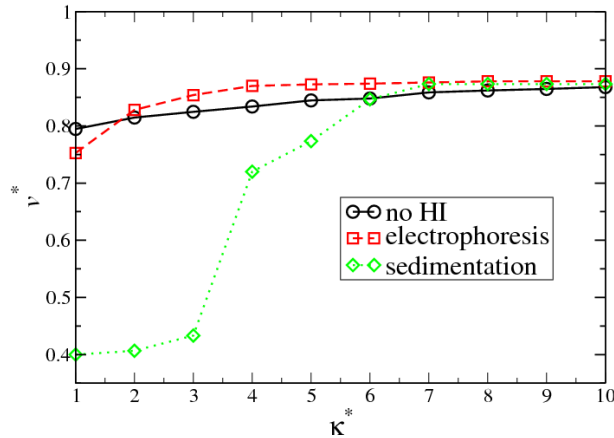


Figure 2.26: Average dimensionless drift velocity $v^* = v/v_0$ in drive direction as a function of the inverse screening length κ^* at $\phi = 0.3$ for Brownian dynamic simulations with hydrodynamic interactions neglected, taken into account through μ_{ij}^{LA} , and μ_{ij}^{RP} .

interactions in the sedimentation for $\kappa^* \geq 6$. When studying the drift velocity for a fixed inverse screening length but for varying volume fractions in Fig. 2.27, we find again an intersection point of the curves for situations (A) and (B). Here, the drift velocity in the electrophoresis reaches an approximately constant value of $v^* \approx 0.75$ for $\phi = 0.1 - 0.4$, whereas it gradually decreases when hydrodynamic interactions are neglected. For the sedimentation the drift velocity decreases monotonically. In contrast to the case of varying salt concentration we do not encounter a jump in the sedimentation drift velocity when entering the square lattice at $\phi = 0.3$ and reentering the no lane regime at $\phi = 0.4$.

Phase transition

Finally, we address the issue of the order of the laning phase transition. Therefore, we calculate the laning order parameter (2.11) as a function of the driving strength $f^* = f\sigma/k_{\text{B}}T$ for $\phi = 0.2$ and $\kappa^* = 6$, which correspond to the values of the experiment by Leunissen et al [28], for all three situations, (A), (B), and (C). Additionally, we also computed another laning order parameter Φ^{D} which was introduced by Dzubiella and co-workers [20]. This order parameter probes the particle density inhomogeneities along the field, which vanishes in an ideal lane configuration and is defined as follows. To every particle i an order parameter Φ_i^{D} is assigned, which is unity if the lateral distance $|\mathbf{r}_{i\perp} - \mathbf{r}_{j\perp}|$ to all oppositely charged particles j is larger than

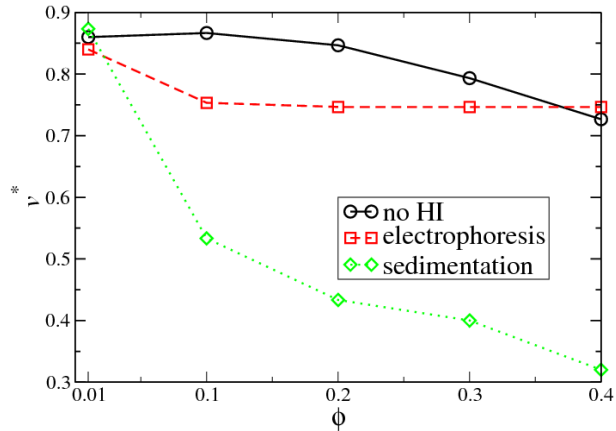


Figure 2.27: Average dimensionless drift velocity $v^* = v/v_0$ in drive direction as a function of the volume fractions ϕ at $\kappa^* = 1$ for Brownian dynamic simulations with hydrodynamic interactions neglected, taken into account through μ_{ij}^{LA} , and μ_{ij}^{RP} .

the cut-off $z_c = \frac{3}{4}\sigma$. Otherwise, Φ_i^D is set zero. The global order parameter Φ^D is then, analogously to Φ , defined as

$$\Phi^D = \frac{1}{N} \left\langle \sum_{i=1}^N \Phi_i^D \right\rangle_t, \quad (2.19)$$

The resulting curves are shown in Fig. 2.28. Two different situations are studied. We increase the field starting from a mixed configuration and decrease the field starting from the true lane state for $f^* = 200$. For situation (A) and (B) the latter is a network-like state, whereas for (C) it is a phase separated one. The results in Fig. 2.28(a) and (b) suggest that the transition in (A) and (B) is of second order with no hysteresis or jump in the order parameters. Instead we observe a gradual increase/decrease of Φ and Φ^D upon increasing/decreasing the strength of the external force. The results for the electrophoresis, Fig. 2.28(b), are in qualitative agreement with experimental data performed by Royall and co-workers [81]. A detailed comparison is current work in progress. In situation (C) on the other hand, the system is either in a phase separated state or in a no lane state, resulting in a jump in the order parameter. It is accompanied by a significant hysteresis. Thus, we conclude that the transition in (C) is first order. The results for Φ and Φ^D are qualitatively the same in all three situations.

In an earlier work by Dzubiella and co-workers [20], who studied a similar system but of like charged colloids driven in opposite directions without

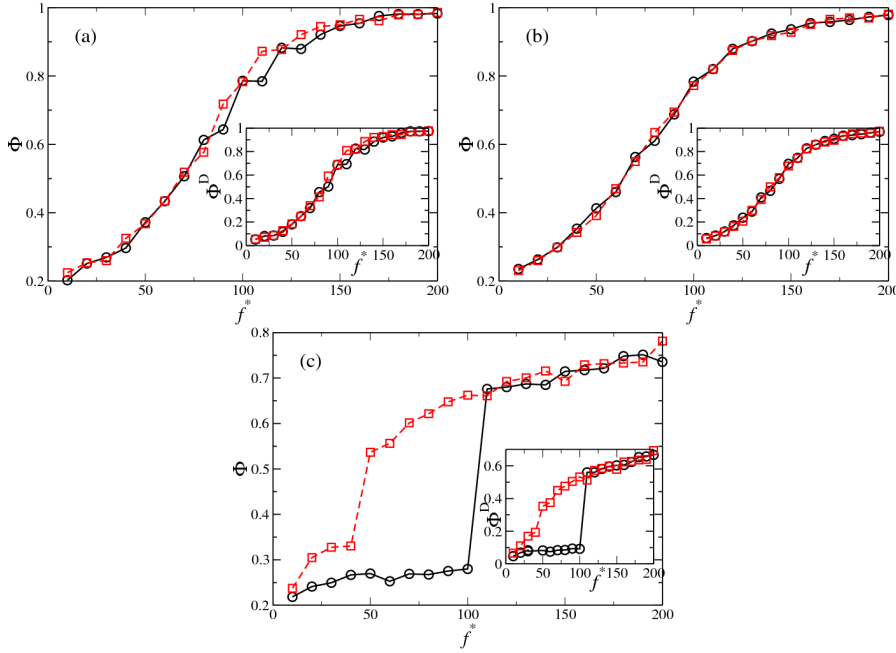


Figure 2.28: Dimensionless order parameters as defined in Eq. (2.11) and (2.19) (insets) as a function of the strength of the external driving force for hydrodynamic interactions neglected (a), for the electrophoresis (b), and for the sedimentation (c). Two different initial configurations are studied: the field is increased starting from a randomly mixed configuration (black curves) and the field is decreased starting from the steady-state configuration for $f^* = 200$ (red curve), that is in its state of lanes (compare Fig. 2.22-2.24).

hydrodynamic interactions, it was reported that the laning phase transition is of first order in a two-dimensional system using Φ^D . In a two-dimensional system lanes form stripes in field direction which are very stable once they are formed. Therefore, we conclude that the order of the transition depends on the dimensionality of the system.

2.6 Conclusions

In conclusion, in Sec. 2.4 we have analyzed steady-states in a driven mixture of oppositely charged colloidal particles which exhibit lane formation. By structural diagnostics, different states were distinguished via a different degree and order of the lanes. At high Coulomb coupling and low densities, a chaining of oppositely charged lanes was observed. Furthermore, there is

the possibility of lateral crystallization of lanes into two-dimensional square, triangular, or rhombic lattices. These states occur for high densities. In Sec. 2.5, we have investigated the influence of hydrodynamic interactions on lane formation of opposite charged colloids driven by an electric field or by gravity. Hydrodynamic interactions were included on the Rotne-Prager level. For an electric field, the leading Oseen term is screened due to the presence of counterions. The latter fact has led to very similar steady-state phase diagrams for an electric field as a driving source than that in the simple case of neglected hydrodynamic interactions. Again, various steady-state were obtained as a function of the colloidal density and the range of the interaction. They can qualitatively be understood in terms of a competition of the mutual Coulomb attraction and friction of sliding lanes. At high densities the lateral structure is crystalline, the crystal is either triangular as dictated by packing at high densities and high screening or square-like at low-screening which minimizes the Coulomb attractive energy. On the other hand, in sedimentation where the two colloidal species have the same buoyant mass up to a relative sign, friction of sliding lanes is strongly enhanced leading to macroscopic separation of lanes.

The steady-state phase diagram can in principle be verified in real-space experiments of charged suspensions which are driven in an electric field or sedimenting [28]. In the future, we shall focus on a detailed comparison between our simulation data and the experimental data. Work along these lines is in progress.

It would be interesting to check whether effective dipolar interactions between the charged particles which are mediated by the distorted counterion cloud around the colloids in an electric field are relevant. These forces favor aligning particles no matter how they are charged.

Further future work is to generalize the set-up to driven non-spherical particles like rod-like particle and/or to rod/plate mixtures where new effects are anticipated [82–84].

Also the special case of a mixture of charged and uncharged particles as recently studied by simulation in Ref. [85] should receive more attention and should be classified according to our structural criteria. It would be interesting to construct a microscopic theory for the lane transitions which includes the lateral crystalline structure. The instability analysis within a dynamical density functional theory as applied to the case of equal charges in two spatial dimensions [44, 86] should in principle be generalizable to the case of oppositely charged particles.

Finally, more sophisticated simulations schemes are needed in order to go beyond the Rotne-Prager level of approximation used in this chapter. Among the various promising approaches are the stochastic rotation dynamics code

[87, 88], a lattice Boltzmann theory including hydrodynamics [89–93] and counterion flow or the recently developed fluid particle dynamics methods [94–96].

Chapter 3

Dynamical density functional theory with hydrodynamic interactions

In this chapter, we derive a dynamical density functional theory (DDFT) for translational Brownian dynamics including hydrodynamic interactions on the two-particle level starting from Smoluchowski's equation for the time-evolution of the probability density. The theory reduces to the original version of the DDFT presented by Marconi and Tarazona [31, 33] when hydrodynamics are neglected. Using Rosenfeld's fundamental measure theory (FMT) for the density functional, we analyze the dynamics of a cluster of hard spheres trapped in an oscillating spherical optical trap which switches periodically in time from a stable confining to an unstable potential. The hydrodynamic interactions are treated as pair interactions on the Rotne-Prager level. The very accurate FMT functional allows us to scrutinize the quality of our theory. Additionally, we compare the results to those obtained when hydrodynamic interactions are ignored. We find that the predictions for the density profile are confirmed by those obtained by extensive Brownian dynamics simulations for moderate external forces. For strong external forces some discrepancies are observed.

3.1 Introduction

The dynamics of colloidal particles dispersed in a molecular solvent is by far less understood than their static behavior. The reason is that colloidal dynamics span a wide range of time-scales due to the enormous difference in size and mass of the colloidal particles and the host solvent molecules. The

obvious approach to this problem is to reduce the description of the solvent, when one is interested in the dynamics of the colloidal particles. While in equilibrium all solvent effects can be mapped on an effective interaction potential between the colloids, in nonequilibrium additional solvent effects need to be taken into account. These are: The friction of the colloids with the solvent, their Brownian motion due to random kicks of the solvent molecules, and solvent mediated interactions, the hydrodynamic interaction. This is either done by solving Langevin's equations of motion for the constituent particles, or by describing the time evolution of the probability density in configurational space. The former description takes the Brownian motion the particles perform explicitly into account and build the basis of computer simulations of colloidal dynamics (see previous chapter 2). A full microscopic theory for the time evolution of the probability density including hydrodynamic interactions through the mobility tensor is in principle given by the Smoluchowski equation. In practice, however, such a predictive theory is hampered by the many-body nature of the problem and the long range of the Oseen mobility tensor which is the leading contribution for a colloidal pair. Explicit approaches have been worked out in the bulk for short-time and long-time diffusion coefficients [97–99], and for the viscosity [100]. There are also first investigations for colloids near walls and on interfaces [101, 102] but a general theory for an arbitrary and time-dependent inhomogeneous external potential is missing.

A promising approach to describing the dynamics of colloidal particles is DDFT which is based on the classical density functional theory (DFT). DFT is a microscopic theory which starts from the interparticle interactions and bulk fluid correlations as an input. It predicts the inhomogeneous density profiles in an external potential including strongly inhomogeneous situations like freezing, for reviews see [30, 103]. The key quantity is the excess (“over ideal-gas”) free energy density functional, which is in general unknown. However, to date very accurate approximations for various interparticle interactions are available. For example, Rosenfeld's fundamental measure theory [104, 105] has been shown to be reliable for hard spheres, and the mean-field approximation is asymptotically correct for soft core interaction at high densities [38, 106, 107].

While it is by now well understood how to extract the static equilibrium properties of an inhomogeneous system from density functional theory, its extension toward time-dependent dynamical situations in nonequilibrium is more challenging. Recently, a DDFT was developed [31, 33, 34] where hydrodynamic interactions are ignored. DDFT results for the nonequilibrium dynamics of inhomogeneous Brownian fluids were found to agree with simulation data [39, 40, 108]. Further important activities in developing the

dynamical extension of DFT lie in the existence proof of the dynamical functional [35], its applicability to Newtonian dynamics [109] and to include fluctuations and noise effects [110]. Still lacking to date is how hydrodynamic interactions are to be treated in the DDFT formalism. Some attempts have been carried out by including hydrodynamic interaction effects in a density dependent diffusion coefficient [37]. Here, we present a stringent derivation of a DDFT which takes hydrodynamic interactions on a two-particle level into account without making further approximations than those underlying the DDFT of Marconi and Tarazona.

This chapter is laid out as follows. In Sec. 3.2, starting from the Smoluchowski equation, we derive a generalized dynamical density functional theory which includes hydrodynamic interactions. Sec. 3.3 is devoted to describing the system and the associated free energy functional. In Sec. 3.4 we present the results obtained by DDFT and Brownian dynamics simulations. Finally, in Sec. 3.5 we draw some conclusions.

3.2 Equation of motion for the one-body density

To derive a functional theory for the one-body density $\rho(\mathbf{r}, t)$ including hydrodynamic interactions, we start from the equation for the time-evolution of the full probability density distribution $P(\mathbf{r}^N, t)$ for N interacting spherical Brownian particles at positions $\mathbf{r}^N = \mathbf{r}_1, \mathbf{r}_2, \dots, \mathbf{r}_N$, i.e., the Smoluchowski equation (see e.g. [10]):

$$\frac{\partial P(\mathbf{r}^N, t)}{\partial t} = \sum_{i=1}^N \sum_{j=1}^N \nabla_i \cdot \mathbf{D}_{ij}(\mathbf{r}^N) \cdot [\nabla_j + \beta \nabla_j U(\mathbf{r}^N, t)] P(\mathbf{r}^N, t), \quad (3.1)$$

where $\mathbf{D}_{ij}(\mathbf{r}^N)$ is the diffusion tensor, $\beta^{-1} = k_B T$ is the thermal energy, and $U(\mathbf{r}^N, t)$ is the total potential energy of the system. By using the Smoluchowski equation the description of the complex fluid is reduced to one based solely on the position coordinates of the colloids, rather than utilizing the full set of phase space coordinates for the colloid and solvent particles. The solvent mediated interactions, the hydrodynamic interactions, are then included through the configuration-dependent diffusion tensor $\mathbf{D}_{ij}(\mathbf{r}^N)$. In our approach, we approximate the diffusion tensor by $\mathbf{D}_{ij}(\mathbf{r}^N) \approx D_0 \mathbf{1} \delta_{ij} + \mathbf{D}_{ij}^{(2)}(\mathbf{r}^N)$, i.e., on a two particle level. D_0 denotes the diffusion constant of a single iso-

lated particle, δ_{ij} is Kronecker's delta, and

$$\mathbf{D}_{ij}^{(2)}(\mathbf{r}^N) = D_0 \left[\delta_{ij} \sum_{l \neq i}^N \boldsymbol{\omega}_{11}(\mathbf{r}_i - \mathbf{r}_l) + (1 - \delta_{ij}) \boldsymbol{\omega}_{12}(\mathbf{r}_i - \mathbf{r}_j) \right]. \quad (3.2)$$

For a one-component suspension of spheres, series expansions of the two tensors $\boldsymbol{\omega}_{11}$ and $\boldsymbol{\omega}_{12}$ are known, in principle, to arbitrary order [111]. We further assume pairwise additivity for the total potential energy of the system, such that $U(\mathbf{r}^N, t)$ reads as:

$$U(\mathbf{r}^N, t) = \sum_{i=1}^N V_{\text{ext}}(\mathbf{r}_i, t) + \frac{1}{2} \sum_{i=1}^N \sum_{j \neq i}^N v_2(\mathbf{r}_i, \mathbf{r}_j), \quad (3.3)$$

where $V_{\text{ext}}(\mathbf{r}, t)$ is the one-body time-dependent external potential acting on each particle and $v_2(\mathbf{r}_i, \mathbf{r}_j)$ is the pair potential. To obtain an equation for the time-evolution of the one-body density, we note that the n -body densities are given by integrals over the probability density:

$$\rho^{(n)}(\mathbf{r}^n, t) = \frac{N!}{(N-n)!} \int d\mathbf{r}_{n+1} \dots \int d\mathbf{r}_N P(\mathbf{r}^N, t) \quad (3.4)$$

Thus, by integrating Eq. (3.1) with $N \int d\mathbf{r}_2 \dots \int d\mathbf{r}_N$, we obtain the following equation for the one-body density:

$$\begin{aligned} \Gamma^{-1} \frac{\partial \rho(\mathbf{r}, t)}{\partial t} = & \left\{ \nabla_{\mathbf{r}} \cdot \left[k_{\text{B}} T \nabla_{\mathbf{r}} \rho(\mathbf{r}, t) + \rho(\mathbf{r}, t) \nabla_{\mathbf{r}} V_{\text{ext}}(\mathbf{r}, t) + \right. \right. \\ & \left. \left. \int d\mathbf{r}' \rho^{(2)}(\mathbf{r}, \mathbf{r}', t) \nabla_{\mathbf{r}} v_2(\mathbf{r}, \mathbf{r}') \right] \right\} + \\ & \nabla_{\mathbf{r}} \cdot \int d\mathbf{r}' \boldsymbol{\omega}_{11}(\mathbf{r} - \mathbf{r}') \cdot \left\{ k_{\text{B}} T \nabla_{\mathbf{r}} \rho^{(2)}(\mathbf{r}, \mathbf{r}', t) + \nabla_{\mathbf{r}} [V_{\text{ext}}(\mathbf{r}, t) + v_2(\mathbf{r}, \mathbf{r}')] \right. \\ & \left. \rho^{(2)}(\mathbf{r}, \mathbf{r}', t) + \int d\mathbf{r}'' \rho^{(3)}(\mathbf{r}, \mathbf{r}', \mathbf{r}'', t) \nabla_{\mathbf{r}} v_2(\mathbf{r}, \mathbf{r}'') \right\} + \\ & \nabla_{\mathbf{r}} \cdot \int d\mathbf{r}' \boldsymbol{\omega}_{12}(\mathbf{r} - \mathbf{r}') \cdot \left\{ k_{\text{B}} T \nabla_{\mathbf{r}'} \rho^{(2)}(\mathbf{r}, \mathbf{r}', t) + \nabla_{\mathbf{r}'} [V_{\text{ext}}(\mathbf{r}', t) + v_2(\mathbf{r}, \mathbf{r}')] \right. \\ & \left. \rho^{(2)}(\mathbf{r}, \mathbf{r}', t) + \int d\mathbf{r}'' \rho^{(3)}(\mathbf{r}, \mathbf{r}', \mathbf{r}'', t) \nabla_{\mathbf{r}'} v_2(\mathbf{r}', \mathbf{r}'') \right\}, \quad (3.5) \end{aligned}$$

where Γ is the mobility constant for which the Einstein relation gives $D_0/\Gamma = \beta$. Eq. (3.5) still depends on both the time-dependent two-body

and the three-body densities. We will cast those into a form involving exclusively the free energy functional $\mathcal{F}[\rho]$ by making use of static DFT [29] and the Yvon-Born-Green (YBG) relations (see, e.g., [9]). To that end, we regard an out-of-equilibrium system at time $t = t_0$ with the instantaneous density profile $\rho(\mathbf{r}, t_0)$, whose time-evolution is given by Eq. (3.5). From static DFT it is known that every equilibrium density profile $\rho_0(\mathbf{r})$ is brought about by a unique external potential $\Phi_{\text{ext}}(\mathbf{r})$. Thus, we can identify the out-of-equilibrium instantaneous density with an equilibrium one of a reference system exposed to an accordingly chosen unique external potential $\Phi_{\text{ext}}(\mathbf{r}, t_0) = u(\mathbf{r}, t_0) + V_{\text{ext}}(\mathbf{r}, t_0)$, such that $\rho_0(\mathbf{r}) = \rho(\mathbf{r}, t_0)$. This holds for every point in time and therefore $\Phi_{\text{ext}}(\mathbf{r}, t)$, the additional potential $u(\mathbf{r}, t)$, and the equilibrium reference density $\rho_t(\mathbf{r})$ depend parametrically on time t . In equilibrium, a generalized force balance equation can be proved [29]

$$\frac{k_{\text{B}}T\nabla\rho_t(\mathbf{r})}{\rho_t(\mathbf{r})} + \nabla\Phi_{\text{ext}}(\mathbf{r}, t) = -\nabla\left.\frac{\delta\mathcal{F}_{\text{exc}}[\rho]}{\delta\rho}\right|_{\rho=\rho_t(\mathbf{r})}, \quad (3.6)$$

with the excess free energy functional $\mathcal{F}_{\text{exc}}[\rho]$. A simple reorganization (recall that $u(\mathbf{r}, t)$ is chosen such that $\rho_t(\mathbf{r}) = \rho(\mathbf{r}, t)$ at each point in time) yields:

$$\nabla u(\mathbf{r}, t) = -\nabla\frac{\delta\mathcal{F}[\rho]}{\delta\rho(\mathbf{r}, t)} \equiv -\nabla\mu(\mathbf{r}, t). \quad (3.7)$$

with the free energy functional

$$\mathcal{F}[\rho] = k_{\text{B}}T \int d\mathbf{r} \rho(\mathbf{r}, t) [\ln(\Lambda^3\rho(\mathbf{r}, t)) - 1] + \mathcal{F}_{\text{exc}}[\rho] + \int d\mathbf{r} \rho(\mathbf{r}, t) V_{\text{ext}}(\mathbf{r}, t). \quad (3.8)$$

Λ denotes the thermal de Broglie wavelength. $\mu(\mathbf{r}, t)$ is usually interpreted as a local nonequilibrium chemical potential. In the nonequilibrium system, the gradient of the chemical potential is the thermodynamic driving force. $\nabla u(\mathbf{r}, t)$ may therefore be envisaged as the additional external force which is necessary to balance the thermodynamic driving force in the equilibrium reference system. In the latter, additionally the YBG-hierarchy holds, whose first two members read as [9]:

$$\begin{aligned} k_{\text{B}}T\nabla_{\mathbf{r}}\rho_t(\mathbf{r}) + \rho_t(\mathbf{r})\nabla_{\mathbf{r}}[V_{\text{ext}}(\mathbf{r}, t) + u(\mathbf{r}, t)] + \int d\mathbf{r}' \rho_t^{(2)}(\mathbf{r}, \mathbf{r}')\nabla_{\mathbf{r}}v_2(\mathbf{r}, \mathbf{r}') &= 0 \\ \Leftrightarrow \\ -\rho_t(\mathbf{r})\nabla_{\mathbf{r}}u(\mathbf{r}, t) &= k_{\text{B}}T\nabla_{\mathbf{r}}\rho_t(\mathbf{r}) + \rho_t(\mathbf{r})\nabla_{\mathbf{r}}V_{\text{ext}}(\mathbf{r}, t) + \\ &\int d\mathbf{r}' \rho_t^{(2)}(\mathbf{r}, \mathbf{r}')\nabla_{\mathbf{r}}v_2(\mathbf{r}, \mathbf{r}') \end{aligned} \quad (3.9)$$

and

$$\begin{aligned}
 & k_{\text{B}}T\nabla_{\mathbf{r}'}\rho_t^{(2)}(\mathbf{r},\mathbf{r}') + \nabla_{\mathbf{r}'}[V_{\text{ext}}(\mathbf{r}',t) + u(\mathbf{r}',t) + v_2(\mathbf{r},\mathbf{r}')] \rho_t^{(2)}(\mathbf{r},\mathbf{r}') + \\
 & \quad \int d\mathbf{r}'' \rho_t^{(3)}(\mathbf{r},\mathbf{r}',\mathbf{r}'')\nabla_{\mathbf{r}'}v_2(\mathbf{r}',\mathbf{r}'') = 0 \\
 & \quad \Leftrightarrow \\
 & -\rho_t^{(2)}(\mathbf{r},\mathbf{r}')\nabla_{\mathbf{r}'}u(\mathbf{r}',t) = \nabla_{\mathbf{r}'}[V_{\text{ext}}(\mathbf{r}',t) + v_2(\mathbf{r},\mathbf{r}')] \rho_t^{(2)}(\mathbf{r},\mathbf{r}') + \\
 & \quad k_{\text{B}}T\nabla_{\mathbf{r}'}\rho_t^{(2)}(\mathbf{r},\mathbf{r}') + \int d\mathbf{r}'' \rho_t^{(3)}(\mathbf{r},\mathbf{r}',\mathbf{r}'')\nabla_{\mathbf{r}'}v_2(\mathbf{r}',\mathbf{r}''). \quad (3.10)
 \end{aligned}$$

The two right-hand sides in the second lines of equations (3.9) and (3.10) occur in the dynamical (nonequilibrium) context, Eq. (3.5). The basic assumption now, which also underlies the original version of the DDFT [31,33,34], is to use these expressions in the nonequilibrium situation, i.e., we approximate the two-body and three-body densities by those of the reference system with the same one-body density: $\rho^{(2)}(\mathbf{r},\mathbf{r}',t) \approx \rho_t^{(2)}(\mathbf{r},\mathbf{r}')$ and $\rho^{(3)}(\mathbf{r},\mathbf{r}',\mathbf{r}'',t) \approx \rho_t^{(3)}(\mathbf{r},\mathbf{r}',\mathbf{r}'')$. Inserting equations (3.7), (3.9), and (3.10) into Eq. (3.5) we obtain our central result

$$\begin{aligned}
 \Gamma^{-1}\frac{\partial\rho(\mathbf{r},t)}{\partial t} &= \nabla_{\mathbf{r}}\left[\rho(\mathbf{r},t)\nabla_{\mathbf{r}}\frac{\delta\mathcal{F}[\rho(\mathbf{r},t)]}{\delta\rho(\mathbf{r},t)}\right] + \\
 \nabla_{\mathbf{r}}\cdot\int d\mathbf{r}'\rho^{(2)}(\mathbf{r},\mathbf{r}',t)\boldsymbol{\omega}_{11}(\mathbf{r}-\mathbf{r}')\cdot\nabla_{\mathbf{r}}\frac{\delta\mathcal{F}[\rho]}{\delta\rho(\mathbf{r},t)} &+ \\
 \nabla_{\mathbf{r}}\cdot\int d\mathbf{r}'\rho^{(2)}(\mathbf{r},\mathbf{r}',t)\boldsymbol{\omega}_{12}(\mathbf{r}-\mathbf{r}')\cdot\nabla_{\mathbf{r}'}\frac{\delta\mathcal{F}[\rho]}{\delta\rho(\mathbf{r}',t)}. & \quad (3.11)
 \end{aligned}$$

Note that the first part on the right hand side of Eq. (3.11) is identical to the original DDFT of Marconi and Tarazona [31,33].

Finally, we need to close the above relation, which still depends on the two-body density. Within the central approximation $\rho^{(2)}(\mathbf{r},\mathbf{r}',t) = \rho_0^{(2)}(\mathbf{r},\mathbf{r}')$, the latter is given at every point in time by the exact generalized Ornstein-Zernike equation [29]:

$$\begin{aligned}
 \rho^{(2)}(\mathbf{r},\mathbf{r}',t) &= \rho(\mathbf{r},t)\rho(\mathbf{r}',t)\left(1 + \beta\frac{\delta^2\mathcal{F}_{\text{exc}}[\rho]}{\delta\rho(\mathbf{r},t)\delta\rho(\mathbf{r}',t)}\right) + \\
 \rho(\mathbf{r}',t)\int d\mathbf{r}''(\rho^{(2)}(\mathbf{r},\mathbf{r}'',t) - \rho(\mathbf{r},t)\rho(\mathbf{r}'',t))\beta\frac{\delta^2\mathcal{F}_{\text{exc}}[\rho]}{\delta\rho(\mathbf{r}',t)\delta\rho(\mathbf{r}'',t)}. & \quad (3.12)
 \end{aligned}$$

In conclusion, we derived a closed system of two equations that involves exclusively the equilibrium free energy functional $F[\rho]$ to obtain the time-evolution of the one-body density, including hydrodynamic interactions on the two-body level. The only assumption in the derivation was that the out-of-equilibrium two-body and three-body densities are approximated by those

of an equilibrium system with the same instantaneous density. This assumption seems reasonable, since we consider overdamped Brownian dynamics, for which the momentum degrees of freedom relax instantaneously. Imagine one actually switches on $u(\mathbf{r}, t)$, then the density of the out-of-equilibrium system is instantaneously the same as its equilibrium one, and “only” the n -body densities have to relax to their equilibrium values. Within our assumption this happens instantly. This central assumption, sometimes referred to as *adiabatic approximation*, was first suggested by Marconi and Tarazona [33]. To date, a number of studies have demonstrated the accuracy of this approximation in a variety of different systems, see e.g. [34, 36–40]. However, it is supposed to work best in relaxational dynamics.

3.3 The model

As a demonstration of the method presented in the previous section, the time-evolution of the one-body density with hydrodynamic interactions is predicted by Eq. (3.11) for a cluster of $N = 100$ monodisperse spherical particles of diameter σ , whose interaction is hard, i.e.,

$$v_2(r_{ij}) = \begin{cases} \infty & \text{if } r_{ij} \leq \sigma \\ 0 & \text{else} \end{cases}, \quad (3.13)$$

with $r_{ij} = |\mathbf{r}_i - \mathbf{r}_j|$. Henceforth, σ serves as the unit of length, the appropriate time scale is $\tau_B = \sigma^2/D_0$, and the energy unit is $k_B T$. The particles are trapped in a fixed soft spherical cavity which is supposed to be generated by light fields. Thus, it only acts on the colloidal particles but is penetrable for the solvent molecules and the solvent is therefore treated as an unbounded fluid. The particles are then driven to the shell or to the center of the cavity by a second light field in an oscillatory manner. The total external potential reads as

$$V_{\text{ext}}(r) = V_0 \left(\frac{r}{R_0} \right)^4 + (-1)^{\Theta(\sin(2\pi t/T))} V_D \left(\frac{r}{R_D} \right)^2, \quad (3.14)$$

where $r = |\mathbf{r}|$ and $\Theta(x)$ is the step function. $R_0 = 4\sigma$ and $V_0 = 10k_B T$ are the length scale and the strength of the outer fixed potential and $R_D = \sigma$ and $V_D = k_B T$ are the length scale and strength of the driving potential, respectively. $T = \tau_B$ is the period with which the inner potential switches instantaneously. Due to the spherical symmetry, the density profile $\rho(r, t)$ depends on only one effective coordinate, namely the absolute value of the coordinate vector.

We argued in the preceding section that the DDFT needs an accurate excess free energy functional as an input. For a hard-sphere liquid, Rosen-

feld's FMT [104] provides a very reliable approximation scheme for $\mathcal{F}_{\text{exc}}[\rho]$. Its accuracy in spherical confinement was demonstrated by González and co-workers [112, 113]. FMT is a generalized form of weighted-density approximations for fluids designed to model hard objects. In contrast to conventional weighted-density approaches, the free energy density is taken to be a function of not just one but of several different weighted densities. Though Rosenfeld's original work was proposed to describe hard sphere mixtures, to date several generalizations to other hard objects are available [114]. The weighted densities are obtained by convolutions with weight-functions, where a spatial convolution is given by $g(\mathbf{r}) * h(\mathbf{r}) = \int d\mathbf{x} g(\mathbf{x})h(\mathbf{r} - \mathbf{x})$. The weight-functions are geometrical properties of the constituent objects. For spherical particles they are given by

$$w_3(\mathbf{r}) = \Theta(R - r), \quad w_2(\mathbf{r}) = \delta(R - r), \quad (3.15)$$

$$\mathbf{w}_{v2}(\mathbf{r}) = w_2(\mathbf{r})\mathbf{r}/r, \quad \mathbf{w}_{m2}(\mathbf{r}) = w_2(\mathbf{r})[\mathbf{r}\mathbf{r}/r^2 - \mathbf{1}/3], \quad (3.16)$$

and the linearly dependent weights

$$w_1(\mathbf{r}) = \frac{w_2(\mathbf{r})}{4\pi R}, \quad \mathbf{w}_{v1}(\mathbf{r}) = \frac{\mathbf{w}_{v2}(\mathbf{r})}{4\pi R}, \quad \mathbf{w}_0(\mathbf{r}) = \frac{w_1(\mathbf{r})}{R}. \quad (3.17)$$

$\delta(x)$ is the Dirac distribution, and $R = \sigma/2$ is the radius of the spheres. $\mathbf{r}\mathbf{r}$ denotes a dyadic product and $\mathbf{1}$ the 3×3 identity matrix. Convolution with the density $\rho(\mathbf{r})$ yields the weighted densities

$$n_\nu(\mathbf{r}) = \rho(\mathbf{r}) * w_\nu(\mathbf{r}), \quad \nu = 3, 2, 1, 0, v2, v1, m2. \quad (3.18)$$

The excess free energy functional is obtained by integrating over a free energy density,

$$\beta\mathcal{F}_{\text{exc}}[\rho] = \int d\mathbf{r} \Phi(\{n_\nu\}), \quad (3.19)$$

where the reduced free energy density Φ is a simple function as opposed to a functional of the weighted densities n_ν and reads as:

$$\begin{aligned} \Phi = & -n_0 \ln(1 - n_3) + \frac{(n_1 n_2 - \mathbf{n}_{v1} \cdot \mathbf{n}_{v2})}{(1 - n_3)} + \\ & \frac{n_2^3/3 - n_2 \mathbf{n}_{v2}^2 + 3(\mathbf{n}_{v2} \mathbf{n}_{m2} \mathbf{n}_{v2} - 3 \det \mathbf{n}_{m2})/2}{8\pi(1 - n_3)}. \end{aligned} \quad (3.20)$$

The contributions involving \mathbf{n}_{m2} are small and will be neglected henceforth. They were given here for completeness.

The last input are the tensors $\boldsymbol{\omega}_{11}(\mathbf{r} - \mathbf{r}')$ and $\boldsymbol{\omega}_{12}(\mathbf{r} - \mathbf{r}')$ that account for the hydrodynamic interactions between a pair of spheres. We approximate $D_0\boldsymbol{\omega}_{12}(\mathbf{r} - \mathbf{r}')$ by the well-known Rotne-Prager expression [58], and it is given in Eq. (2.7) in chapter 2 and neglect $\boldsymbol{\omega}_{11}(\mathbf{r} - \mathbf{r}')$, whose leading term is $O((\sigma/r)^4)$. On this level of approximation, we incorporate all solvent mediated interactions up to $O((\sigma/r)^3)$, neglected is $O((\sigma/r)^4)$.

The partial differential equation governing the time evolution of $\rho(r, t)$, Eq. (3.11), is solved numerically employing a finite difference approximation with a fixed time step $\Delta t_D = 10^{-5}\tau_B$. We avoid the numerically demanding solution of Eq. (3.12) which would involve an iterative scheme to calculate the two-body density at every time step. Instead, we approximate the two-body density by $\rho^{(2)}(\mathbf{r}, \mathbf{r}', t) = \rho(r, t)\rho(r', t)g(|\mathbf{r} - \mathbf{r}'|)$, where $g(|\mathbf{r} - \mathbf{r}'|)$ is the pair correlation function for a homogeneous system, that has been evaluated from an analytic expression, which is based on the Percus-Yevick equation, given in [115]. Thereby, at each time step the pair correlation is calculated at the average density of the system $\bar{\rho}(t) = 1/R_{\max} \int_0^{R_{\max}} dr \rho(r, t)$, where R_{\max} is the distance from the origin for which the density vanishes: $\rho(r \geq R_{\max}, t) = 0$.

The results are checked against Brownian dynamics simulations performed on the same level of accuracy of the diffusion tensor. Additionally, the densities are compared to those obtained by standard DDFT where hydrodynamic interactions are ignored. The Brownian dynamics simulation technique for hard spheres differs from the standard one presented by Ermak [56] (see also previous chapter 2) where in a time step Δt all particles are displaced simultaneously. In the latter method forbidden overlap configurations would occur. To avoid those, the method presented by Cichocki and Hinsen [116] resembles that of a Monte-Carlo simulation. In each time step $\Delta t/N$ only one particle is displaced according to Eq. (2.4). If an overlap occurs, the particle is restored to its previous position and the time step is not counted. Unfortunately, this scheme is only valid for Brownian dynamics simulations in which hydrodynamic interactions are neglected. For hydrodynamic interactions on the Rotne-Prager level no similar scheme is available. Foss and Brady [117] presented a simulation method for hard spheres which is based on the Stokesian dynamics [61]. Their code crucially needs lubrication forces to avoid particle overlaps and is thus not appropriate here, since lubrication is neglected in the DDFT results. Therefore, for the case of hydrodynamic interactions included, we approximate the hard interaction by a soft one:

$$\frac{v_2(r_{ij})}{k_B T} = \begin{cases} \left[\left(\frac{\sigma}{r_{ij}} \right)^{48} - \left(\frac{\sigma}{r_{ij}} \right)^{24} + \frac{1}{4} \right] & \text{if } r_{ij} \leq 2^{1/24}\sigma \\ 0 & \text{else} \end{cases} . \quad (3.21)$$

The simulation algorithm is then the same as presented in chapter 2. In

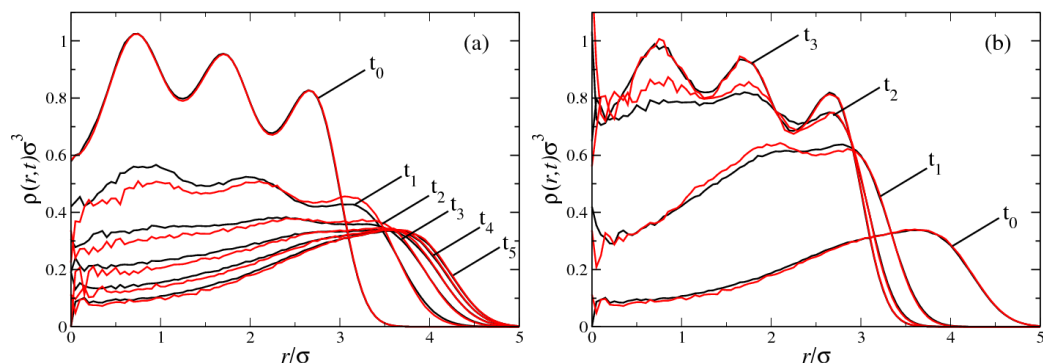


Figure 3.1: Hard-sphere (black curves) and soft-sphere (red curves) BD simulation results for the time-dependent density profile. Hydrodynamic interactions are in both cases neglected. The profiles correspond to the following time sequence: $t_0 = 0.0$, $t_1 = 0.1\tau_B$, $t_2 = 0.2\tau_B$, $t_3 = 0.3\tau_B$, $t_4 = 0.4\tau_B$, and $t_5 = 0.5\tau_B$ in (a) and $t_0 = 0.5\tau_B$, $t_1 = 0.6\tau_B$, $t_2 = 0.7\tau_B$, $t_3 = 1.0\tau_B$ in (b).

all simulations we chose $\Delta t = 10^{-4}$. In order to obtain the time-dependent density $\rho(r, t)$ we perform a large number $N_{\text{run}} = 5000$ of independent runs with different initial configurations sampled from a situation with a static external potential, i.e., Eq. (3.14) at $t = 0$.

For hydrodynamic interactions neglected we are in the position to compare the resulting density profiles for the hard- and the soft-core interaction, see Fig. 3.1. Some deviations are observed (profiles for the soft-core interaction evolve faster and have slightly less structure). However, we use the soft-core results as reference results for hydrodynamic interactions included. For future work, a simulation scheme that is capable of simulating the true hard-sphere interaction should be developed.

3.4 Results

In this section, we present the results obtained by DDFT and Brownian dynamics simulation for the setups introduced in the preceding section. Henceforth, the case of hydrodynamic interactions included will be labeled (A), and the case of hydrodynamic interactions ignored (B), respectively. The associated profiles for $\rho(r, t)$ are shown in Fig. 3.2 for the first half-period in which the cavity is unstable and in Fig. 3.3 for the stable complement, respectively. In (A) full relaxation to equilibrium is hindered by the periodic switching of the external potential and the system rather reaches a *steady-*

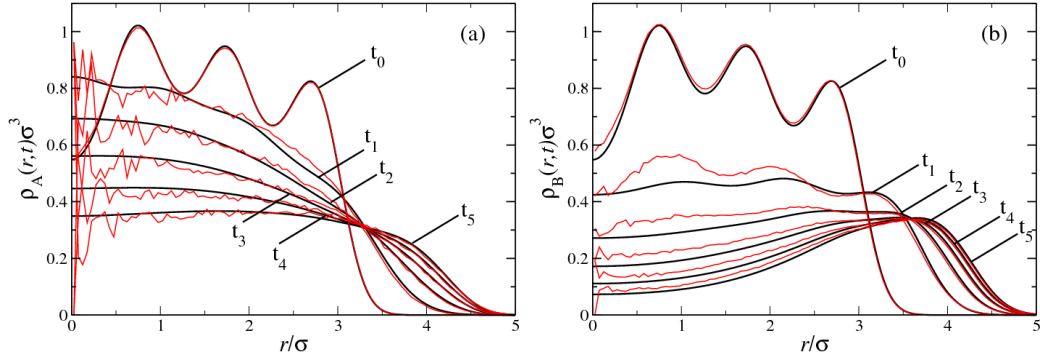


Figure 3.2: DDFT (black curves) and BD (noisy red curves) results for the time-dependent density profile with hydrodynamic interactions taken into account (a) and without hydrodynamic interactions (b). The profiles correspond to the following time sequence: $t_0 = 0.0$, $t_1 = 0.1\tau_B$, $t_2 = 0.2\tau_B$, $t_3 = 0.3\tau_B$, $t_4 = 0.4\tau_B$, and $t_5 = 0.5\tau_B$.

state, i.e., a periodically repeating density profile $\rho(r, t) = \rho(r, t + T)$. The steady-state profiles for (A) are depicted in Fig. 3.4. In (B) on the other hand, the system relaxes to equilibrium within each period. Therefore, their steady-state profiles are identical to those in the initial period and not shown again. The initial curves in Fig. 3.2 are the same in both cases, namely the equilibrium profiles $\rho_0(r)$ for $t = 0$, i.e., when the external confining potential is stable. One clearly observes a layering in the initial curve with three correlation peaks in the density profile. In the dynamic development of the

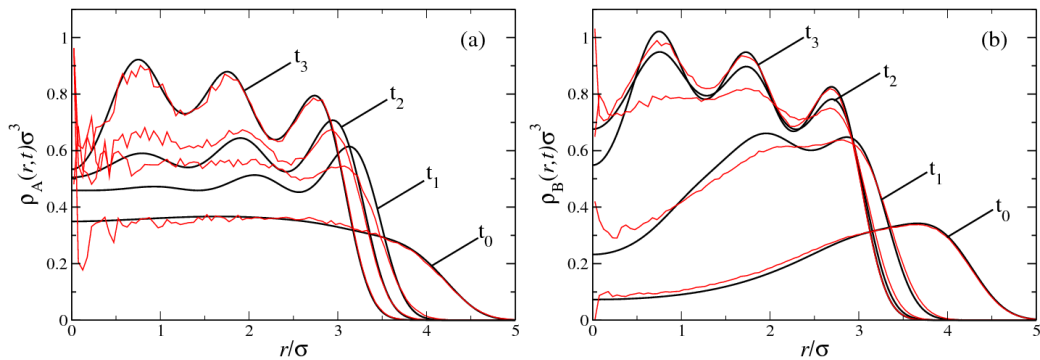


Figure 3.3: Same as Fig. 3.2 but for the time sequence: $t_0 = 0.5\tau_B$, $t_1 = 0.6\tau_B$, $t_2 = 0.7\tau_B$, and $t_3 = 1.0\tau_B$.

density, there are some obvious results that can already be discerned by vi-

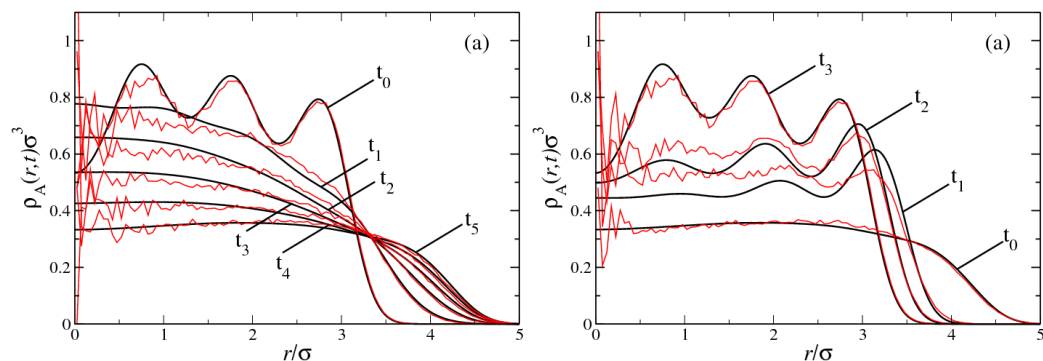


Figure 3.4: DDFT (black curves) and BD (noisy red curves) results for the time-dependent steady-state density profile with hydrodynamic interactions taken into account for the expanding and compressing half-periods (a) and (b), respectively. $t_0 = 2T + 0.0$, $t_1 = 2T + 0.1\tau_B$, $t_2 = 2T + 0.2\tau_B$, $t_3 = 2T + 0.3\tau_B$, $t_4 = 2T + 0.4\tau_B$, and $t_5 = 2T + 0.5\tau_B$ in (a) and $t_0 = 2T + 0.5$, $t_1 = 2T + 0.6\tau_B$, $t_2 = 2T + 0.7\tau_B$, $t_3 = 2T + 1.0\tau_B$ in (b).

sual inspection: The curves obtained by DDFT are in good agreement with the simulation results for the initial unstable half-period (Fig. 3.2), while there are strong deviations in the stable half-period (Fig. 3.3), in both (A) and (B). The latter can be understood from the fact that the system is driven with a strong external force and is therefore “far from equilibrium”. Then the fast driving process might generate additional dynamic correlations. In such a situation the underlying assumption in the derivation of the DDFT is rather inappropriate. This is supported from the finding that the agreement in (B) is “worse” than in (A). The dynamics in the system involving hydrodynamic interactions are considerably slowed by the coupling of the spheres through the long ranged solvent mediated interactions and therefore the net-force on each particle is smaller than in (B). Then, the assumption in the DDFT seems to work better. However, the qualitative trends are recovered correctly.

Since the first time step of the time evolution of the density with hydrodynamic interactions is given by [see Eq. (3.11)]: $\rho_A(r, \Delta t_D) = \rho_B(r, \Delta t_D) + \Delta\rho(r)\Delta t_D$, where ρ_A is the density profile of situation (A) and ρ_B of (B), respectively, the significant retardation of (A) compared to (B) can be inferred more quantitatively from the difference in the initial time evolution between the case (A) and (B), i.e., $\Delta\rho(r) = (\rho_A(r, \Delta t_D) - \rho_B(r, \Delta t_D))/\Delta t_D$, presented in Fig. 3.5. We accompany the figure with the initial time evolution of the density when hydrodynamic interactions are neglected: $\Delta\rho_B(r) =$

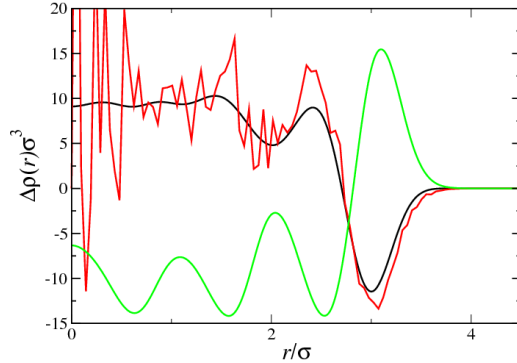


Figure 3.5: Difference in the initial time evolution of the density profiles $\Delta\rho(r)$ from DDFT (black curve) and simulation (noisy red curve). Additionally, the DDFT result for $\Delta\rho_B(r) = (\rho_B(r, \Delta t_D) - \rho_0(r))/\Delta t_D$ (green curve) is shown.

$(\rho_B(r, \Delta t_D) - \rho_0(r))/\Delta t_D$. The figure clearly reveals that the part originating from the hydrodynamic interactions is acting in the opposite direction and is of the same order of magnitude as the part without hydrodynamic interactions. Here, the DDFT reproduces the simulation results.

A further qualitative difference between (A) and (B) is that during the unstable half-period, where particles leak in to the initially depleted area, Fig. 3.2(a) reveals that the density in the center of the system first increases and then gradually decreases. In (B) on the other hand, Fig. 3.2(b), the density behaves rather the way one would expect: The profiles decrease gradually and leave behind a depleted part in the center. During the confining half-period, the behavior is opposed to the former. Here, in (B) initially, mainly the outer part of the cavity experiences an increase in the density while the center remains depleted. Only in a later stage of the time evolution material flows to the center. This is again the behavior one would expect, since the forces are the stronger the larger the distance from the origin. In (A) on the other hand, the center of the system is affected immediately due to the hydrodynamic coupling of the particles.

In order to quantify better the asymmetry of the time evolution of (A) and (B), we consider the second moment of the density, $m_2(t)$, defined through

$$m_2(t) = \int d\mathbf{r} r^2 \rho(r, t). \quad (3.22)$$

This quantity is a measure of the spread of $\rho(r, t)$ around the center of the external field. Its time evolution is depicted in Fig. 3.6. Obviously, the time

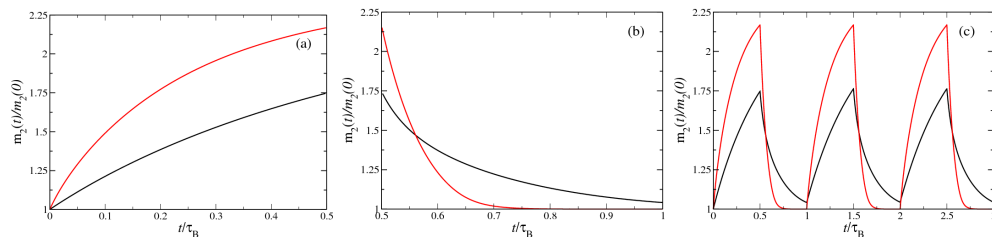


Figure 3.6: The second moment of the radial DDFT density profiles, $m_2(t)$ for hydrodynamic interactions taken into account (black curves) and neglected (red curves), respectively. Results for the time evolution of $m_2(t)$ for initial unstable half-period (A), the initial stable half-period (b), and for the first three periods (C) are shown.

evolution of $m_2(t)$ for (A) and (B) are different and it also supports our earlier finding that the dynamics of the system with hydrodynamic interactions are considerably slowed compared to (B). System (B) is already in its steady-state within the first period and correspondingly the second moment is virtually the same for the next periods. System (A) on the other hand, needs two periods to be in the steady-state. Furthermore, Fig. 3.6 reveals that the stable and the unstable half-period are asymmetric and not each other's “time reverse”. The saw tooth-like shape of $m_2(t)$ indicates that the confining half-period evolves much faster than the unstable one.

We checked whether the time evolution of $m_2(t)$ can be fitted to a single exponential during the stable or the unstable half-period, respectively. The motivation to do so, is that the time evolution of a single isolated particle would behave like this, since the driving force is proportional to r . We find that non of the curves can be fitted reasonably to a single exponential and conclude that the dynamical evolution of the densities is non-trivial.

Finally, to scrutinize the influence of the strength of the external force on the accuracy of the adiabatic approximation, we also studied a similar system with the following external potential:

$$V_{\text{ext}}(r) = V_0 \left(\frac{r}{R_0} \right)^2 - \Theta(\sin(2\pi t/T)) V_D \left(\frac{r}{R_D} \right)^2, \quad (3.23)$$

with $V_0 = 10k_B T$, $V_D = 5k_B T$, $R_0 = R_D = 2\sigma$, $T = 0.5\tau_B$, and $N = 30$. In this setup the forces acting on the particles are moderate compared to the previous one. The resulting curves for the first two half-periods are depicted in Fig. 3.7 and Fig. 3.8. Again, we show both cases: hydrodynamic interactions included (A) and neglected (B). Obviously, the DDFT results are in good agreement with the simulation data in situation (A) and (B)

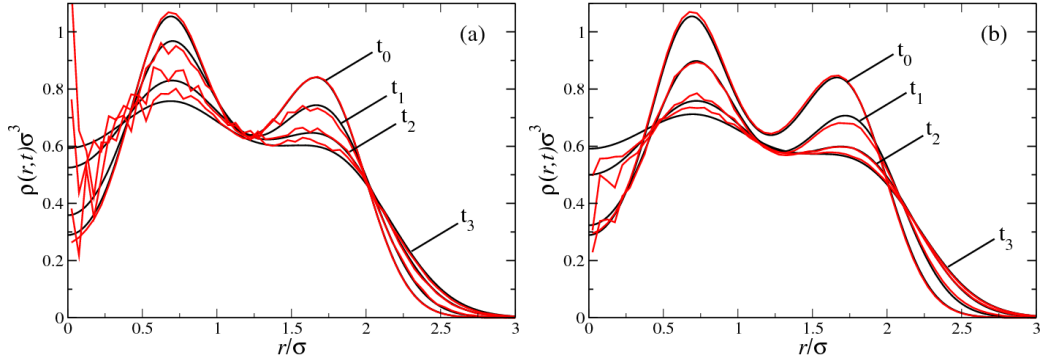


Figure 3.7: DDFT (black curves) and BD (noisy red curves) results for the time-dependent density profile with hydrodynamic interactions taken into account (a) and without hydrodynamic interactions (b) for the external potential (3.23). The profiles correspond to the following time sequence: $t_0 = 0.0$, $t_1 = 0.05\tau_B$, $t_2 = 0.15\tau_B$, and $t_3 = 0.25\tau_B$.

for the stable half-period as well as for the unstable one. This supports our conclusion that the discrepancies in the previous setup stem from the strong forces. On the other hand, we find smaller differences in the dynamical evolution of the densities in (A) and (B) compared to the previous setup. Yet, we observe the same trend, namely a retardation in the dynamics in system (A) compared to (B).

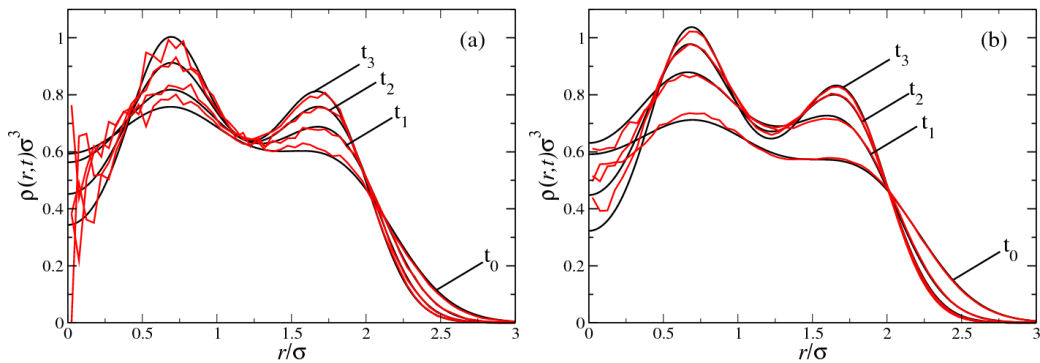


Figure 3.8: Same as Fig. 3.7 but for the time sequence: $t_0 = 0.25\tau_B$, $t_1 = 0.3\tau_B$, $t_2 = 0.4\tau_B$, and $t_3 = 0.5\tau_B$.

3.5 Conclusions

In this chapter, we have presented a DDFT formalism with hydrodynamic interactions incorporated on a two-particle level. As a demonstration of the theory we have studied a hard-sphere system confined in an optical trap which switches periodically from a stable to an unstable confining potential. The theory has been supplemented by an accurate equilibrium free energy functional, namely Rosenfeld's FMT functional. We have found good agreement for the dynamic development of the density profile in the unstable half-period while deviations from simulation results have been observed during the stable half-period. The latter was explained by the strong driving force acting on the spheres such that the system is far from equilibrium. In this situation the assumption underlying DDFT seems inappropriate. By comparing the results to those obtained from conventional DDFT, where hydrodynamic interactions are ignored, we find significant differences and the time evolution is considerably slowed by hydrodynamic interactions.

The presented formalism provides a theory that can be applied to arbitrary time-dependent external potentials and systems, provided the applied external forces are moderate and an accurate equilibrium free energy functional is known. It would be interesting to study sedimentation or, in connection with the previous section, lane formation with DDFT. It would be further challenging to generalize the present formalism to many-body hydrodynamic interactions. A generalization of DDFT to anisotropic particles with orientational degrees of freedom without hydrodynamic interactions will be given in the next chapter 4.

Finally, Archer [109] has demonstrated how mode-coupling theory, which is capable of predicting glass transition, can be derived from a DDFT for atomic liquids with further approximations. It is tempting to use the above formalism to derive a mode-coupling theory including hydrodynamic interactions since it is anticipated that hydrodynamic interactions play an important role in the dynamics near the glass transition [118].

Chapter 4

Dynamical density functional theory for anisotropic colloidal particles

In this chapter, we present a joint work with H. H. Wensink. We generalize the formalism of dynamical density functional theory for translational Brownian dynamics to that of anisotropic colloidal particles which perform both translational and rotational Brownian motion. Using a mean-field approximation for the density functional and a Gaussian-segment model for the rod interaction, the dynamical density functional theory is then applied to a concentrated rod suspension in a confined slab geometry made by two parallel soft walls. The walls are either expanded or compressed and the relaxation behavior is investigated for an equilibrated starting configuration. We find distinctly different orientational ordering during expansion and compression. During expansion we observe preferential parallel ordering of the rods relative to the wall while during compression there is homeotropic ordering perpendicular to the wall. We find a nonexponential relaxation behavior in time. Furthermore, an external field which aligns the rods perpendicular to the walls is turned on or switched off and similar differences in the relaxational dynamics are found. Comparing the theoretical predictions to Brownian dynamics computer simulation data – by courtesy of H. H. Wensink –, we find good agreement.

4.1 Introduction

Nearly all activities in dynamical density functional theory, including the previous chapter 3, were focused on translational dynamics while the orien-

tational degrees of freedom were neglected. The latter are trivial for spherical particles but become highly relevant for asymmetric (e.g., rodlike) particles. At high densities, the translational degrees of freedom are nontrivially coupled to their rotational counterparts.

In this chapter, we extend the formalism of dynamical density functional theory to both translational and rotational degrees of motion by considering the Brownian motion of anisotropic colloidal particles. With similar approximations used for the translational case [34], we derive the dynamical equation for the time-dependent density field $\rho(\mathbf{r}, \hat{\omega}, t)$ which depends both on the position \mathbf{r} and orientation $\hat{\omega}$, where $\hat{\omega}$ is a unit vector. It is shown that this theory becomes equivalent to the approach of Dhont, Briels and co-workers [119, 120] at low-density where a virial approximation for the density functional is appropriate. The theory, however, provides a more general framework for dynamics and nonequilibrium phenomena at higher densities as well. We then test the theory against Brownian dynamics computer simulation for a soft-core rod-segment model. This model is the rodlike analog to spherical polymer models [121, 122] and therefore describes bottle-brush polymers with a stiff backbone [123–125]. We use a mean-field-type approximation for the density functional and apply it to a situation of strong confinement between two soft walls. Two situations are studied. First the confined system is compressed and relaxed by compressing and expanding the walls. In a second setup, an additional external aligning field is turned on and switched off. We find a nontrivial relaxation behavior which is non-exponential in time. Expansion and compression proceed via different paths as a function of time. In particular, distinctly different orientational ordering during expansion and compression is observed. During expansion, rods orient preferentially parallel to the wall while during compression there is homeotropic ordering perpendicular to the wall. Similar conclusions are found for the aligning field. In general, good agreement between DDFT and Brownian dynamics simulation is found.

This chapter is organized as follows. In Sec. 4.2 we derive the generalized dynamical density functional theory which includes rotational Brownian motion. Sec. 4.3 and 4.4 will be devoted to describing the rod model, the associated free energy functional and the dynamical processes, respectively. In Sec. 4.5 the predictions of our DDFT will be compared with simulation results and notable effects will be discussed. Finally, some conclusions will be formulated in Sec. 4.6.

4.2 Equation of motion for the one-body density

In this section we will derive an expression for the time evolution of the one-body density, $\rho(\mathbf{r}, \hat{\omega}, t)$, for anisotropic Brownian particles with a three-dimensional spatial coordinate \mathbf{r} and orientation unit vector $\hat{\omega}$. In doing so, we generalize the derivation by Archer and Evans [34] to orientational degrees of freedom.

We start from the full probability density distribution $P(\mathbf{r}^N, \hat{\omega}^N, t)$ to find N anisotropic Brownian particles at positions $\mathbf{r}^N = (\mathbf{r}_1, \dots, \mathbf{r}_N)$ and orientations $\hat{\omega}^N = (\hat{\omega}_1, \dots, \hat{\omega}_N)$. According to Ref. [34], the n -body density is given by the following integral of the probability density distribution $P(\mathbf{r}^N, \hat{\omega}^N, t)$

$$\rho^n(\mathbf{r}^n, \hat{\omega}^n, t) = \frac{N!}{(N-n)!} \int d\mathbf{r}_{n+1} \dots \int d\mathbf{r}_N \oint d\hat{\omega}_{n+1} \dots \oint d\hat{\omega}_N P(\mathbf{r}^N, \hat{\omega}^N, t) \quad (4.1)$$

where the integral of the orientation is over the full unit sphere. For overdamped Brownian dynamics of the particles, the time evolution of $P(\mathbf{r}^N, \hat{\omega}^N, t)$ is given by the Smoluchowski equation [10]

$$\frac{\partial P(\mathbf{r}^N, \hat{\omega}^N, t)}{\partial t} = \hat{\mathcal{L}}_S P(\mathbf{r}^N, \hat{\omega}^N, t) \quad (4.2)$$

where the Smoluchowski operator is defined as

$$\hat{\mathcal{L}}_S = \sum_{i=1}^N \left\{ \nabla_{\mathbf{r}_i} \cdot \mathbf{D}(\hat{\omega}_i) \cdot [\nabla_{\mathbf{r}_i} + \beta \nabla_{\mathbf{r}_i} U(\mathbf{r}^N, \hat{\omega}^N, t)] + D_r \hat{\mathcal{R}}_i \cdot [\hat{\mathcal{R}}_i + \beta \hat{\mathcal{R}}_i U(\mathbf{r}^N, \hat{\omega}^N, t)] \right\}. \quad (4.3)$$

Here, hydrodynamic interactions are not taken into account, $\beta^{-1} = k_B T$ is the thermal energy of the system, $\nabla_{\mathbf{r}_i}$ is the gradient operator with respect to \mathbf{r}_i , and $\hat{\mathcal{R}}_i$ the rotation operator acting on the Cartesian coordinates of the orientation $\hat{\omega}_i$. The latter is given by

$$\hat{\mathcal{R}}_i = \hat{\omega}_i \times \nabla_{\hat{\omega}_i}. \quad (4.4)$$

Furthermore, D_r is the rotational diffusion coefficient and $\mathbf{D}(\hat{\omega}_i)$ the translational diffusion tensor. For uniaxial (cylindrical) anisotropic particles this tensor may be expressed as

$$\mathbf{D}(\hat{\omega}_i) = D_{\parallel} \hat{\omega}_i \hat{\omega}_i + D_{\perp} [\hat{\mathbf{I}} - \hat{\omega}_i \hat{\omega}_i], \quad (4.5)$$

in terms of the translational diffusion constant parallel (D_{\parallel}) and perpendicular (D_{\perp}) to the main particle axis $\hat{\omega}_i$, with $\hat{\mathbf{I}}$ the unit matrix, and $\hat{\omega}_i\hat{\omega}_i$ the dyadic product. Assuming pairwise additivity for the total potential energy of the system $U(\mathbf{r}^N, \hat{\omega}^N, t)$, we may write

$$U(\mathbf{r}^N, t) = \sum_{i=1}^N V_{\text{ext}}(\mathbf{r}_i, \hat{\omega}_i, t) + \frac{1}{2} \sum_{i=1}^N \sum_{j \neq i}^N v_2(\mathbf{r}_i, \mathbf{r}_j, \hat{\omega}_i, \hat{\omega}_j), \quad (4.6)$$

where $V_{\text{ext}}(\mathbf{r}, \hat{\omega}, t)$ is the one-body external potential acting on each particle and $v_2(\mathbf{r}, \mathbf{r}', \hat{\omega}, \hat{\omega}')$ the pair potential. Upon integrating Eq. (4.2) with $N \int d\mathbf{r}_2 \dots \int d\mathbf{r}_N \oint d\hat{\omega}_2 \dots \oint d\hat{\omega}_N$ one obtains

$$\begin{aligned} \frac{\partial \rho(\mathbf{r}, \hat{\omega}, t)}{\partial t} = & \\ & \nabla_{\mathbf{r}} \cdot \mathbf{D}(\hat{\omega}) \cdot \left[\nabla_{\mathbf{r}} \rho(\mathbf{r}, \hat{\omega}, t) + \beta \rho(\mathbf{r}, \hat{\omega}, t) \nabla_{\mathbf{r}} V_{\text{ext}}(\mathbf{r}, \hat{\omega}, t) - \beta \bar{\mathbf{F}}(\mathbf{r}, \hat{\omega}, t) \right] \\ & + D_r \hat{\mathcal{R}} \cdot \left[\hat{\mathcal{R}} \rho(\mathbf{r}, \hat{\omega}, t) + \beta \rho(\mathbf{r}, \hat{\omega}, t) \hat{\mathcal{R}} V_{\text{ext}}(\mathbf{r}, \hat{\omega}, t) - \beta \bar{\mathbf{T}}(\mathbf{r}, \hat{\omega}, t) \right], \quad (4.7) \end{aligned}$$

with $\bar{\mathbf{F}}(\mathbf{r}, \hat{\omega}, t)$ denoting the average force and $\bar{\mathbf{T}}(\mathbf{r}, \hat{\omega}, t)$ the average torque due to the interaction with other particles:

$$\begin{aligned} \bar{\mathbf{F}}(\mathbf{r}, \hat{\omega}, t) = & - \int d\mathbf{r}' \oint d\hat{\omega}' \rho^{(2)}(\mathbf{r}, \mathbf{r}', \hat{\omega}, \hat{\omega}', t) \nabla_{\mathbf{r}} v_2(\mathbf{r}, \mathbf{r}', \hat{\omega}, \hat{\omega}', t) \\ & \text{and} \\ \bar{\mathbf{T}}(\mathbf{r}, \hat{\omega}, t) = & - \int d\mathbf{r}' \oint d\hat{\omega}' \rho^{(2)}(\mathbf{r}, \mathbf{r}', \hat{\omega}, \hat{\omega}', t) \hat{\mathcal{R}} v_2(\mathbf{r}, \mathbf{r}', \hat{\omega}, \hat{\omega}', t). \quad (4.8) \end{aligned}$$

Note that for the steady-state ($\partial \rho / \partial t = 0$), Eq. (4.7) reduces to the first member of the Yvon-Born-Green (YBG) hierarchy molecular fluids [126].

The equation of motion (4.7) for the one-body density $\rho(\mathbf{r}, \hat{\omega}, t)$ is *exact* but still depends on the unknown time-dependent two-body density $\rho^{(2)}(\mathbf{r}, \mathbf{r}', \hat{\omega}, \hat{\omega}', t)$. Using Eq. (4.1), a similar equation of motion may be derived for $\rho^{(2)}(\mathbf{r}, \mathbf{r}', \hat{\omega}, \hat{\omega}', t)$ which will depend on the three-body density $\rho^{(3)}$ and so on. To make headway, a closure relation is needed to terminate the resulting hierarchy of coupled equations of motion. Making use of static DFT, this can be done at the second YBG level by recasting the average interaction force and torque, given by Eq. (4.8), into functionals of the nonequilibrium one-body density to construct a dynamical density functional theory.

In equilibrium, a generalized force balance equation can be proved [29, 127]

$$\nabla_{\mathbf{r}} \rho_0(\mathbf{r}, \hat{\omega}) + \beta \rho_0(\mathbf{r}, \hat{\omega}) \nabla_{\mathbf{r}} V_{\text{ext}}(\mathbf{r}, \hat{\omega}) = -\rho_0(\mathbf{r}, \hat{\omega}) \nabla_{\mathbf{r}} \left. \frac{\delta \mathcal{F}_{\text{exc}}[\rho]}{\delta \rho} \right|_{\rho=\rho_0(\mathbf{r}, \hat{\omega})} \quad (4.9)$$

where $\rho_0(\mathbf{r}, \hat{\omega})$ denotes the equilibrium one-particle density field corresponding to the prescribed external potential $V_{\text{ext}}(\mathbf{r}, \hat{\omega})$ and $\mathcal{F}_{\text{exc}}[\rho_0]$ is the excess free energy density functional in equilibrium. Likewise, a generalized torqued balance [127] reads in equilibrium as

$$\hat{\mathcal{R}}\rho_0(\mathbf{r}, \hat{\omega}) + \beta\rho_0(\mathbf{r}, \hat{\omega})\hat{\mathcal{R}}V_{\text{ext}}(\mathbf{r}, \hat{\omega}) = -\rho_0(\mathbf{r}, \hat{\omega})\hat{\mathcal{R}}\left.\frac{\delta\mathcal{F}_{\text{exc}}[\rho]}{\delta\rho}\right|_{\rho=\rho_0(\mathbf{r}, \hat{\omega})}. \quad (4.10)$$

A second set of balance conditions are the well-known YBG relations [cf. Eq. (4.7)] in equilibrium [126]. These are for the translational part

$$\begin{aligned} \nabla_{\mathbf{r}}\rho_0(\mathbf{r}, \hat{\omega}) + \beta\rho_0(\mathbf{r}, \hat{\omega})\nabla_{\mathbf{r}}V_{\text{ext}}(\mathbf{r}, \hat{\omega}) = \\ -\beta \int d\mathbf{r}' \oint d\hat{\omega}' \rho_0^{(2)}(\mathbf{r}, \mathbf{r}', \hat{\omega}, \hat{\omega}')\nabla_{\mathbf{r}}v_2(\mathbf{r}, \mathbf{r}', \hat{\omega}, \hat{\omega}') \end{aligned} \quad (4.11)$$

and for the rotational part

$$\begin{aligned} \hat{\mathcal{R}}\rho_0(\mathbf{r}, \hat{\omega}) + \beta\rho_0(\mathbf{r}, \hat{\omega})\hat{\mathcal{R}}V_{\text{ext}}(\mathbf{r}, \hat{\omega}) = \\ -\beta \int d\mathbf{r}' \oint d\hat{\omega}' \rho_0^{(2)}(\mathbf{r}, \mathbf{r}', \hat{\omega}, \hat{\omega}')\hat{\mathcal{R}}v_2(\mathbf{r}, \mathbf{r}', \hat{\omega}, \hat{\omega}') \end{aligned} \quad (4.12)$$

respectively. Consequently, the following two relations hold in equilibrium:

$$\rho_0(\mathbf{r}, \hat{\omega})\nabla_{\mathbf{r}}\frac{\delta\mathcal{F}_{\text{exc}}[\rho]}{\delta\rho_0(\mathbf{r}, \hat{\omega})} = \int d\mathbf{r}' \oint d\hat{\omega}' \rho_0^{(2)}(\mathbf{r}, \mathbf{r}', \hat{\omega}, \hat{\omega}')\nabla_{\mathbf{r}}v_2(\mathbf{r}, \mathbf{r}', \hat{\omega}, \hat{\omega}') \quad (4.13)$$

and

$$\rho_0(\mathbf{r}, \hat{\omega})\hat{\mathcal{R}}\frac{\delta\mathcal{F}_{\text{exc}}[\rho]}{\delta\rho_0(\mathbf{r}, \hat{\omega})} = \int d\mathbf{r}' \oint d\hat{\omega}' \rho_0^{(2)}(\mathbf{r}, \mathbf{r}', \hat{\omega}, \hat{\omega}')\hat{\mathcal{R}}v_2(\mathbf{r}, \mathbf{r}', \hat{\omega}, \hat{\omega}'). \quad (4.14)$$

The two right-hand sides of equations (4.13) and (4.14) occur in the dynamical (nonequilibrium) context as average force and torque in Eq. (4.7). The basic approximation now is to use this expression in the nonequilibrium situation. This may be called an adiabatic approximation since the underlying idea is to identify – for a fixed time t – the dynamical one-particle density profile $\rho(\mathbf{r}, \hat{\omega}, t)$ with an equilibrium density profile $\rho_0(\mathbf{r}, \hat{\omega})$ with a suitably prescribed external potential. Strictly speaking, the two latter quantities depend parametrically on time t . Hence nonequilibrium correlations are approximated by equilibrium correlations of a suitable equilibrium reference system that possesses the same one-particle density [31, 33].

Within this *adiabatic approximation*, we obtain our central dynamical density functional theory (DDFT) result:

$$\begin{aligned} \frac{\partial\rho(\mathbf{r}, \hat{\omega}, t)}{\partial t} = \nabla_{\mathbf{r}} \cdot \mathbf{D}(\hat{\omega}) \cdot \left[\rho(\mathbf{r}, \hat{\omega}, t)\nabla_{\mathbf{r}}\frac{\delta\mathcal{F}[\rho(\mathbf{r}, \hat{\omega}, t)]}{\delta\rho(\mathbf{r}, \hat{\omega}, t)} \right] \\ + D_r\hat{\mathcal{R}} \cdot \left[\rho(\mathbf{r}, \hat{\omega}, t)\hat{\mathcal{R}}\frac{\delta\mathcal{F}[\rho(\mathbf{r}, \hat{\omega}, t)]}{\delta\rho(\mathbf{r}, \hat{\omega}, t)} \right], \end{aligned} \quad (4.15)$$

in terms of the total *equilibrium* Helmholtz free energy functional

$$\mathcal{F}[\rho_0] = \mathcal{F}_{\text{id}}[\rho_0] + \mathcal{F}_{\text{exc}}[\rho_0] + \int d\mathbf{r} \oint d\hat{\omega} \rho_0(\mathbf{r}, \hat{\omega}) V_{\text{ext}}(\mathbf{r}, \hat{\omega}, t) \quad (4.16)$$

where the ideal contribution reads

$$\mathcal{F}_{\text{id}}[\rho_0] = k_{\text{B}}T \int d\mathbf{r} \oint d\hat{\omega} \rho_0(\mathbf{r}, \hat{\omega}) [\ln \mathcal{V}\rho_0(\mathbf{r}, \hat{\omega}) - 1], \quad (4.17)$$

with \mathcal{V} the thermal volume of the anisotropic particle.

We finish this section with some remarks: First of all, the DDFT equation for spherical particles is recovered when the density is independent of orientation. In this case, the adiabatic approximation has been shown to hold even for strong inhomogeneities and strong time dependencies and turned out to give remarkably good agreement with results from Brownian dynamics computer simulations [34, 36–40, 108, 110, 128, 129]. Second, we emphasize that the above equation reproduces the approach proposed by Dhont and Briels [119, 120] for thin hard rods if $\mathcal{F}_{\text{exc}}[\rho_0]$ is represented by the Onsager functional [8, 130]. Third, a similar dynamical density functional theory approach was proposed by Chandra and Bagchi [131, 132] on a phenomenological basis. In the latter work, the explicit coupling between orientational and translational diffusion was neglected.

4.3 Model and free energy functional

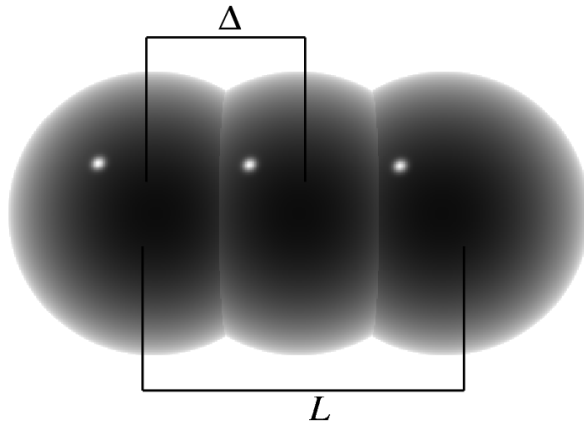


Figure 4.1: Gaussian segment model of $N_S = 3$ and segment spacing Δ .

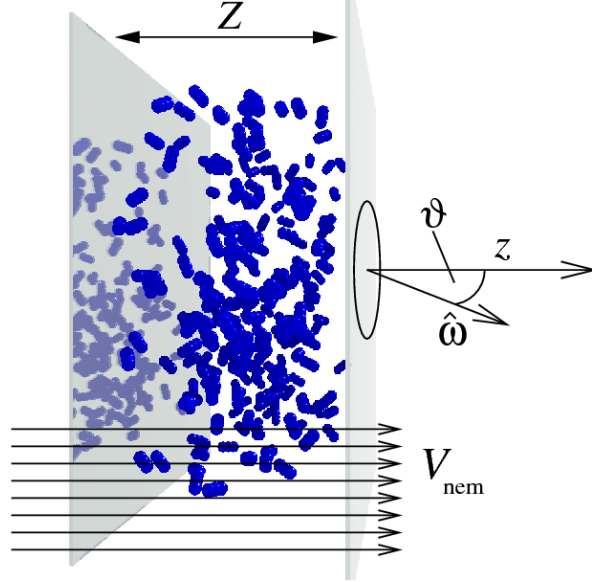


Figure 4.2: Schematic sketch of the system setup. The Gaussian rods are confined in a slab geometry that consists of two soft walls and an orienting field. V_{nem} is applied perpendicular to the walls. The relevant coordinates of the system are the spatial coordinate z normal to the wall and the angle ϑ between the rod and the wall normal.

In this chapter, we consider systems of soft rods of length L , each composed of N_S segments of *ultrasoft* spheres¹; see Fig. 4.1. The distance between two consecutive segments on the rod is $\Delta = L/(N_S - 1)$. The interaction potential between two segments of different rods is supposed to be a Gaussian. The total rod-rod interaction potential is then given by

$$v_2(\mathbf{r}_i, \mathbf{r}_j, \hat{\omega}_i, \hat{\omega}_j) = \epsilon \sum_{\alpha=-K}^K \sum_{\beta=-K}^K \exp\left(-\frac{|\mathbf{r}_{\alpha\beta}|^2}{\sigma^2}\right), \quad (4.18)$$

where $K = (N_S - 1)/2$ and $\mathbf{r}_{\alpha\beta} = (\mathbf{r}_i + \alpha\Delta\hat{\omega}_i) - (\mathbf{r}_j + \beta\Delta\hat{\omega}_j)$ the distance between segment α on rod i and β on rod j ($i \neq j$). Furthermore, σ is the range of the Gaussian potential which sets the unit length, and $\epsilon = k_B T$ provides the unit of energy for the system. In all cases, we consider slightly anisotropic rods with $N_S = 3$ and $L \equiv \sigma$.

The Gaussian segment model can be considered as a simplified model for the effective interaction between so-called *bottlebrush* polymers with a short,

¹Ellipsoidal Gaussian particles were recently studied in S. Prestipino and F. Saija, J. Chem. Phys. **126**, 194902 (2007)

stiff backbone [123–125]. For ultrasoft particles at high densities, a very accurate and simple functional $\mathcal{F}_{\text{exc}}[\rho]$ is available, namely the *mean-field* or *random-phase* approximation:

$$\mathcal{F}_{\text{exc}}[\rho] = \frac{1}{2} \int d\mathbf{r} \int d\mathbf{r}' \oint d\hat{\omega} \oint d\hat{\omega}' \rho(\mathbf{r}, \hat{\omega}) v_2(\mathbf{r}, \mathbf{r}', \hat{\omega}, \hat{\omega}') \rho(\mathbf{r}', \hat{\omega}'). \quad (4.19)$$

which was demonstrated to become exact for bounded potentials at asymptotically high densities [38, 106, 107]. The accuracy of the static mean-field DFT for soft rods enables us to scrutinize the validity of the adiabatic approximation for the dynamics of systems with coupled translational and rotational degrees of freedom.

An important limitation of our model is that, within the mean-field approximation, the rotational diffusion becomes ideal for homogeneous systems. This can be easily inferred from the excess functional Eq. (4.19) using the rod pair potential Eq. (4.18). Identifying $\rho(\mathbf{r}, \hat{\omega}) = \rho$ and carrying out the spatial integration over the Gaussian potential leads to a constant, independent of the orientation. This result, which in fact holds for *any* bounded segment-segment potential, implies that in homogeneous systems all rotational correlations are absent and that the system cannot form a stable nematic phase. Although this effect may seem unphysical, it is in fact reproduced by Brownian dynamics simulations of the segment model provided that the density is sufficiently high [133]. Therefore, in order to avoid the rotational diffusion being trivial we will only consider inhomogeneous systems throughout this paper. This is done by confining the fluid in a slab geometry consisting of two soft walls, see Fig. 4.2, so that a nonuniform density distribution is generated. The soft walls are supposed to model an optical trap such that only the colloidal particles are affected by the field and the solvent remains quiescent. For the external wall potential we choose the following form:

$$V_{\text{wall}}(z, t) = V_0(z/Z(t))^{10}. \quad (4.20)$$

Here, $V_0 = 10k_{\text{B}}T$ is the amplitude of the potential, and $Z(t)$ the potential range that will be changed in time; see Sec. 4.4. In this setup, the instantaneous density profile $\rho(z, \vartheta, t)$ depends on only one spatial coordinate z (normal to the wall), an angular one ϑ (the angle between the rod and the wall normal), and time t . A similar setup for the statics of hard ellipsoids between hard walls was studied by Chrzanowska *et al.* [134].

4.4 Dynamic processes

We intend to study two different setups. First, the system is compressed and expanded by changing the wall separation $Z(t)$. For the compression case,

the wall separation is reduced linearly in time, so that

$$Z(t) = \begin{cases} 2\sigma & \text{if } t < 0 \\ 2\sigma - ct & \text{if } 0 \leq t \leq \tau_B \\ \sigma & \text{if } t > \tau_B \end{cases} \quad (4.21)$$

with the velocity of the wall $c = \sigma/\tau_B$. τ_B denotes the Brownian timescale and will be specified later. The reverse direction is implemented for the expansion case. Additionally, we investigate the expansion process for an instantaneous extension of the wall separation. We do not look at the inverse problem: The instantaneous compression.

In a second setup, we instantaneously switch on an external orienting field represented by

$$V_{\text{nem}}(\vartheta) = -\Phi_0 \cos^2 \vartheta, \quad (4.22)$$

where the strength of the potential is $\Phi_0 = 10k_B T$ and ϑ is the angle between the wall normal and the orientation of the rods: $\cos \vartheta = \hat{z} \cdot \hat{\omega}$. This field generates strong homeotropic nematic ordering with a director parallel to the wall normal. All setups are summarized in Table 4.1.

In each system the initial density is the equilibrium density $\rho_0(z, \vartheta, t_0)$ of the respective system and we follow the time evolution of $\rho(z, \vartheta, t)$ to the new equilibrium state. Note that in the first scenario the external field primarily couples to the translational degree of freedom, whereas in the second one the orienting field acts only on the rod orientations. Both cases will provide insight into the intricate interplay between the translational and orientational degrees of freedom during the dynamic processes.

As a final input for the dynamics, we need to specify the diffusion constants D_\perp , D_\parallel , and D_r . For these, we take the results for hard ellipsoids of variable aspect ratio p reported by Tirado and co-workers [135]:

$$\begin{aligned} D_\perp &= \frac{D_0}{4\pi} (\ln p + 0.839 + 0.185/p + 0.233/p^2), \\ D_\parallel &= \frac{D_0}{2\pi} (\ln p - 0.207 + 0.980/p - 0.133/p^2), \\ D_r &= \frac{3D_0}{\pi L^2} (\ln p - 0.662 + 0.917/p - 0.050/p^2), \end{aligned} \quad (4.23)$$

where D_0 sets the unit of time via $\tau_B = \sigma^2/D_0$. In all cases, the hydrodynamic aspect-ratio of the rods was fixed at $p = 5$. To justify the use of the mean-field functional, we fix the overall system number density to $\rho_0 \sigma^3 = 1$, which is close to the overlap concentration of the rods.

Benchmark data to test our DDFT results were obtained by Brownian dynamics (BD) simulations of the segment model introduced in Sec. 4.3. The simulation method is based on a standard finite-difference integration of the overdamped Langevin equations for N Brownian rods according to the

| Setups | | $V_{\text{ext}}(\mathbf{r}, \omega, t)$ |
|--------|-----------------------------------|---|
| A | Slow compression | $V_0 \left(\frac{z}{Z(t)} \right)^{10}, Z(t) = \begin{cases} 2\sigma & \text{if } t < 0 \\ 2\sigma - ct & \text{if } 0 \leq t \leq \tau_B \\ \sigma & \text{if } t > \tau_B \end{cases}$ |
| B | Slow expansion | $V_0 \left(\frac{z}{Z(t)} \right)^{10}, Z(t) = \begin{cases} \sigma & \text{if } t < 0 \\ \sigma + ct & \text{if } 0 \leq t \leq \tau_B \\ 2\sigma & \text{if } t > \tau_B \end{cases}$ |
| C | Instantaneous expansion | $V_0 \left(\frac{z}{Z(t)} \right)^{10}, Z(t) = \begin{cases} \sigma & \text{if } t < 0 \\ 2\sigma & \text{if } t \geq 0 \end{cases}$ |
| D | Relaxation from initial alignment | $V_0 \left(\frac{z}{2\sigma} \right)^{10} - \Phi_0 \cos^2 \vartheta \Theta(-t)$ |
| E | Evolution toward alignment | $V_0 \left(\frac{z}{2\sigma} \right)^{10} - \Phi_0 \cos^2 \vartheta \Theta(t)$ |

Table 4.1: All setups investigated in this chapter which are characterized by different time-dependent external potentials and labeled by the letters A–E. In A, B, and C a slab confinement of two soft walls is modeled with time varying wall separation $Z(t)$ *compressing or relaxing the system*. z is the coordinate perpendicular to the walls, $V_0 = 10k_B T$ and $c = \sigma/\tau_B$. In D and E, in addition to a fixed slab geometry, a nematic ordering field is either switched off D or on E. Here, ϑ is the angle between the wall normal and the orientation of the rods: $\cos \vartheta = \hat{z} \cdot \hat{\omega}$, and $\Phi_0 = 10k_B T$. The Heaviside step-function is defined by: $\Theta(x) = 1$ if $x \geq 0$ and 0 if $x < 0$.

scheme of Ermak [56, 136]. We simulated $N = 100$ rods each with $N_S = 3$ segments in a slab geometry with periodic boundary conditions in the x and y directions. In all simulations, the time step was fixed at $0.001\tau_B$. Instantaneous density profiles were measured by averaging over 1000 consecutive dynamical processes each starting from a different initial equilibrium configuration. Each process was followed for the duration of about $15 - 20\tau_B$. To check for finite-size effects, additional simulations were carried out for $N = 500$ rods yielding virtually identical results in all setups.

4.5 Results

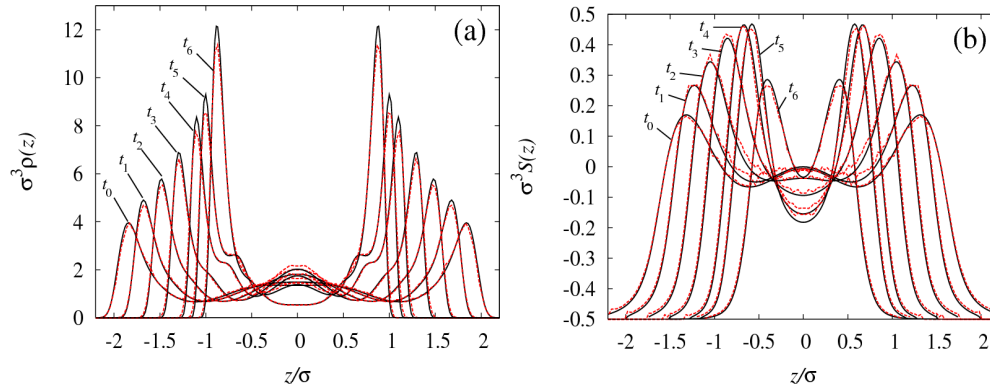


Figure 4.3: DDFT (solid black curves) and BD (dashed red curves) results for (a) the time-dependent density profile $\rho(z, t)$ and order parameter (b) $S(z, t)$ for the slow compression; see A in Table 4.1. The profiles correspond to the following time sequence: $t_0 = 0.0$, $t_1 = 0.2\tau_B$, $t_2 = 0.4\tau_B$, $t_3 = 0.6\tau_B$, $t_4 = 0.8\tau_B$, $t_5 = 0.9\tau_B$, and $t_6 = 15.0\tau_B$. At t_6 the system has virtually relaxed to equilibrium.

In this section, we present the results obtained by DDFT and Brownian dynamics simulation for the setups introduced in the preceding section. For each situation we show the time evolution of the density profile

$$\rho(z, t) = \int d(\cos \vartheta) \rho(z, \vartheta, t) \quad (4.24)$$

and of the local nematic order parameter

$$S(z, t) = \frac{1}{\rho(z, t)} \int d(\cos \vartheta) \left[\frac{3}{2} \cos^2 \vartheta - \frac{1}{2} \right] \rho(z, \vartheta, t) \quad (4.25)$$

for a sequence of times. The nematic order parameter gives insight into the preferred direction of the rods. It is unity if the rods are perfectly oriented perpendicular to the wall and $S = -0.5$ if the rods are oriented parallel to the wall.

4.5.1 Compression and expansion

First we examine the compression and expansion setups A, B, and C in Table 4.1. The associated profiles are shown in Figs. 4.3-4.5. From all figures it can be seen that the theory correctly reproduces the time evolution of the density and nematic order parameter profiles. Looking first at the evolution of the nematic order parameter $S(z, t)$ we find a qualitative difference between the slow compression and expansion processes. Upon compression, the rods show enhanced *homeotropic* ordering (perpendicular to the wall), whereas the expansion process seems to be associated with pronounced *planar* ordering (parallel to the wall).

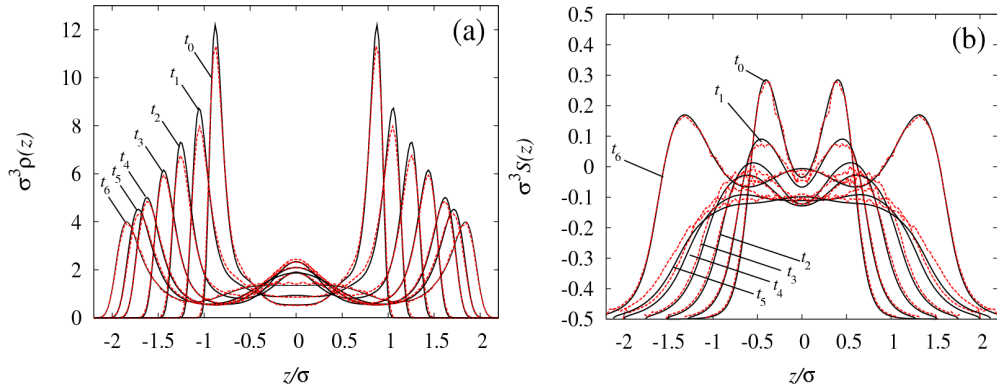


Figure 4.4: DDFT (solid black curves) and BD (dashed red curves) results for (a) the time-dependent density profile and (b) order parameter for the inverse case to Fig. 4.3, the slow expansion; see B in Table 4.1. The profiles correspond to the following time sequence: $t_0 = 0.0$, $t_1 = 0.2\tau_B$, $t_2 = 0.4\tau_B$, $t_3 = 0.6\tau_B$, $t_4 = 0.8\tau_B$, $t_5 = 0.9\tau_B$, and $t_6 = 15.0\tau_B$. At t_6 the system has virtually relaxed to equilibrium and the curves coincide with the initial ones, t_0 , in Fig. 4.3(a) and (b).

The first effect can be inferred from the overshoot in the nematic order parameter profile compared to the final equilibrium one; see Fig. 4.3(b). During the slow expansion, $S(z)$ gradually becomes negative indicating an orientational relaxation path characterized by the rods being preferentially oriented parallel to the wall [Fig. 4.4(b)].

This effect becomes even more pronounced for the instantaneous expansion, shown in Fig. 4.5(b). Here, the initially depleted area is flooded with rods that are strongly oriented parallel to the walls. This is best seen for the curves t_1 , t_2 and t_3 in Fig. 4.5(b) where $S < -0.4$ close to the walls.

Both expansion processes B and C roughly consist of two steps. First, the initial two peak structure of $S(z, t)$ rapidly vanishes within the time interval of about $1\tau_B$. Second, a slow evolution (spanning multiple τ_B) towards the final three peak structure is observed. On the contrary, for the slow compression case the initial two peak structure is preserved throughout the process and the weak third peak at $z = 0$ slowly fades.

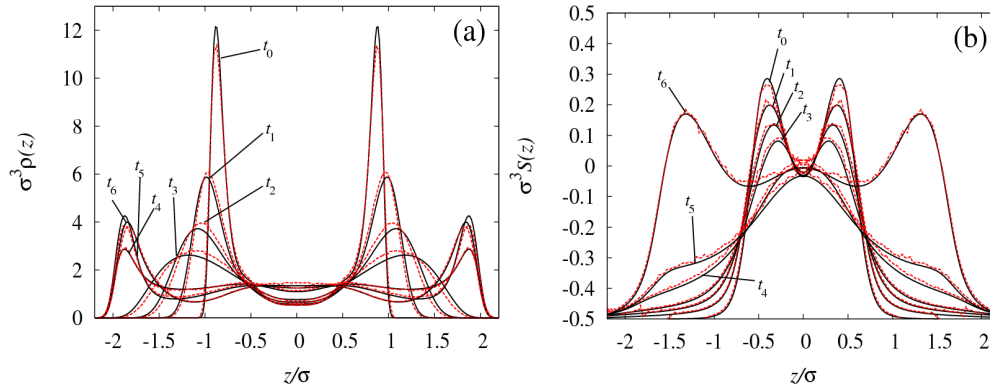


Figure 4.5: DDFT (solid black curves) and BD (dashed red curves) results for (a) the time-dependent density profile and (b) order parameter for the instantaneous expansion; see C in Table 4.1. The profiles correspond to the following time sequence: $t_0 = 0.0$, $t_1 = 0.02\tau_B$, $t_2 = 0.04\tau_B$, $t_3 = 0.06\tau_B$, $t_4 = 0.08\tau_B$, $t_5 = 0.25\tau_B$, and $t_6 = 15.0\tau_B$. The initial curves and those for t_6 coincide with the corresponding ones in Fig. 4.4.

Now we turn our attention to the time evolution of the density profiles $\rho(z, t)$. For the slow compression, the preferred homeotropic alignment corresponds to a *shoulder* in the density profiles [see t_4 and t_5 Fig. 4.3(a)]. Note that it is not present in the final equilibrated configuration: t_6 in Fig. 4.3(a). Due to the increased local homeotropic alignment, there is an excess of rods with position $Z - L/2 \geq |z| \geq Z$ which gives rise to the shoulder.

Apart from the shoulder, the density profiles for the slow expansion and compression processes seem very similar. Both show a layering effect that becomes manifest by a third peak emerging at $z = 0$. This is most pronounced for $t \approx 0.5\tau_B$ where the effective wall-wall distance is such that three layers of rods can be accommodated between the walls. For the sudden expansion, the correlation peaks vanish completely during the relaxation process

and the path toward the new equilibrium state goes via a four-peak structure illustrated by curve t_4 . Another difference is that the planar oriented rods give rise to an overshoot in the correlation peaks compared to the final equilibrated profile; see t_5 and t_6 .

In order to quantify the described asymmetry of the path of the different processes we calculate the second moment of the density, defined as

$$m_2(t) = \int dz z^2(\rho(z, t) - \rho(z, t = \infty)). \quad (4.26)$$

The quantity $m_2(t)$ is a measure of the spread of $\rho(z, t)$ around its center. The resulting curves are shown in Fig. 4.6. In a similar study for spherical

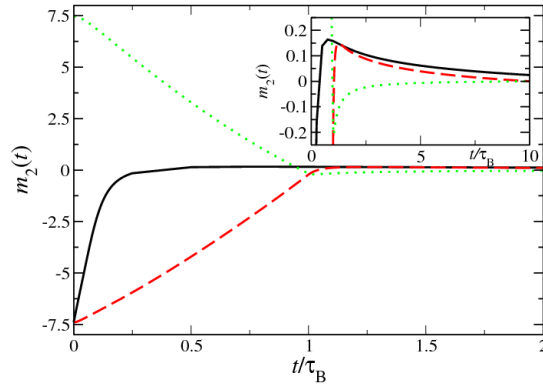


Figure 4.6: Second moment of the density profiles, $m_2(t)$, versus time t . The full black curve corresponds to the instantaneous relaxation C, the long-dashed red curve to the continuous relaxation B, and the short-dashed green curve to the compression A, respectively. The inset shows a magnified view of the same curves for small values of $m_2(t)$.

particles [36], it was found that $m_2(t)$ behaves *monotonically* and can be best fitted to a single-exponential function for the expansion case and to a double-exponential function for the compression process. Here, $m_2(t)$ turns out to be a *nonmonotonic* function of time for all three processes which precludes a simple description in terms of an exponentially decaying function. From this we may already conclude that there is an interesting interplay between rotational and translational dynamics not found in systems of spherical particles.

The complicated relaxational behavior found here is related to the non-monotonous evolution of the density profiles due to a transient enhanced localization of rods, *viz.* the shoulders emerging during the compression process. Finally, we note that in all three setups the reorientation process toward

the new equilibrium state is approximately an order of magnitude slower than the initial relaxation of the positional degrees of freedom of the rods.

4.5.2 Orienting external field

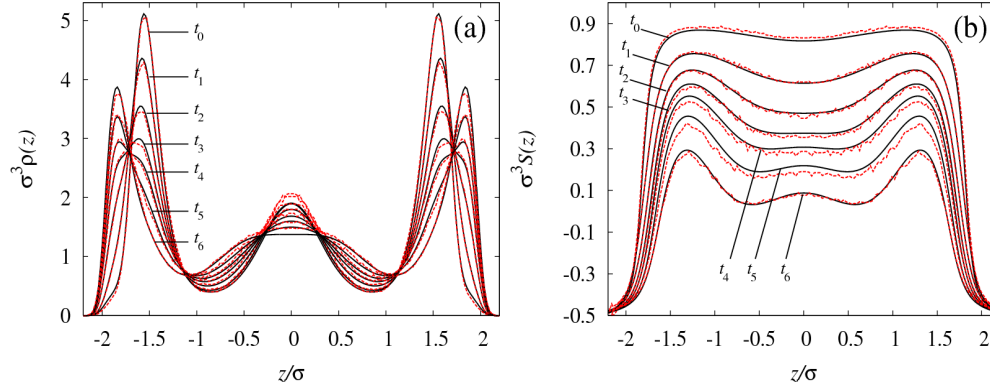


Figure 4.7: DDFT (solid black curves) and BD (dashed red curves) results for (a) the time-dependent density profile and (b) order parameter for the relaxation of an initially aligned state; see D in Table 4.1. The profiles correspond to the following time sequence: $t_0 = 0.0$, $t_1 = 1.0\tau_B$, $t_2 = 2.0\tau_B$, $t_3 = 3.0\tau_B$, $t_4 = 4.0\tau_B$, $t_5 = 6.0\tau_B$, and $t_6 = 15.0\tau_B$.

We will now focus on the setups D and E in Table 4.1, a slab confinement of fixed wall separation with an additional orienting field. We investigate both the relaxation from an initially aligned state by instantaneously switching off the field (Fig. 4.7) and the opposite case, in which a system is driven into an aligned state after the field is switched on (Fig. 4.8). For the relaxation process both density and order parameter profiles agree very well with the simulation results. For the aligning process, however, larger discrepancies are found, especially in the nematic order parameter profiles. Here, the orienting process seems to be faster in the DDFT than in the BD simulations. (See Fig. 4.8(b).) A possible explanation is that the fast aligning process generates additional dynamic correlations that are not accounted for by the adiabatic assumption in our DDFT.

Although the external orienting field couples only to the orientation of the rods, the positions are also clearly affected. By forcing the rods to orient perpendicular to the wall, rod overlaps will be more common and the system will feel an effective compression. As a result, layering becomes more prominent, as we see from the sharpening of the density peaks in Fig. 4.8(a). The order parameter profiles show that the rods strongly orient perpendicular to

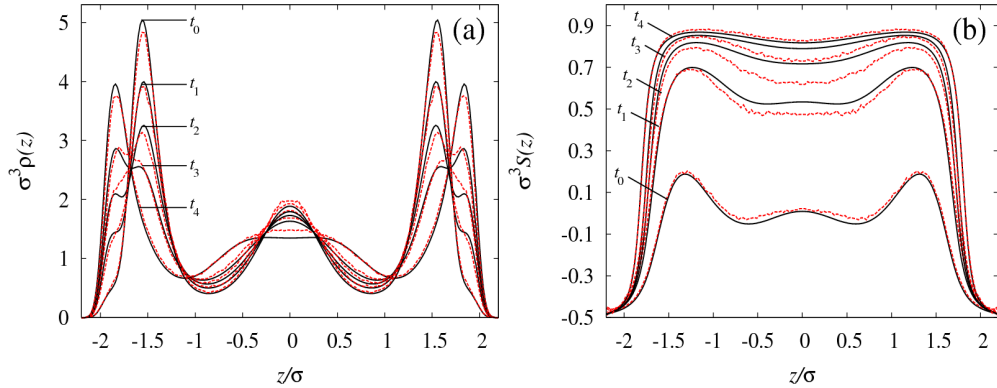


Figure 4.8: DDFT (solid black curves) and BD (dashed red curves) results for (a) the time-dependent density profile and (b) order parameter for the inverse case to Fig. 4.7, the evolution towards an aligned state; see E in Table 4.1. The profiles correspond to the following time sequence: $t_0 = 0.0$, $t_1 = 3.0\tau_B$, $t_2 = 5.0\tau_B$, $t_3 = 7.0\tau_B$, $t_4 = 20.0\tau_B$.

the wall when the orienting field is switched on resulting in a value close to unity. Only very close to the walls do the rods lie parallel but the local density there is rather low.

In order to demonstrate the asymmetry of the two processes, we show the absolute values of the second moment in Fig. 4.9. First of all, the two data for $m_2(t)$ fall on different curves showing that the processes are asymmetric. Still both systems need approximately the same time to equilibrate, roughly $20\tau_B$. Furthermore, the log-linear plot shown in the inset shows that there are clear deviations from a straight line. Hence again the behavior is not a single exponential function in time. In contrast to the compression and expansion the time evolution of $m_2(t)$ is a monotonous function of t for both situations.

4.6 Conclusions

We have presented a formalism to predict the dynamical evolution under nonequilibrium conditions for anisotropic colloidal particles. The input needed for this theory is the equilibrium free energy density functional. Within a mean-field approximation for the functional valid for bounded Gaussian segment-segment interactions, the relaxation dynamics was studied for rods confined in a slab geometry. Slab expansion and compression was studied as well as turning on and off an aligning external field. Good agreement with

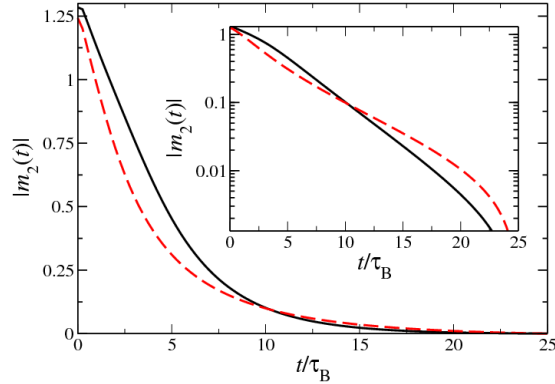


Figure 4.9: Absolute value of the second moment $m_2(t)$ of the density profiles defined in Eq. 4.26 against time t . The full black curve shows $|m_2(t)|$ for the situation when the orienting field is switched on E and the long-dashed red curve the inverse D. The inset shows a logarithmic plot of the same.

Brownian dynamics computer simulations was found. The relaxation was a nontrivial interplay between rotational and translational dynamics. The system chose different paths of relaxation upon compression and expansion implying that the sequence of density fields is not inversion symmetric, even not with a suitably scaled time variable.

The present formalism can be applied to describe both different systems and setups. For examples, hard rods or platelets can be treated by more sophisticated density functionals, as, e.g., within the fundamental measure-like approximation [114, 137, 138] and Yukawa-segment models can be described by a mapping onto effective hard spherocylinders [139]. Other setups concern switching dynamics in different aligning fields which is the basic process in a liquid-crystalline optical device [140–142], sedimentation problems in rod-like suspensions [143–146] and orientational dynamics in rotating light fields [82, 83, 147, 148]. Furthermore, it would be interesting to study the orientational glass transition within the DDFT approach in order to explore whether the orientational and translational dynamics get frozen-in at the same densities or not [125, 149]. For future studies it would be challenging to incorporate shear flow in the dynamical density functional theory formalism in which case macroscopic solvent flow will couple strongly to the orientation of rodlike particles [150, 151]. We acknowledge that serious modifications have to be carried out to our present DDFT formalism in order to correctly account for the distorted pair correlation function due to the shear [152–154]. In connection with the previous section, the ultimate goal would be to derive a DDFT for anisotropic particles including hydrodynamic interactions. Fi-

nally we think that the present approach will be helpful to describe solvation dynamics [155, 156], the orientational diffusion of supramolecular aggregates (like proteins) in solution and the dynamics of stiff polymers [157].

Chapter 5

Conclusion and outlook

In summary, we have investigated the out-of-equilibrium dynamics of colloidal systems in external fields using theory and computer simulations. In the first part of this thesis we examined an equimolar binary mixture of oppositely charged colloidal particles, which were driven by an external field, by means of extensive Brownian dynamics simulations. In this system Leunissen *et al.* [28] found the first experimental realization of lane formation. Lane formation is a nonequilibrium phase transition, in which oppositely driven colloids avoid each other by forming lanes which comprise only particles driven alike [20, 21, 43–47]. We confirmed the findings of Leunissen and co-workers, and focused on the influence of hydrodynamic interactions on the nonequilibrium state. For that purpose we studied two different situations, namely sedimentation and electrophoresis where the colloids were driven either by gravity or by an electric field. While the direct forces were chosen to be identical, the hydrodynamic interactions are different in the two situations. In the electrophoresis case the Oseen contribution to the mobility tensor is screened due to the forces acting on the counterion cloud surrounding a charged colloid. Additionally, we compared the results to those obtained by simulations where hydrodynamic interactions were neglected. We have analyzed the steady-states by structural diagnostics and identified different states in the lateral direction, i.e. perpendicular to the driving field. At high Coulomb coupling and low densities, a chaining of oppositely charged lanes was observed. Furthermore, there is the possibility of lateral crystallization of lanes into two-dimensional square, triangular, or rhombic lattices. The various steady-state can qualitatively be understood in terms of a competition of the mutual Coulomb attraction and friction of sliding lanes. All states were summarized in steady-state diagrams as a function of the volume fractions and the screening lengths. The screening of the solvent mediated interactions in the electrophoresis has led to a very similar steady-state phase

diagram compared to the phase diagram in the simple case of neglected hydrodynamic interactions. On the other hand, during sedimentation, friction of sliding lanes is strongly enhanced leading to macroscopic separation of lanes. We have further analyzed the nature of the lane transition for varying driving strengths and found an interesting feature. In the sedimentation the nonequilibrium phase transition seems to be of first order with a significant jump and hysteresis in an appropriate order parameter. Conversely, in the electrophoresis, and when the solvent mediated interactions are ignored, the transition was found to be second order. For future studies, more sophisticated simulation techniques needed to test the validity of the Long-Ajdari tensor for the electrophoresis and to account for many-body interactions, lubrication forces, and deformation of the counterion cloud due to the electric field. There are several promising approaches, e.g. the stochastic rotation dynamics code [87, 88], a lattice Boltzmann theory including hydrodynamics [89–93] and counterion flow or the recently developed fluid particle dynamics methods [94–96]. What is also missing is a detailed comparison with experimental data from Ref. [28]. Work along these lines is in progress. Recently, lane formation was also observed in a dusty plasma system. Here, the appropriate particle dynamics are given by the Fokker-Planck equation. It would be interesting to scrutinize the influence of the dynamics of the particles on the formation of lanes.

In chapter 3, we presented a dynamical density functional theory (DDFT) which takes hydrodynamic interactions on a two-body level into account. The only approximation in the derivation was that the n -body densities are approximated by those of an equilibrium system whose one-body densities are equal. The formalism presented here provides a theory that can be applied to arbitrary time dependent external potentials and systems, provided an accurate equilibrium free energy functional is known and the external forces are not too strong, such that the underlying assumption is still accurate. The theory reduces to the original version of DDFT derived by Marconi and Tarazona when hydrodynamic interactions are neglected. As a demonstration of the theory we have analyzed the dynamics of hard spheres in an unstable spherical optical trap supplied by Rosenfeld’s very reliable excess free energy functional and compared the results to those obtained by Brownian dynamics simulations. We found that the theory reproduces the simulation results as long as the external forces were moderate and demonstrated thereby the validity of our theory. Additionally, we calculated the density profiles from the original version of dynamical density functional theory for the same setup but without hydrodynamic interactions. We found that the coupling of the particles mediated through the solvent slowed the dynamics considerably. For future studies, it would be interesting to apply

the presented DDFT to the setup studied in chapter 2 and to have a theory that predicts lane formation. Finally, Archer [109] has demonstrated how mode-coupling theory, which is capable of predicting the glass transition but ignores hydrodynamic interaction, can be derived from a DDFT for atomic liquids with further approximations. It is tempting to use our formalism to obtain a mode-coupling theory including hydrodynamic interactions since it is anticipated that hydrodynamic interactions play an important role near the colloidal glass transition [118]. For future work, it would be further challenging to expand the present formalism to many-body hydrodynamic interactions.

A generalization of DDFT to anisotropic particles with orientational degrees of freedom but without hydrodynamic interactions was derived in the last chapter of this thesis. The formalism allows for studying arbitrary external potentials in nonequilibrium albeit with some discrepancies anticipated for strongly driven systems “far from equilibrium”, since the underlying approximation is expected to work best for relaxational dynamics. Once again, the accuracy of the theory crucially depends on the excess free energy. In this chapter, we use a mean-field approximation for the density functional, which is essentially exact for unbounded potentials at high densities. Therefore, we chose for the rod interaction a Gaussian-segment model which describes bottlebrush polymers with a stiff backbone. We then applied our theory to predict the time-evolution of the density profiles of a concentrated rod suspension in a confined slab geometry made by two parallel soft walls. Slab expansion and compression was studied, as well as the effect of an aligning external field which was either switched on or off. Good agreement with Brownian dynamics computer simulations was found. The relaxation was a nontrivial interplay between rotational and translational dynamics. The system chose different paths of relaxation upon compression and expansion implying that the sequence of density fields is not inversion symmetric, even with a suitably scaled time variable. The present formalism can be also applied to describe different particle shapes like platelets or hard spherocylinders. Furthermore, it would be interesting to study the orientational glass transition within the DDFT approach in order to explore whether the orientational and translational dynamics become frozen-in at the same densities or not [125, 149]. Finally, in connection with the previous chapter, a density functional theory for anisotropic particles and hydrodynamic interactions would be desirable.

Appendix A

Ewald sum of $\boldsymbol{\mu}_{ij}^{\text{LA}}$

In the appendix, the lattice sum of the long ranged dipole part of the Long-Ajdari tensor $\boldsymbol{\mu}_{ij}^{\text{LA}}$ is given. The scheme is adapted from the more general summation by Beenakker [69].

We consider a three-dimensional periodic lattice in which each unit cell (volume V , numbered by the index l) contains N spherical particles (radius a , numbered by the index i) with inverse screening length κ and friction coefficient $\gamma = 6\pi\eta a$, where η is the viscosity of the solvent. The lattice points are given by the vectors \mathbf{R}_l and the particles have position vectors $\mathbf{r}_{il} = \mathbf{r}_i + \mathbf{R}_l$. The force on particle i is denoted by \mathbf{F}_i . The total force on the particles in a unit cell is assumed to vanish:

$$\sum_{i=1}^N \mathbf{F}_i = 0 \quad (\text{A.1})$$

Now we consider the following lattice sum:

$$\mathbf{S}_{i_0} = \sum_l \left(\sum_{i=1}^N \boldsymbol{\mu}_{i_0 l_0, il} \cdot \mathbf{F}_i \right), \quad (\text{A.2})$$

with the long ranged part of $\boldsymbol{\mu}_{ij}^{\text{LA}}$:

$$\gamma \boldsymbol{\mu}_{i_0 l_0, il} = \begin{cases} \frac{3a}{2\kappa^2 |\mathbf{x}|^3} (\mathbf{1} - 3\hat{\mathbf{x}}\hat{\mathbf{x}}) & \text{for } (i, l) \neq (i_0, l_0) \\ \mathbf{1} & \text{for } (i, l) = (i_0, l_0) \end{cases} \cdot \quad (\text{A.3})$$

with $\mathbf{x} = \mathbf{r}_{il} - \mathbf{r}_{i_0 l_0}$ and $\hat{\mathbf{x}} = \mathbf{x}/|\mathbf{x}|$. Using the the Ewald summation technique, Beenakker has rewritten this series into a rapidly converging form (with the

simple modification $a^3 \rightarrow 3a\kappa^{-2}$):

$$\begin{aligned} \gamma \mathbf{S}_{i_0} &= (1 - 40\pi^{-1/2}\xi^3 a\kappa^{-2}) \mathbf{F}_{i_0} \\ &+ \sum_l \sum_{\substack{i=1 \\ \mathbf{r}_{il} \neq \mathbf{r}_{i_0 l_0}}}^N \boldsymbol{\mu}^{(1)}(\mathbf{r}_{il} - \mathbf{r}_{i_0 l_0}) \cdot \mathbf{F}_i \\ &+ V^{-1} \sum_{\substack{\lambda \\ \mathbf{k}_\lambda \neq 0}}^N \boldsymbol{\mu}^{(2)}(\mathbf{k}_\lambda) \cdot \mathbf{F}_i \cos[\mathbf{k}_\lambda \cdot (\mathbf{r}_i - \mathbf{r}_{i_0})], \end{aligned} \quad (\text{A.4})$$

with the definitions

$$\begin{aligned} \boldsymbol{\mu}^{(1)} &= \mathbf{1} \left\{ \frac{3}{2} a\kappa^{-2} r^{-3} \text{erfc}(\xi r) + \right. \\ &\quad \left. (4\xi^7 r^4 - 20\xi^5 r^2 + 14\xi^3 + \xi r^{-2}) 3a\kappa^{-2} \pi^{-1/2} \exp(-\xi^2 r^2) \right\} + \\ &\hat{\mathbf{r}} \hat{\mathbf{r}} \left\{ -\frac{9}{2} a\kappa^{-2} \text{erfc}(\xi r) + \right. \\ &\quad \left. (-4\xi^7 r^4 + 16\xi^5 r^2 - 2\xi^3 - 3\xi r^{-2}) 3a\kappa^{-2} \pi^{-1/2} \exp(-\xi^2 r^2) \right\} \end{aligned} \quad (\text{A.5})$$

$$\boldsymbol{\mu}^{(2)} = -6\pi a\kappa^{-2} \left(\mathbf{1} - \hat{\mathbf{k}} \hat{\mathbf{k}} \right) \left(1 + \frac{1}{4} \xi^{-2} k^2 + \frac{1}{8} \xi^{-4} k^4 \right) \exp \left(-\frac{1}{4} \xi^{-2} k^2 \right). \quad (\text{A.6})$$

The second lattice sum in Eq. A.4 runs in reciprocal space over reciprocal lattice vectors \mathbf{k}_λ satisfying $\exp(i\mathbf{k} \cdot \mathbf{r}_l) = 1$ for all l . $\xi > 0$ is an convergence rate control parameter.

Bibliography

- [1] C. N. Likos, Phys. Rep. **348**, 261 (2001).
- [2] R. J. Hunter, *Foundations of Colloid Science*, Oxford University Press, Oxford, 2 edition, 1989.
- [3] H. Löwen, J. Phys.: Condens. Matter **13**, R415 (2001).
- [4] R. B. Jones, Ann. Rev. Phys. Chem. **42**, 137 (1991).
- [5] R. G. Smith and G. C. Maitland, Chem. Eng. Res. Des. **76**, 539 (1998).
- [6] R. A. L. Jones, *Soft Condensed Matter*, Oxford University Press, Oxford, 2002.
- [7] D. Frenkel, Physica A **313**, 1 (2002).
- [8] L. Onsager, Ann. N.Y. Acad. Sci. **51**, 627 (1949).
- [9] J. P. Hansen and I. R. MacDonald, *Theory of Simple Liquids*, Academic, London, 3 edition, 2006.
- [10] J. K. G. Dhont, *An Introduction to Dynamics of Colloids*, Elsevier Science, Amsterdam, 1996.
- [11] W. B. Russel, D. A. Saville, and W. R. Schowalter, *Colloidal Dispersions*, Cambridge University Press, Cambridge, 1989.
- [12] A. van Blaaderen, M.R.S. Bulletin **29**, 85 (2004).
- [13] M. P. Allen and D. J. Tildesley, editors, *Computer Simulation of Liquids*, Clarendon Press Oxford, Oxford, 1989.
- [14] M. Baus, L. Rull, and J. Ryckaert, editors, *Observation, Prediction and Simulation of Phase Transitions in Complex Fluids*, volume Series B: Physics, Kluwer Academic Publisher, Dordrecht, 1995.

-
- [15] H. Löwen, Phys. Rep. **237**, 249 (1994).
- [16] J. Dzubiella and H. Löwen, J. Phys.: Condens. Matter **14**, 9383 (2002).
- [17] B. Schmittmann and R. K. P. Zia, *Statistical mechanics of driven diffusive systems*, Academic Press, London, 1995.
- [18] S. Katz, J. L. Lebowitz, and H. Spohn, Phys. Rev. B **28**, 1655 (1983).
- [19] S. Katz, J. L. Lebowitz, and H. Spohn, J. Stat. Phys. **34**, 497 (1984).
- [20] J. Dzubiella, G. P. Hoffmann, and H. Löwen, Phys. Rev. E **65**, 021402 (2002).
- [21] H. Löwen and J. Dzubiella, Faraday Discuss. **123**, 99 (2003).
- [22] G. C. M. A. Ehrhardt, A. Stephenson, and P. M. Reis, Phys. Rev. E **71**, 041301 (2005).
- [23] M. P. Ciamarra, A. Coniglio, and M. Nicodemi, Phys. Rev. Lett. **94**, 188001 (2005).
- [24] A. Wysocki and H. Löwen, J. Phys.: Condens. Matter **16**, 7209 (2004).
- [25] M. Das, S. Ramaswamy, and G. Ananthakrishna, Europhys. Lett. **60**, 636 (2002).
- [26] R. Kolbl and D. Helbing, N. J. Phys. **5**, 48 (2003).
- [27] R. Jiang, D. Helbing, P. K. Shuklai, and Q. S. Wu, Physica A **368**, 567 (2006).
- [28] M. E. Leunissen et al., Nature **437**, 235 (2005).
- [29] R. Evans, Adv. in Phys. **28**, 143 (1979).
- [30] J. Z. Wu, AIChE Journal **52**, 1169 (2006).
- [31] U. M. B. Marconi and P. Tarazona, J. Phys.: Condens. Matter **12**, A413 (2000).
- [32] W. Dieterich, H. L. Frisch, and A. Majhofer, Z. Phys. B: Condens. Matter **78**, 317 (1990).
- [33] U. M. B. Marconi and P. Tarazona, J. Chem. Phys. **110**, 8032 (1999).
- [34] A. J. Archer and R. Evans, J. Chem. Phys. **121**, 4246 (2004).

-
- [35] G. K. L. Chan and R. Finken, *Phys. Rev. Lett.* **94**, 183001 (2005).
- [36] J. Dzubiella and C. N. Likos, *J. Phys.: Condens. Matter* **15**, L147 (2003).
- [37] C. P. Royall, J. Dzubiella, M. Schmidt, and A. V. Blaaderen, *Phys. Rev. Lett.* **98**, 188304 (2007).
- [38] A. J. Archer, *J. Phys.: Condens. Matter* **17**, 1405 (2005).
- [39] M. Rex, H. Löwen, and C. N. Likos, *Phys. Rev. E* **72**, 021404 (2005).
- [40] M. Rex, C. N. Likos, H. Löwen, and J. Dzubiella, *Mol. Phys.* **104**, 527 (2006).
- [41] T. A. Witten, *Rev. Mod. Phys.* **71**, S367 (1999).
- [42] M. Medebach and T. Palberg, *J. Chem. Phys.* **119**, 3360 (2003).
- [43] R. R. Netz, *Europhys. Lett.* **65**, 616 (2003), A corresponding state in two spatial dimensions was already proposed as an alternating stripe pattern.
- [44] J. Chakrabarti, J. Dzubiella, and H. Löwen, *Europhys. Lett.* **61**, 415 (2003).
- [45] J. Delhommelle, *Phys. Rev. E* **71**, 016705 (2005).
- [46] R. B. Pandey, J. F. Gettrust, R. Seyfarth, and L. A. Cueva-Parra, *Int. J. Mod. Phys. C* **14**, 955 (2003).
- [47] M. Köppl, P. Henseler, A. Erbe, P. Nielaba, and P. Leiderer, *Phys. Rev. Lett.* **97**, 208302 (2006).
- [48] T. Mullin, *Phys. Rev. Lett.* **84**, 4741 (2000).
- [49] G. P. Saracco and E. V. Albano, *J. Chem. Phys.* **118**, 4157 (2003).
- [50] A. P. Hynninen, M. E. Leunissen, A. van Blaaderen, and M. Dijkstra, *Phys. Rev. Lett.* **96**, 018303 (2006).
- [51] A. P. Hynninen, C. G. Christova, R. van Roij, A. van Blaaderen, and M. Dijkstra, *Phys. Rev. Lett.* **96**, 138308 (2006).
- [52] C. P. Royall, M. E. Leunissen, A. P. Hynninen, M. Dijkstra, and A. van Blaaderen, *J. Chem. Phys.* **124**, 2447061 (2006).

-
- [53] D. L. Ermak and J. A. McCammon, *J. Chem. Phys.* **69**, 1352 (1978).
- [54] D. M. Heyes and A. C. Brańka, *Mol. Phys.* **98**, 1949 (2000).
- [55] A. C. Brańka and D. M. Heyes, *Phys. Rev. E* **60**, 2381 (1999).
- [56] D. L. Ermak, *J. Chem. Phys.* **62**, 4189 (1975).
- [57] E. Wajnryb, P. Szymczak, and B. Cichocki, *Physica A* **335**, 339 (2004).
- [58] J. Rotne and S. Prager, *J. Chem. Phys.* **50**, 4831 (1969).
- [59] D. Long and A. Ajdari, *Eur. Phys. J. E* **4**, 29 (2001).
- [60] S. Kim and S. J. Karrila, *Microhydrodynamics: Principles and selected applications*, Butterworth-Heinemann, Boston, 1991.
- [61] L. Durlofsky, J. F. Brady, and G. Bossis, *J. Fluid Mech.* **180**, 21 (1987).
- [62] A. J. C. Ladd, *J. Chem. Phys.* **88**, 5051 (1988).
- [63] B. Cichocki, B. U. Felderhof, K. Hinsen, E. Wajnryb, and J. Błiawdziewicz, *J. Chem. Phys.* **100**, 3780 (1994).
- [64] A. Sierou and J. F. Brady, *J. Fluid Mech.* **448**, 115 (2001).
- [65] A. J. Banchio and J. F. Brady, *J. Chem. Phys.* **118**, 10323 (2003).
- [66] E. R. Smith, I. K. Snook, and W. van Meegen, *Physica A* **143A**, 441 (1987).
- [67] E. R. Smith, *Faraday Discuss. Chem. Soc.* **83**, 193 (1987).
- [68] J. F. Brady, R. J. Phillips, J. C. Lester, and G. Bossis, *J. Fluid Mech.* **195**, 257 (1988).
- [69] C. W. J. Beenakker, *J. Chem. Phys.* **85**, 1581 (1986).
- [70] M. Teubner and R. Strey, *J. Chem. Phys.* **87**, 3195 (1987).
- [71] G. Gompper and M. Schick, *Phys. Rev. Lett.* **62**, 1647 (1989).
- [72] A. Jaster, *Europhys. Lett.* **42**, 277 (1998).
- [73] H. Weber, D. Marx, and K. Binder, *Phys. Rev. B* **51**, 14636 (1995).
- [74] M. Heni and H. Löwen, *J. Phys.: Condens. Matter* **13**, 4675 (2001).

- [75] B. I. Halperin and D. R. Nelson, *Phys. Rev. Lett.* **41**, 121 (1978).
- [76] T. Tlusty and S. A. Safran, *Science* **290**, 1328 (2000).
- [77] J. J. Weis, *J. Phys.: Condens. Matter* **15**, S1471 (2003).
- [78] J. J. Weis, J. M. Tavares, and M. M. T. da Gama, *J. Phys.: Condens. Matter* **14**, 9171 (2002).
- [79] M. Rex and H. Löwen, *Phys. Rev. E* **75**, 051402 (2007).
- [80] M. Watzlawek and G. Nägele, *Jour. Colloid Interface Sci.* **214**, 170 (1999).
- [81] M. Rex, T. Vissers, C. P. Royall, A. van Blaaderen, and H. Löwen, Second order nonequilibrium phase transition in oppositely charged driven colloids, (unpublished).
- [82] R. Kirchhoff and H. Löwen, *Europhys. Lett.* **69**, 291 (2005).
- [83] R. Kirchhoff and H. Löwen, *J. Phys.: Condens. Matter* **17**, 7805 (2005).
- [84] H. H. Wensink and H. Löwen, *Phys. Rev. Lett.* **97**, 038303 (2006).
- [85] C. Reichhardt and C. J. O. Reichhardt, *Phys. Rev. E* **74**, 011403 (2006).
- [86] J. Chakrabarti, J. Dzubiella, and H. Löwen, *Phys. Rev. E* **70**, 012401 (2004).
- [87] J. T. Padding and A. A. Louis, *Phys. Rev. E* **74**, 031402 (2006).
- [88] J. T. Padding and A. A. Louis, *Phys. Rev. Lett.* **93**, 220601 (2004).
- [89] V. Lobaskin and B. Dünweg, *N. J. Phys.* **6**, 54 (2004).
- [90] A. Chatterji and J. Horbach, *J. Chem. Phys.* **122**, 184903 (2005).
- [91] F. Capuani, I. Pagonabarraga, and D. Frenkel, *J. Chem. Phys.* **124**, 124903 (2006).
- [92] A. Chatterji and J. Horbach, *J. Chem. Phys.* **126**, 064907 (2007).
- [93] V. Lobaskin, B. Dünweg, M. Medebach, T. Palberg, and C. Holm, *Phys. Rev. Lett.* **98**, 176105 (2007).

-
- [94] H. Kodama, K. Takeshita, T. Araki, and H. Tanaka, *J. Phys.: Condens. Matter* **16**, L115 (2004).
- [95] K. Kim, Y. Nakayama, and R. Yamamoto, *Phys. Rev. Lett.* **96**, 208302 (2006).
- [96] K. Kim and R. Yamamoto, *Macromol. Theory Simul.* **14**, 278 (2005).
- [97] G. Nägele and J. K. G. Dhont, *J. Chem. Phys.* **108**, 9566 (1998).
- [98] G. Nägele and J. Bergenholtz, *J. Chem. Phys.* **108**, 9893 (1998).
- [99] G. Nägele, J. Bergenholtz, and J. K. G. Dhont, *J. Chem. Phys.* **110**, 7037 (1999).
- [100] G. Nägele, *J. Phys.: Condens. Matter* **15**, S407 (2003).
- [101] B. Cichocki, M. L. Ekiel-Jezewska, P. Szymczak, and E. Wajnryb, *J. Chem. Phys.* **117**, 1231 (2002).
- [102] R. Pesché and G. Nägele, *Europhys. Lett.* **51**, 584 (2000).
- [103] Y. Singh, *Phys. Rep.* **207**, 351 (1991).
- [104] Y. Rosenfeld, *Phys. Rev. Lett.* **63**, 980 (1989).
- [105] Y. Rosenfeld, M. Schmidt, H. Löwen, and P. Tarazona, *Phys. Rev. E* **55**, 4245 (1997).
- [106] N. Grewe and W. Klein, *J. Math. Phys.* **18**, 1729 (1977), *ibid.* **64** 1735 (1977).
- [107] C. N. Likos, A. Lang, M. Watzlawek, and H. Löwen, *Phys. Rev. E* **63**, 031206 (2001).
- [108] F. Penna, J. Dzubiella, and P. Tarazona, *Phys. Rev. E* **68**, 061407 (2003).
- [109] A. J. Archer, *J. Phys.: Condens. Matter* **18**, 5617 (2006).
- [110] A. J. Archer and M. Rauscher, *J. Phys. A: Math. Gen.* **37**, 9325 (2004).
- [111] G. Nägele, *The physics of colloidal soft matter*, Lecture notes, Institut of Fundamental Technological Research, Polish Academy of Science, Warsaw, Poland, 2004.

-
- [112] A. González, J. A. White, F. L. Román, S. Velasco, and R. Evans, *Phys. Rev. Lett.* **79**, 2466 (1997).
- [113] A. González, J. A. White, F. L. Román, and R. Evans, *J. Chem. Phys.* **109**, 3637 (1998).
- [114] A. Esztermann, H. Reich, and M. Schmidt, *Phys. Rev. E* **73**, 011409 (2005).
- [115] A. Trokhymchuk, I. Nezbeda, J. Jirsák, and D. Henderson, *J. Chem. Phys.* **123**, 024501 (2005).
- [116] B. Cichocki and K. Hinsen, *Physica A* **166**, 473 (1990).
- [117] D. R. Foss and J. F. Brady, *J. Rheol.* **44**, 629 (2000).
- [118] M. Tokuyama, *Rep. Inst. Fluid Science* **19**, 7 (2007).
- [119] J. K. G. Dhont and W. J. Briels, *J. Chem. Phys.* **118**, 1466 (2003).
- [120] J. K. G. Dhont and W. J. Briels, *Phys. Rev. E* **72**, 031404 (2005).
- [121] A. Lang, C. N. Likos, M. Watzlawek, and H. Löwen, *J. Phys.: Condens. Matter* **12**, 5087 (2000).
- [122] C. N. Likos et al., *Macromolecules* **34**, 2914 (2001).
- [123] S. Lecommandoux et al., *Macromolecules* **35**, 8878 (2002).
- [124] S. Jha, S. Dutta, and N. B. Bowden, *Macromolecules* **37**, 4365 (2004).
- [125] T. Theenhaus, R. Schilling, A. Latz, and M. Letz, *Phys. Rev. E* **64**, 051505 (2001).
- [126] C. G. Gray and K. E. Gubbins, *Theory of Molecular Fluids*, Clarendon Press, Oxford, 1984.
- [127] K. E. Gubbins, *Chem. Phys. Lett.* **76**, 329 (1980).
- [128] A. J. Archer, *J. Phys.: Condens. Matter* **17**, S3253 (2005).
- [129] F. Penna and P. Tarazona, *J. Chem. Phys.* **68**, 1766 (2003).
- [130] A. Poniewierski and R. Holyst, *Phys. Rev. A* **38**, 3721 (1988).
- [131] A. Chandra and B. Bagchi, *Physica A* **169**, 246 (1990).

-
- [132] A. Chandra and B. Bagchi, *J. Chem. Phys.* **91**, 1829 (1989).
- [133] H. H. Wensink, H. Löwen, M. Rex, C. N. Likos, and S. van Teeffelen, arXiv:0710.3111 (2007).
- [134] A. Chrzanowaksa, P. I. C. Teixeira, H. Ehrentraut, and D. J. Cleaver, *J. Phys.: Condens. Matter* **13**, 4715 (2001).
- [135] M. M. Tirado, C. L. Martinez, and J. G. de la Torre, *J. Chem. Phys.* **81**, 2047 (1984).
- [136] T. Kirchhoff, H. Löwen, and R. Klein, *Phys. Rev. E* **53**, 5011 (1996).
- [137] D. de las Heras, E. Velasco, and L. Mederos, *Phys. Rev. Lett.* **94**, 017801 (2005).
- [138] E. Velasco, L. Mederos, and D. E. Sullivan, *Phys. Rev. E* **62**, 3708 (2000).
- [139] H. Graf and H. Löwen, *Phys. Rev. E* **57**, 5744 (1998).
- [140] F. Barmes and D. J. Cleaver, *Chem. Phys. Lett.* **425**, 44 (2006).
- [141] D. Marenduzzo, E. Orlandini, and J. M. Yeomans, *Europhys. Lett.* **71**, 604 (2005).
- [142] T. D. Wilkinson, W. A. Crossland, and A. B. Davey, *Mol. Cryst. Liq. Cryst.* **401**, 171 (2003).
- [143] A. P. Philipse, *Curr. Op. Colloid Interface Sci.* **2**, 200 (1997).
- [144] S. V. Savenko and M. Dijkstra, *Phys. Rev. E* **70**, 051401 (2004).
- [145] F. M. van der Kooij, A. P. Philipse, and J. K. G. Dhont, *Langmuir* **16**, 5317 (2000).
- [146] Z. Dogic, A. P. Philipse, S. Fraden, and J. K. G. Dhont, *J. Chem. Phys.* **113**, 8368 (2000).
- [147] A. I. Bishop, T. A. Nieminen, N. R. Heckenberg, and H. Rubinsztein-Dunlop, *Phys. Rev. A* **68**, 033802 (2003).
- [148] Z. Cheng, P. M. Chaikin, and T. G. Mason, *Phys. Rev. Lett.* **89**, 108303 (2002).
- [149] M. Letz, R. Schilling, and A. Latz, *Phys. Rev. E* **62**, 5173 (2000).

-
- [150] Y. G. Tao, W. K. den Otter, and W. J. Briels, *Phys. Rev. Lett.* **95**, 237802 (2005).
- [151] Y. G. Tao, W. K. den Otter, J. K. G. Dhont, and W. J. Briels, *J. Chem. Phys.* **124**, 134906 (2006).
- [152] J. K. G. Dhont, *Phys. Rev. Lett.* **76**, 4269 (1996).
- [153] U. M. B. Marconi and P. Tarazona, *J. Chem. Phys.* **124**, 164901 (2006).
- [154] U. M. B. Marconi and S. Melchionna, *J. Chem. Phys.* **126**, 184109 (2007).
- [155] B. Bagchi and A. Chandra, *J. Chem. Phys.* **97**, 5126 (1992).
- [156] R. Ramirez and D. Borgis, *J. Phys. Chem. B* **109**, 6754 (2005).
- [157] M. Doi and S. F. Edwards, *The Theory of Polymer Dynamics*, Clarendon Press, Oxford, 1 edition, 1986.

Acknowledgments

First, I would like to express my gratitude to Hartmut Löwen for the great opportunity to work with him. It was an honor and pleasure to have him as my teacher and supervisor.

I would like to thank Prof. Dr. Gerhard Nägele for kindly accepting to referee this thesis and for the helpful suggestions, comments, and discussions.

I very much appreciate the work with Rik Wensink. It was very much fun writing those papers with you.

I especially like to thank Sven van Teeffelen, Matthew Jenkins, and Ansgar Esztermann for carefully proof-reading this manuscript. Sven, thanks for the numerous helpful suggestions and discussions. Ansgar, a very special thank for answering every single question with enormous patience, which you could not even escape moving to Göttingen.

I owe very special thanks to Dr. Martin Konieczny, Dr. Christian Mayer, and Dr. Norman Hoffmann for fruitful discussions and the best fun throughout the whole study.

Many thanks to former and current members of the ThPhyII group for the great working atmosphere and nice coffee-breaks. How can one study without?

I gratefully acknowledge financial support from the Graduiertenförderung der Heinrich-Heine-Universität.

I want to thank all my friends for keeping me in touch with the real world and all the support and precious reliefs.

My sincere thanks to my family supporting me in every situation all my life.

Finally, I thank you Celia, for your inestimable support and for every single day with you.

Die hier vorgelegte Dissertation habe ich eigenständig und ohne unerlaubte Hilfe angefertigt. Die Dissertation wurde in der vorgelegten oder in ähnlicher Form noch bei keiner anderen Institution eingereicht. Ich habe bisher keine erfolglosen Promotionsversuche unternommen.

Düsseldorf, den 17.12.2007

(Martin Rex)

